# Investigating the SEI formation in Li-ion batteries using novel in situ XPS-based approaches

Federico Giovanni Capone

Sorbonne Université

*Ecole Doctorale – ED 397 Physique et Chimie des Matériaux*

# Investigating the SEI formation in Li-ion batteries using novel *in situ* XPS-based approaches

Federico Giovanni Capone

Doctoral thesis in Physics and Chemistry of Materials

April $5^{th}$, 2024

Président de Jury : Lorenzo Steviano

| | | |
|---|---|---|
| Fabrice Bournel | Maître de conférence | Examinator |
| Magali Gauthier | Chercheur | Examinator |
| Patrick Le Fevre | Chercheur | Examinator |
| Giancarlo Panaccione | Professeur | Reporter |
| Lorenzo Steviano | Professeur | Reporter |
| Alexis Grimaud | Professeur | Supervisor |
| Antonella Iadecola | Ingénieur de Recherche | Supervisor |
| Jean-Pascal Rueff | Directeur de Recherche | Supervisor |

> “A process cannot be understood by stopping it. Understanding must move with the flow of the process, must join it and flow with it.”
>
> — Frank Herbert, Dune

# Contents

**Table of contents** iii

**Resumé** 1

**Abstract** 3

**List of Figures** 11

**1 Introduction** 15

1.1 Li-ion batteries . . . 16

1.1.1 Significant parameters in LIBs . . . 20

1.2 The solid-electrolyte interphase . . . 21

1.2.1 The SEI formation and composition . . . 23

1.2.2 The SEI structure and its dependence on the anode structure . . . 26

1.2.3 Characterization of the SEI . . . 28

1.3 The BIG-MAP project . . . 31

1.3.1 BIG-MAP materials . . . 32

1.3.2 Other materials used in this project . . . 33

1.4 Aim of this work . . . 35

**2 Experimental method** 39

2.1 Theory of X-ray Photoelectron Spectroscopy . . . 39

2.1.1 Core-level analysis . . . 46

2.1.2 Calculation of the binding energy . . . 48

2.2 Instrumentation . . . 50

2.2.1 Synchrotron radiation . . . 50

2.2.2 Vacuum environment . . . 52

2.2.3 Analyser . . . 53

2.3 HAXPES end-station at GALAXIES . . . 55
2.4 NAP-PES end-station at HIPPIE . . . 56
2.4.1 Dip & Pull method . . . 57
2.5 General procedure for XPS data analysis . . . 58
2.5.1 Choices for this manuscript . . . 59
2.5.2 Data calibration and BE levels in electrochemical cell . . . 60
2.5.3 Electrochemical potential of electrons . . . 61
2.5.4 Work function . . . 62
2.5.5 Calibrating energies for XPS solid samples . . . 64

**3 Study of the SEI formation using operando NAP-PES 67**

3.1 Description of the Dip & Pull experiment . . . 67
3.1.1 Choice of materials and validation . . . 68
3.1.2 Experimental procedure . . . 70
3.2 Energy calibration of NAP-PES spectra . . . 72
3.2.1 Calibration and interpretation of the binding energies . . . 72
3.2.2 Peaks intensity ratio . . . 76
3.3 The SEI formation using PC-based electrolyte . . . 77
3.3.1 Results on the thick liquid meniscus . . . 77
3.3.2 Results on the PC || GC interphase . . . 81
3.4 The influence of EC solvent . . . 85
3.4.1 Results on the thick liquid meniscus . . . 86
3.4.2 Results on the PC:EC || GC interphase . . . 88
3.5 The influence of VC additive . . . 91
3.5.1 Results on the thick liquid meniscus . . . 91
3.5.2 Results on the PC+VC || GC interphase . . . 93
3.6 Conclusion . . . 96

**4 Development of a HAXPES electrochemical cell** **97**

4.1 Cell design . . . . . 97

4.1.1 SESSA simulations . . . . . 101

4.2 Chips and membranes . . . . . 102

4.2.1 Sputtered carbon on 30 µm-thick $Si_3N_4$ commercial chip . . . . . 103

4.2.2 Bilayer graphene on hole pattern $Si_3N_4$ chip . . . . . 105

4.2.3 Sputtered carbon on home-made $Si_3N_4$ chip . . . . . 108

4.3 Conclusion . . . . . 114

**5 Conclusions and Perspectives** **115**

**Bibliography** **129**

**Acknowledgements** **131**

# Resumé

La formation de la couche interphasique entre l'électrode et l'électrolyte (SEI) est cruciale pour le fonctionnement des batteries Li-ions: la présence de la SEI élargit la fenêtre thermodynamique des électrodes et facilite l'accès à des tensions élevées, améliorant ainsi les performances des batteries. La stabilité de la SEI empêche la décomposition des espèces d'électrolyte, conférant ainsi à la batterie une durée de vie prolongée, une stabilité améliorée et une sécurité renforcée. Malgré son rôle central, les processus régissant la formation de la SEI demeurent un sujet d'étude actuel.
Parmi toutes les techniques appliquées pour étudier la formation de la SEI, la spectroscopie de photoélectrons des rayons X (XPS) est la technique la plus appropriée grâce à sa sensibilité chimique et de surface, permettant l'identification des différentes espèces formant la SEI. D'autre part, les contraintes expérimentales liées à la détection des photoélectrons et à l'environnement en ultra-vide peuvent limiter l'utilisation d'électrolytes liquides et empêcher l'étude des interfaces enterrées. Des approches innovantes avec l'XPS peuvent être développées grâce à l'utilisation des techniques de synchrotron aux rayons X.

Dans ce travail de thèse, la formation de la SEI est étudiée en utilisant deux approches spectroscopiques novatrices:

1. La spectroscopie de photoélectrons des rayons X à pression quasi-ambiante (NAP-PES) avec un dispositif Dip & Pull pour étudier l'influence de la formulation de l'électrolyte;

2. Une cellule *in situ* électrochimique pour l'étude par XPS de haute énergie cinétique (HAXPES) *operando* de la SEI dans des conditions électrochimiques réalistes.

Dans les deux cas, les résultats obtenus sont prometteurs, bien que des améliorations supplémentaires soient encore nécessaires, en particulier pour la cellule électrochimique *in situ* dédiée aux études de la SEI par HAXPES *operando*.

# Abstract

The formation of the solid electrolyte interphase (SEI) between the electrode and the electrolyte is critical for Li-ion battery functioning: the presence of the SEI expands the thermodynamic window of the electrodes and facilitate access to elevated voltages, improving the battery performances. Stability of the SEI prevents the decomposition of electrolyte species, thereby endowing the battery with prolonged life, improved stability, and enhanced safety. Despite its pivotal role, the enigmatic processes governing the SEI's formation remain the subject of ongoing investigation.

Among all the techniques applied to study the SEI formation, X-ray photoelectron spectroscopy (XPS) is the suitable technique thanks its chemical and surface sensitivity, enabling the identification of the different species forming the SEI. On the other hand, the experimental constraints related to the photoelectron detection and the ultra-high vacuum environment, can limit the use of liquid electrolyte and prevent the study of buried interfaces. Innovative XPS approaches can be developed, thanks to the use of X-ray synchrotron techniques.

In this work, the SEI formation is investigated using two novel spectroscopic approaches:

1. the near-ambient pressure XPS (NAP-PES) with a Dip & Pull setup, was used to study the influence of the electrolyte formulation;

2. the development of a tailored *in situ* cell for XPS at high kinetic energy (HAXPES) to study the SEI in a more realistic, electrochemical cell.

In both cases, the obtained results were promising, while further improvements are still needed, especially for the *in situ* electrochemical cell dedicated to HAXPES *operando* studies of the SEI.

# List of Figures


1.1 Total of publications per year as a result of the query "Li-ion batteries" on the "Dimensions.ai research database". . . . . 17

1.2 Schematic functioning of a Li-ion battery. . . . . 18

1.3 The HOMO and LUMO energy levels of the electrolyte defining the battery stability window and the electrode working potentials. . . . . 22

1.4 Molecule structures for some popular solvents used in Li-ion batteries. . . 24

1.5 SEI structure and composition. . . . . 26

1.6 Schematic of the a)*in situ* cell for *operando* HAXPES and the b)Dip & Pull NAP-PES setup . . . . . 35

2.1 Scheme of an XPS experiment. . . . . 40

2.2 Different energy levels involved in the XPS process. . . . . 41

2.3 Illustration of the three-step and one step models for XPS. . . . . 44

2.4 Universal curve for IMFP . . . . . 46

2.5 Survey spectra on $Si_3N_4$ chip collected at GALAXIES with $h\nu$ = 7 keV . . . 48

2.6 Schematic picture of a synchrotron with (1) linac, (2) booster, (3) storage ring, (4) and (5) are bending magnets and focusing undulators and (6) beamlines. . . . . 51

2.7 Scheme of a hemispherical photoelectrons analyser. . . . . 54

2.8 HAXPES end-station at GALAXIES beamline, SOLEIL. . . . . 55

2.9 Scheme of the differential pumping of a HiPP-3 analyser. . . . . 56

2.10 Scheme of a Dip & Pull NAP-PES experiment. . . . . 58

2.11 Pictures of the Dip & Pull NAP-PES setup at HIPPIE beamline. . . . . 59

2.12 Energy Levels diagram. . . . . 62

2.13 Energy levels diagram for XPS . . . . . 64

3.1 a) C 1s XPS spectra collected at different vertical positions on the GC electrode. b) C 1s XPS spectra of different phases measured in our system. . . . 69

3.2 C 1s XPS spectrum of PC solvent in measured at T=-140 °C with an Al $K_\alpha$ source. ($h\nu = 1489$ eV) . . . . . 70

3.3 Experimental procedure applied for the Dip & Pull NAP-PES experiment. . 71

3.4 a) At OCV, the electrolyte and the electrode have the same electrochemical potential. b) and c) effects on the applied voltage on the liquid electrolyte as a function of the distance from the electrode. . . . . 73

3.5 a) Chemical species dissolved in the electrolyte at OCV. b) Some of the degradation species dissolved in the electrolyte, thus having the same voltage applied. c) The SEI species start to deposit on the electrode, and "feel" a different applied voltage. . . . . 75

3.6 C 1s XPS spectra of PC as solvent of the liquid electrolyte measured at HIPPIE beamline (a), and as a frozen drop of PC at IPREM (b). . . . . 78

3.7 Electrochemical profile of the applied potential and resulting current during the *in situ* experiment. a) The applied voltage (blue) and the resulting current (red) as a function of time. b) The profile I vs V shows the resulting "stepped" CV. . . . . 79

3.8 a) C 1s XPS spectra measured during discharge on the PC bulk liquid meniscus. b) Evolution of the C 1s binding energies of the main components as a function of applied voltage. . . . . 79

3.9 a) O 1s XPS spectra measured during discharge on the PC bulk liquid meniscus. b) Evolution of the O 1s binding energies of the main components as a function of applied voltage. . . . . 80

3.10 a) F 1s XPS spectra measured during discharge on the PC bulk liquid meniscus. b) Evolution of the F 1s binding energies of the main components as a function of applied voltage. . . . . 81

3.11 a) C 1s XPS spectra measured during discharge on the PC||GC interphase. b) Evolution of the C 1s binding energies of the main components as a function of applied voltage. . . . . 82

3.12 a) O 1s XPS spectra measured over discharge on the PC||GC interphase. b) Evolution of the O 1s binding energies of the main components as a function of applied voltage. . . . . 84

3.13 a) F 1s XPS spectra measured over discharge on the PC||GC interphase. b) Evolution of the F 1s binding energies of the main components as a function of applied voltage. . . . . 85

3.14 Structure of EC and PC molecules. . . . . 86

3.15 a) C 1s XPS spectra measured during discharge on the PC:EC bulk liquid meniscus. b) Evolution of the C 1s binding energies of the main components as a function of applied voltage. . . . . 86

3.16 a) O 1s XPS spectra measured during discharge on the PC:EC bulk liquid meniscus. b) Evolution of the O 1s binding energies of the main components as a function of applied voltage. . . . . 87

3.17 a) F 1s XPS spectra measured during discharge on the PC:EC bulk liquid meniscus. b) Evolution of the F 1s binding energies of the main components as a function of applied voltage. . . . . 87

3.18 a) C 1s XPS spectra measured during discharge at the PC:EC||GC interphase. b) Evolution of the C 1s binding energies of the main components as a function of applied voltage. . . . . 88

3.19 a) O 1s XPS spectra measured during discharge at the PC:EC||GC interphase. b) Evolution of the O 1s binding energies of the main components as a function of applied voltage. . . . . 89

3.20 a) F 1s XPS spectra measured during discharge at the PC:EC||GC interphase. b) Evolution of the F 1s binding energies of the main components as a function of applied voltage. . . . . 89

3.21 a) C 1s XPS spectra measured during discharge at the PC+VC thick liquid meniscus. b) Evolution of the C 1s binding energies of the main components as a function of applied voltage. . . . . 91

3.22 a) O 1s XPS spectra measured during discharge at the PC+VC thick liquid meniscus. b) Evolution of the O 1s binding energies of the main components as a function of applied voltage. . . . . 92

3.23 a) F 1s XPS spectra measured during discharge at the PC+VC thick liquid meniscus. b) Evolution of the F 1s binding energies of the main components as a function of applied voltage. . . . . 92

3.24 a) C 1s XPS spectra measured during discharge at the PC+VC||GC interphase. b) Evolution of the C 1s binding energies of the main components as a function of applied voltage. . . . . 93

3.25 a) O 1s XPS spectra measured during discharge at the PC+VC||GC interphase. b) Evolution of the O 1s binding energies of the main components as a function of applied voltage. . . . . 94

3.26 a) F 1s XPS spectra measured during discharge at the PC+VC||GC interphase. b) Evolution of the F 1s binding energies of the main components as a function of applied voltage. . . . . 95

4.1 Sketch of the *in situ* electrochemical cell for *operando* HAXPES in LIBs. . . 98

4.2 Lateral view of the cell showing the carbon coated $Si_3N_4$ chip (a), the O-rings (b1,b2), the glassy fiber separator (c), and the Li metal as anode (d). On the right panel, a picture of the cell inside the glovebox is shown (e). . 98

4.3 Geometric scheme used to estimate the incidence angle $\beta$ for the chip design. 100

4.4 a) Survey simulation of our system composed of $LiPF_6$ electrolyte in EC+EMC under 5 nm of amorphous carbon and 20 nm of $Si_3N_4$, at different photon energies ; b)–d) close up of three main core peaks. . . . . 101

4.5 Model used for the SESSA simulations. . . . . 102

4.6 a) Pristine membrane before assembling; b) broken membrane after rough pumping from 1 bar to $10^{-3}$ mbar; c) intact membrane after slow pumping from 1 bar to $10^{-3}$ mbar. . . . . 103

4.7 XPS survey of a coated 30 nm-thick $Si_3N_4$ membrane at $h\nu = 6.9$ keV (broken membrane). . . . . 104

4.8 XPS survey of a coated 30 nm-thick $Si_3N_4$ membrane at $h\nu = 6.9$ keV (broken membrane). . . . . 105

4.9 a) Schematic drawing of the BLG chip (top view); b) successfully assembled cell c) cell busted after pumping. . . . . 106

4.10 Cyclic voltammetry using the *in situ* cell with the BLG chip: in red the voltage step procedure, in blue the standard CV. . . . . 107

4.11 XPS survey obtained on the BLG cell (blue) along with the simulated spectrum (red). . . . . 108

4.12 HAXPES C 1s (a) and F 1s (b) core levels collected at $h\nu = 6.9$ keV upon discharge. . . . . 109

4.13 chip structure and sizes. In blue, $Si_3N_4$, in dark orange Pt, in light orange the membrane. . . . . 110

4.14 Elecrochemical Procedure for the homemade sputtered chip. In (a), the stepped applied voltage as a function of time and the related current flowing. In (b) the resulting CV curve. . . . . 111

4.15 Measurement of N 1s (a) and O 1s (b) gas phases through the membrane (red) and through the carbon coated membrane (green) compared to an empty cell. . . . . 112

4.16 Survey spectra of an electrolyte filled cell with a 15 nm membrane . . . . . 112

4.17 Main core peaks (C 1s, O 1s, F 1s) coming from the electrolyte below the membrane. OCV at $h\nu = 8$ keV . . . . . 113

5.1 Vertical scan over the C 1s core peak on the silicon electrode. Depending on the vertical position, different phase were observed (a) the Si substrate + PC gas phase, (b) bulk PC liquid meniscus and (c) the Si substrate and PC wetting layer. . . . . 117

5.2 Vertical scan over the Si 1s core peak on the silicon electrode. Depending on the vertical position, different phases were observed (a) the Si substrate + PC gas, (b) no signal due to the bulk PC thick meniscus, and (c) the Si substrate and the PC wetting layer, coherently with the C 1s XPS data. . . 117

5.3 Model for a possible improvement of the inner side of the chip with a grid of Pt (or Au or other conductive material) acting as a current collector . . . 118

# List of Acronyms

- **AFM**: Atomic Force Microscopy
- **BE**: Binding Energy
- **BIG-MAP**: Battery Interface Genome - Material Acceleration Platform
- **CV**: Cyclic Voltammetry
- **DCM**: Double Chrystal Monochromator
- **FT-IR**: Fourier Transform Infrared Spectroscopy
- **HAXPES**: Hard X-ray Photoelectron Spectroscopy
- **HRM**: High Resolution Monochromator
- **HSA**: Hemispherical Sector Analyzer
- **IMFP**: Inelastic Mean Free Path
- **LIB**: Lithium Ion Battery
- **LINAC**: Linear Accelerator
- **LNO**: Lithium Nickel Dioxide
- **MED**: Mean Escape Depth
- **NIST**: National Institute of Standards and Technology
- **NAP-PES**: Near Ambient Pressure Photoelectron Spectroscopy
- **OCV**: Open Circuit Voltage
- **SEM**: Scanning Electron Microscopy
- **SEI**: Solid Electrolyte Interphase

- **SESSA**: Simulation of Electron Spectroscopy for Surfaces Analysis
- **SICM**: Scanning Ion Conductance Microscopy
- **STM**: Scanning Tunneling Microscopy
- **TEM**: Transmission Electron Microscope
- **UHV**: Ultra High Vacuum
- **XPS**: X-ray Photoelectron Spectroscopy
- **XRD**: X-ray Diffraction
- **XRS**: X-ray Raman Scattering

# Chapter 1

# Introduction

Since the first industrial revolution at the end of the $17^{th}$ century, fossil fuels had seen an exponential increase in their utilization [1]. In more recent years, however, the use of fossil fuels and the related $CO_2$ emission have been linked to the several alarming phenomena collectively known as "Climate Change" [2]. Adopted in 1997 by 192 countries, the Kyoto protocol [3] has been the first of many initiatives aimed at reducing the $CO_2$ emissions, identified as the main responsible of the world-wide increase of the average temperature. As a further reason to move from these energy sources, it has always been clear how the extensive usage of fossil fuels is not compatible with their intrinsic nature of non-renewable and limited sources, as has been shown for example during the oil crisis in 1973.

For these reasons, shifting to new, renewable energy sources is one of the main goals for the $21^{st}$ century societies. Photovoltaic, wind power, hydroelectric power, are all different examples of renewable, sustainable energy sources, that can provide electricity without having to rely on the combustion of fossil fuels, or having to deal with their emissions. Yet, all these renewable energies bring new challenges. Among them, the intermittence of the natural phenomena that are relied upon to produce electricity is one of the major issues: often, there will be cases of high energy production but low energy demand, while in other moments, the demand could be higher compared to the actual output. For this reason, energy storage solutions play a central role in linking the electricity production plants to the actual grid [4], working both as a vessel for the exceeding energy in situation of low de-

mand, and as an additional source of energy when necessary, thus stabilizing the electric grid. Moreover, the shift from thermal combustion engines to electrical-based ones for the transportation vehicles, would also further reduce the $CO_2$ emission as well as any other hazardous emission coming from combustion engines [5], as already promoted by the "European Green Deal" approved in 2020 [6]. Among the adopted initiatives, a law stopping the production of thermal motors after 2035 is a clear example of how there will be a strong need for reliable systems for the energy storage applicable in the automotive sector, in order to exploit the green energy produced by sustainable sources and reduce emissions in the cities. Ultimately, electronic devices are becoming more and more relevant in the everyday life, and their growing performances requires long lasting high-capacity rechargeable batteries. The best way to answer the need for portable and performing energy storage solutions has been identified in the latest 30 years mostly in the rechargeable lithium-ion batteries (LIBs), even with recent exceptions of notable system such as sodium-ion batteries (NIBs), that are becoming popular for some stationary or high-power applications. The interest in LIBs is noticeable also in the research done over the last 20 years, as can be seen in Figure 1.1, where the total of publication on the "Li-ion batteries" topic has been plotted using the Dimensions® online database over time, from 1974 to 2024 [7].

## 1.1 Li-ion batteries

In 1817, Arfwedson and Berzelius discovered lithium by analysing petalite ore ($LiAlSi_4O_{10}$), when they recorded the presence of a new element with several similarities to potassium and sodium. One year later, in 1818, Christian Gmelin reported that lithium salt gave a bright red colour in flame, but it wasn't until 1821 that lithium could be isolated, through electrolysis of lithium oxide thanks to the work of William Thomas Brande. Lithium was then studied in the early 1958 in relation to its solubility in different non-aqueous electrolytes by William Harris, who noticed the formation of a passivation layer on the lithium that would prevent further interaction with the electrolyte while allowing ion conduction: lithium was just starting to show its potential for battery systems. After these first discover-

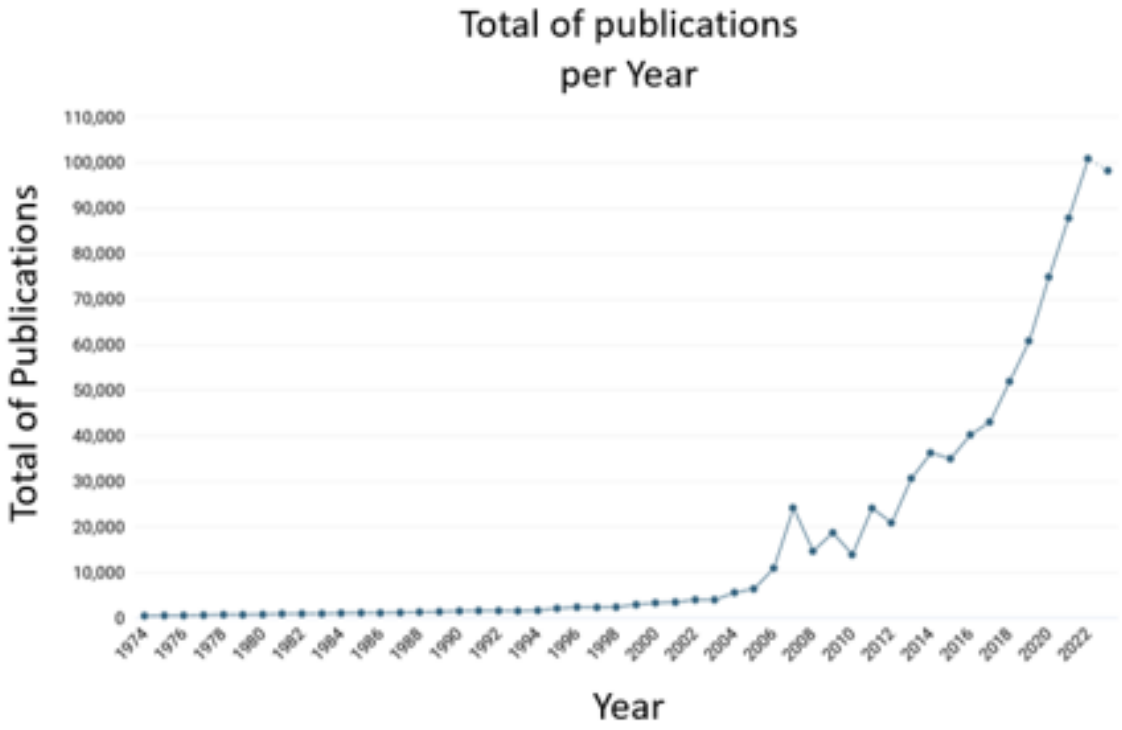


Figure 1.1: Total of publications per year as a result of the query "Li-ion batteries" on the "Dimensions.ai research database". [7].

ies, several electrochemical cells based on lithium ions with non-aqueous electrolytes, such as Li/$SO_2$ with various combinations of solvents and salts for the electrolyte [8] (1969) and $LiMnO_2$ with 1M $LiClO_4$ in 1.3-dioxolane [9] as an electrolyte (1975) were developed and commercialized. However, these primary batteries were non-rechargeable and presented safety issues, related to the Li plating/stripping processes and the formation of dendrites: in fact, conditions such as high charging rate or low temperatures of the battery promotes a deposition of the Li ions on the surface of the anode instead of the desired intercalation process [10]. This has two primary consequences: lithium ions involved in the deposition process transform into lithium metal that no longer participates in electrochemical processes; these formations often give rise to the so called dendrites, metallic structures with a branching structure that grows from the electrode, and that can provoke short circuits, as well as representing a loss of active material in the system.

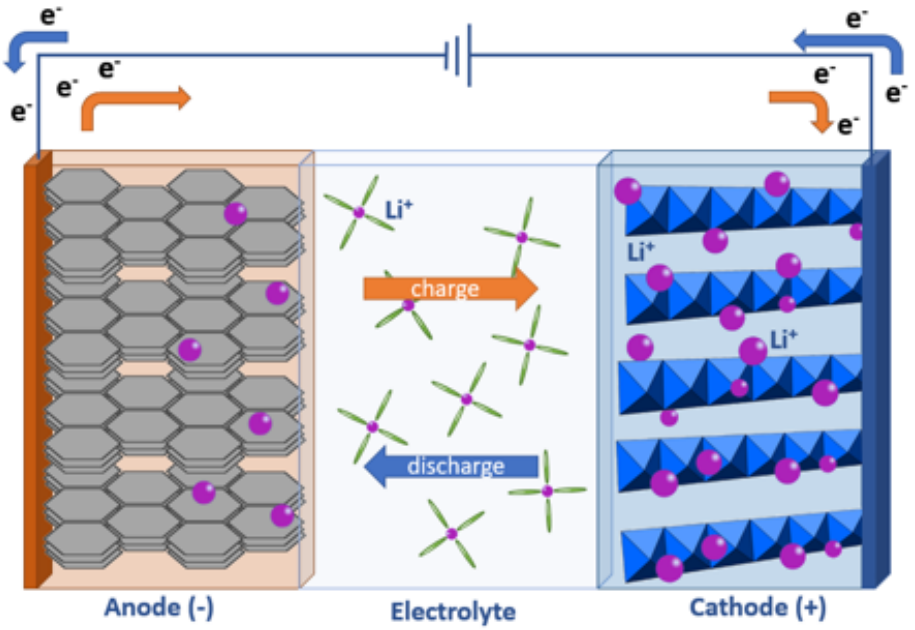


Figure 1.2: Schematic functioning of a Li-ion battery.

The first studies on rechargeable electrochemical cells based on lithium ions and intercalation cathodes have been conducted in the 1970s [11], [12] by John Goodenough, Stanley Whittingham and Akira Yoshino, and then awarded in 2019 with the Nobel Prize for Chemistry. Due to difficulties in stabilizing the system, however, the release of rechargeable lithium-ion batteries on the market waited up until 1991, with the first commercial release by SONY and Asahi Kasei.

The functioning of rechargeable LIBs is based on the so-called "rocking chair" mechanism. The use of redox intercalation materials at the positive electrodes (cathodes) and graphite at the negative electrodes (anodes) allows the lithium ions, the actual energy carriers in the system, to be able to go back and forth between the two electrodes through the electrolyte, without having to rely on a lithium metal electrode as source of $Li^+$ ions. The implementation of redox intercalation materials was a crucial step to avoid the use of metallic lithium electrodes in rechargable systems: due to the high reactivity of lithium, in fact, they would rapidly deplete, also forming lithium dendrites on its surface through the several cycles, and thus performing badly on the long term, as well as generating safety issues due to the short circuits [13], [14].

The scheme of a typical Li-ion battery is shown in Figure 1.2 where its shown that it has three main components: two electrodes and the electrolyte. The electrodes are the host materials that exchange the Li ions during charge and discharge. During the charging of a LIB, the electrode receiving the $Li^+$ is referred to as the negative one, and called anode, and in modern rechargeable LIBs is composed of graphite (left orange side in the scheme picture). On the other side, the positive electrode is called cathode (right blue side). Several materials have been used as cathodes, but the most structurally stable and with higher capacity are the layered transition metal oxides [15]. Lastly, the electrolyte ensures the $Li^+$ conduction while being electrically insulating. A separator, usually a polymer or a glassy fiber membrane, ensures the ionic conductivity and acts as a physical electric insulator between the two electrodes to avoid any contact. Nowadays, electrolytes are composed of a wide range of carbonate organic components mixed with $Li^+$ salts.

During charge, the transition metal ions in the cathode get oxidized and $Li^+$ are de-intercalated from the positive electrode. The $Li^+$ ions move through the electrolyte to the anode side, and they are inserted into the graphite interlayer, forming the $LiC_6$ alloy. During the discharge, in a symmetrical process, the $Li^+$ moves back from the graphite anode to the cathode, reducing the positive electrode and oxidizing the negative one.

Most of the studies focused on improving the performances of the main components of the battery: the electrodes and the electrolyte. However, focusing on the single component is not sufficient to improve the whole battery performances because how these parts interact with each others must be also considered. In particular, the specific interaction between the liquid electrolyte and the solid electrode is one of the most important topic in LIBs: in fact, during the first cycles of LIB, the electrolyte gets reduced on the surface of the negative electrode, forming a solid passivation layer that has the electrolyte characteristics of being ion-conducting but current insulating. For this reason and its double nature, this important layer has been called “Solid Electrolyte Interphase” (SEI) [16], [17].

### 1.1.1 Significant parameters in LIBs

In order to understand and define the performances of a battery, significant parameters have been identified over time. Firstly, the **voltage** V of a battery is defined as the difference in electrical potential of the two electrodes, as

$$V = E_+ - E_- \tag{1.1}$$

Then, is possible to define the **theoretical gravimetric capacity** Q as the quantity of electrons (or $Li^+$) that can be exchanged per unit of mass, calculated on the base of the molar mass M of the electrode compound, the quantity $\Delta$x of energy carriers ($Li^+$ or electrons) exchanged per formula unit, and their charge z, as

$$Q = \frac{\Delta x \cdot z \cdot F}{3.6 \cdot M} \, [mAh \cdot g^{-1}] \tag{1.2}$$

where F stands for the Faraday's constant ($965 \cdot 10^2 C \cdot mol^{-1}$). The **experimental gravimetric capacity** $Q_{exp}$ can be calculated experimentally as

$$Q_{exp} = \frac{I \cdot (t_1 - t_0)}{3.6 \cdot m} \, [mAh \cdot g^{-1}] \tag{1.3}$$

where m is the mass of active material, I the current and $(t_1 - t_0)$ the time interval. A discrepancy is often observed between the theoretical and experimental capacity, due to the $Li^+$ ions involved in parasitic reactions. For this reason, the number of electrons reversibly exchanged in a full charge-discharge cycle is used, and the **coulombic efficiency** is defined as

$$CE = \frac{Q_{discharge}}{Q_{charge}} \tag{1.4}$$

Where $(1 - CE)$ indicates the amount of $Li^+$ ions irreversibly lost in the parasitic reactions. It is important to remind that a charged battery can get slowly discharged while on rest. The ability to retain charge during the rest periods is called **retention capacity**. This is defined as the ratio of the discharge capacity at cycle *n + 1* over the capacity at the cycle *n*.

When considering the applications of batteries in real systems, other parameters are often used to such as the **energy density** (in $Wh \cdot kg^{-1}$ or $Wh \cdot L^{-1}$) and **specific power** (in $W/kg$ or $W/L$).

## 1.2 The solid-electrolyte interphase

The electrolyte plays the role of electrical separator and ionic connector between the anode and the cathode. Its chemical compatibility with both electrodes and the intrinsic electrochemical stability of the couple electrode/electrolyte in a wide voltage window have to be guaranteed in order to have a functioning battery. Moreover, to ensure the reversibility of reactions along the cell operation, the electrochemical potentials of the anode and cathode must be within the potential window defined by the lowest unoccupied and highest occupied molecular orbitals (LUMO and HOMO) of the electrolyte. However, during the battery operation, the thermodynamic stability window of the carbonate-based electrolytes [18], [19] is smaller than the applied voltage. This translates to a reduction (or oxidation) of electrolyte species on the surface of the negative (or positive) electrodes, forming the solid-electrolyte interphase (SEI). The SEI, passivating the surface of the electrode and preventing further reduction (or oxidation), expands the exploitable voltage window of the system as shown in figure 1.3

The formation of the SEI occurs during the first cycle of the battery, and it induces an initial capacity loss. This can be explained by the consumption of Li ions during the electrolyte reduction, that results in the reduction of capacity: in fact, up to a $10\%$ of total capacity is consumed in irreversible processes during the first cycle [20]. This loss is however accepted since, thanks to its electronic insulating but ionic conducting character, the resulting SEI acts as a solid thin layer that passivates the electrode and prevents continuous degradation of the electrolyte upon further cycles. Indeed, a stable SEI becomes essential to ensure high coulombic efficiency and long-life span in LIBs, also allowing to exploit higher

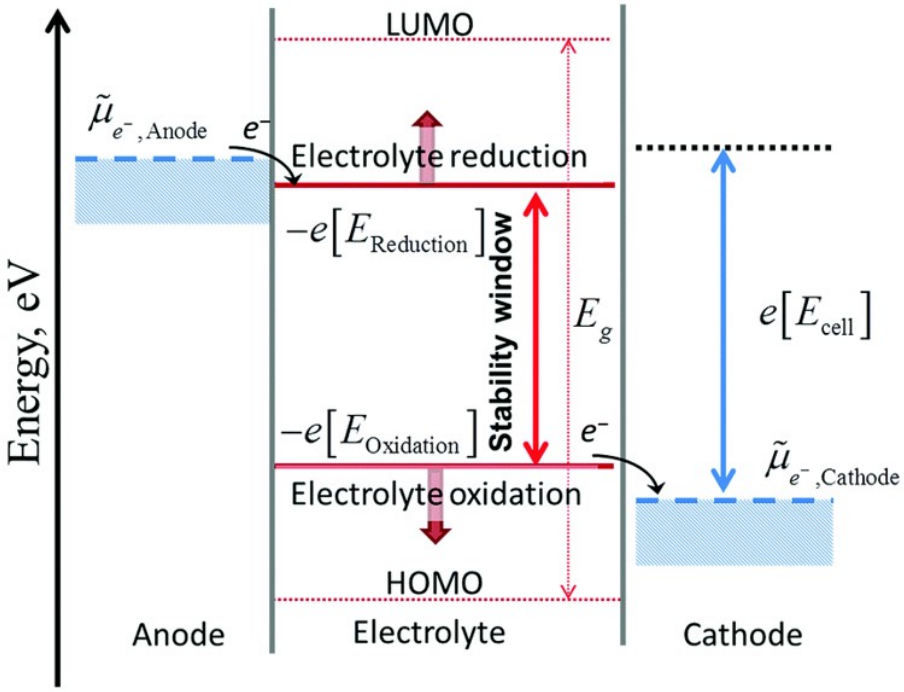


Figure 1.3: The HOMO and LUMO energy levels of the electrolyte defining the battery stability window and the electrode working potentials. [18]

power through the widening of the effective thermodynamic stability window of batteries. It is important to note that to achieve this goal, the whole surface of the anode has to be covered by the SEI, meaning that there is a consumption of active material in the formation of it, and a loss of capacity, that is strictly related to the surface of the electrode that has to be passivated. To avoid this, a first solution that comes to mind could be to highly reduce the surface of the anode: indeed larger anode surfaces imply higher quantity of material lost to passivate them, and thus a greater loss of active material. However, choosing to reduce the size of the anode to have less surface to passivate would also mean a loss in the power density of the battery, as well as another unwanted processes: when the anode has a smaller capacity than the anode, lithium plating and dangerous formation of lithium dendrites that could lead to internal short circuits happens. Actually, to avoid this, the capacity ratio between anode and cathode is usually kept at around 1.1 A/C, and thus reducing the exposed area of the anode surface is not the right option to avoid high reduction of species during SEI formation, and it must be accepted that an initial capacity loss due to the SEI

formation is unavoidable [21]. The best solution is actually to form a stable SEI layer, so that after the first formation, any further loss of material is prevented.

The important role of SEI formation for the proper functioning of a battery was firstly assessed by Peled in 1979 [22] for the case of metallic lithium batteries, and its importance can be seen in how the first lithium / graphite batteries were brought on the market only in 1990, eleven years later, after an extensive research effort allowed to understand the SEI formation process well enough to allow their commercialization [23]. Indeed, understanding the process of formation of the SEI depending on the electrode/electrolyte couple, formulation of the electrolyte and cycling condition, has been since then a major goal in LIB research; however only partial information has been achieved. Over the last 30 years, most of the information and knowledge about this interphase have concerned the identification of major species forming the SEI, while the process through they form is still under debate. This is also due to the intrinsic nature of SEI: being a buried interphase of nanometric thickness and being extremely sensitive to air and impurities, most of the studies on the SEI have been conducted using *ex situ* characterization protocols. For this purpose, the electrodes were first cycled in a coin cell up to the desired state of charge; the coin cell was then disassembled inside an argon filled glove-box and the electrodes recovered, rinsed in solvent and dried under vacuum. Finally, the electrodes were transferred to the analysing chamber. This sample preparation can strongly alter the retrieved information, for example on the expected organic species forming the SEI that are soluble in the solvent [24], [25], resulting in a partial picture of the expected process. This calls for new approaches able to capture the SEI formation and stability.

### 1.2.1 The SEI formation and composition

The formation process of SEI is a highly debated topic, because it is influenced by many factors, such as the electrolyte formulation, the electrode coating and the cycling conditions. However, some consensus has been achieved on the expected formation mechanism.

As already mentioned, the SEI is formed as a result of a two-step process involving first

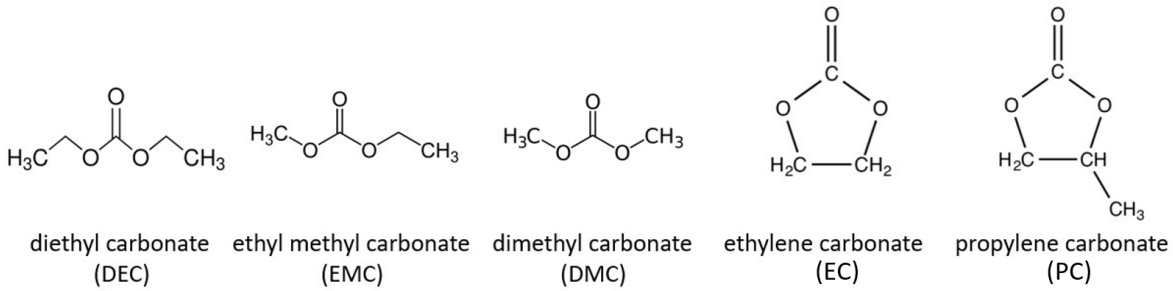


Figure 1.4: Molecule structures for some popular solvents used in Li-ion batteries.

the polarization of the electrode and the subsequent reduction of the electrolyte components as the lithium ions, salts, solvents and impurities, and then the precipitation of the formed chemical species on the surface of the anode. This process is very complex as it starts for the different components at different times, in relation to their instability when the electrode reaches potentials out of their operating window. For the anode, this happens around 1V vs $Li^+/Li$, when the voltage is lower than the LUMO related to the reduction potential of organic carbonates, the main components of electrolyte solvents in LIBs. Most of the electrolytes used in LIBs contain these acyclic carbonates, as diethyl carbonate (DC) or dimethyl carbonate (DMC) or ethyl methyl carbonate (EMC) as well as cyclic carbonates as the ethylene carbonate (EC) whose structure is shown in fig 1.4. Especially the cyclic carbonates as EC have been shown to be necessary to obtain stable SEI and thus a prolonged cycling life [26]–[28].

Several processes take part and compete each other on the surface of the graphite electrode during $Li^+$ insertion. Their rates differ based on their reductive potential, reduction activation energy or exchange current density. Also, besides these intrinsic proprieties, it has been shown how reaction sites, temperature, concentration of the electrolyte salt and reduction current rate also affect SEI formation [29]–[32]. For example, studies made on highly ordered graphite have shown that the SEI growing on the edge plane, where more reactive sites are present, results to be several times thicker than the one grown on the less reactive basal plane [33]. For these reasons, SEI formation mechanism is hard to exactly pinpoint.

Some processes are however generally accepted: usually, at first the $LiPF_6$ salt reduces in the form of LiF or $Li_xPF_y$. Then, the carbonates of the solvent decompose following different possible pathways that depends on the specific carbonate involved, if it is part of a solvation shell for a Li ion, and if it is a one or two electron process. The results comprehend gaseous species as $CO_2$ as well as species commonly reported in the SEI like $Li_2CO_3$ or lithium alkyl carbonates (such as $ROCO_2Li$). However, these are not the only possible players in the SEI formation. The use of additives in the electrolyte mixture as Vinylene Carbonate (VC) also influences the SEI formation. Indeed, the reduction of VC implies the formation of more stable species than in solvents as EC, undergoing decompositions producing species as poly-Li alkyl, polycarbonates, alkoxides, Li-carbides and oligomers [34]. These products are believed to further polymerize the electrode surface thus building a more effective SEI [35], improving the Li transport and electrode passivation.

Additionally, even if LIB manufacturing tries to keep contaminant as low as possible, small traces of water are often unavoidable, being present both in the electrolyte and adsorbed on the electrode surface. Water is extremely reactive and in the battery environment produces inorganic components as lithium carbonates. This adds up to the fact that for example it has been observed that LiF could be found in greater abundance both after destructive surface analysis measurements or when it reacts with traces of HF coming from the interaction of decomposition products of $LiPF_6$ with traces of water, that could come either from sample pollution or non-inert atmosphere during the measure, adding another level of uncertainty on the SEI composition. It is believed that the HF produced through the reaction of water with reduction products particularly tends to affect dramatically the performances of LIBs by attacking the SEI layer, while other polluting compounds can react at the charged interface, reacting with both the SEI components and the solvent molecules, altering the composition and performances of both. This underlines the importance of assembling the battery in inert atmosphere to obtain durable LIBs [36]–[38].

Problems arise also when the *ex situ* sample is prepared: for surface-sensitive techniques as XPS, the electrode surface must be rinsed with solvent and then dried before the mea-

surement can be performed. This is because an excess of solvent and salts coming from the electrolyte would not allow a good measurement of SEI. However, the outer organic layer of SEI has several metastable components that inevitably undergo reactions, as the lithium-alkyl carbonates, while outer species derived from the salt decomposition could get washed away during the rinsing [24], [39]. This means that the process needed to perform *ex-situ* measurements also inevitably brings changes to the SEI composition.

Another important issue is related to the formation of $Li_2O$ species: while it has been often reported to be present in the SEI, it was later argued that it could be actually a result of Ar+ sputtering, a technique often used to analyse the depth profile of the different SEI layers by XPS. In fact, it has been observed that the $Li_2O$ arises from the $Ar^+$ sputtering on $Li_2CO_3$ compounds ($Li_2CO_3 \rightarrow Li_2O + CO_2$). In a similar process, also X-ray beam damage has been reported to produce $Li_2O$ [40]. It is thus evident how, while there is a wide understanding of the species that compose the SEI, some points are still unclear. Clearing these points and unraveling the mechanisms behind the SEI formation, and how they are related to its stability during cycling, would be an important step for batteries research.

### 1.2.2 The SEI structure and its dependence on the anode structure

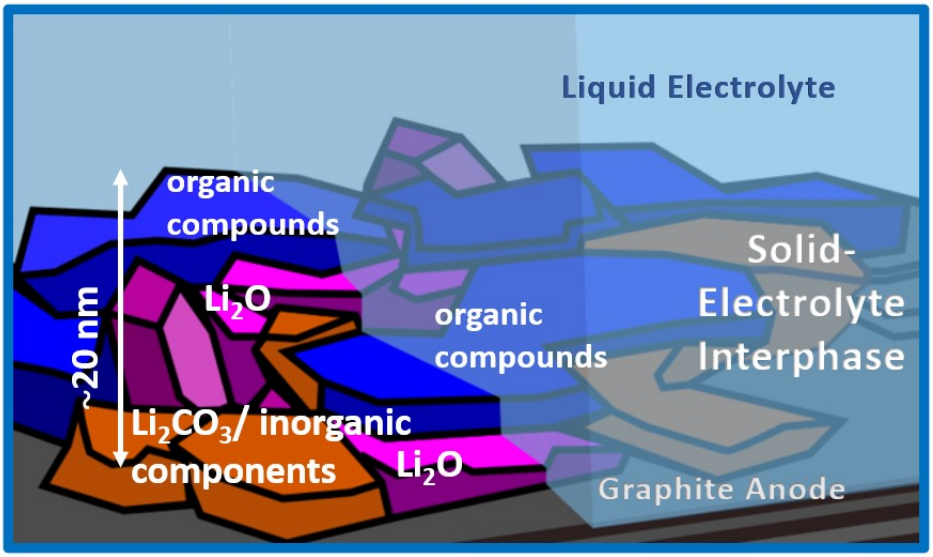


Figure 1.5: SEI structure and composition.

Together with the composition, the structure of SEI represents a highly important and debated topic. Understanding its nanostructure upon the interphase formation and the influence of different carbon substrates is crucial to further improve the design of LIBs.
SEI is usually described as composed of two main "layers". The closer one to the anode surface is formed at the very start of the formation process and it is made by inorganic species: these are electron insulating components coming from the degradation of salts, as LiF or $Li_2CO_3$, and generally have low porosity and dense morphology. The outer layer, in direct contact to the liquid electrolyte and forming later on, is made of organic compounds coming from the degradation of the electrolyte solvents, and it is described as more porous and soaked with the electrolyte [41], [42].
However, the SEI structure is not as simple as the double layer description may imply. In fact, this description identifying two "layers" oversimplifies the structure that has been instead described more as a "mosaic" one, where the different compounds interlock together to form the SEI, as shown in figure 1.5. In this case, there is no sharp separation between the inorganic and organic layers, and the the components are distributed in a more blended way.
It has also been observed that the thickness of these different layers is highly depending on the specific structure of the carbon substrate used as anode. The importance of the nanostructure of the anode in relation to the SEI growth has been underlined by studies performed on highly ordered pyrolytic graphite (HOPG). This material has the same composition of graphite, as it is composed of a stack of graphene planes, but is different in the order of these graphene planes, that is more coherent and on a bigger scale compared to the mesh of small micro and nano regions of ordered planes that compose graphite [43]. This gives the HOPG the interesting property of having two easily distinguishable planes: one, parallel to the graphene planes, is generally referred to as "basal plane" while the other, perpendicular to the planes, is the "edge plane". Similar to a graphene sheet, the basal plane does not present many dangling bonds and is less electrochemically reactive than the edge plane, that has instead many more active sites [44]. This impacts on the elec-

trochemical behaviour of basal and edge plane and therefore the SEI formation on them. The edge plane usually shows a thicker SEI, in accordance to the higher reaction current observed on it [33]. This SEI is mainly composed of an inner inorganic layer, of mostly LiF and $Li_2CO_3$, and an outer organic layer, composed of organic lithium alkali carbonates, polymeric compounds and inorganic lithium carbonates in a loose arrangement. On the basal plane, instead, lithium carbonates are more present than LiF. Ideally, since on this plane $Li^+$ cannot easily intercalate, the basal plane area of an electrode does not contribute to the reversible capacity of LIB and its SEI should be electron insulating and impermeable to the electrolyte components, without the need to be ion conducting [45], [46].
Previous studies conducted on graphene and on glassy carbon showed that the former behaves like the basal plane of graphite, while the latter is closer to the behaviour of the edge planes [47], with the sole exception of not allowing Li-ion intercalation, in accordance to possible predictions based on the similarities in the structure of these composites [46]–[48].

### 1.2.3 Characterization of the SEI

In this paragraph, we give an overview of the morphological, structural and chemical information retrieved on the SEI by several characterization techniques. Before detailing the different techniques and their capabilities, it is important to introduce two different terms that will be used henceforth. As already said, SEI is composed of highly reactive species with a metastable character. This brings forth the need to distinguish between three types of approaches:

- *ex situ*: the SEI is analysed after the electrode has been extracted from the cell and the reaction has happened;
- *in situ*: the SEI Is analysed directly inside the cell, and the electrochemical measurements are stopped during the measurements;
- *operando*: the SEI is analysed while the cell is working, therefore the measurements

can monitor the whole reaction processes.

### Morphology and structural information by imaging methods

Microscopy is an important method to observe morphological changes in the SEI. Different microscopy techniques have been used for both *in situ* and *ex situ* measurements.
The most used laboratory-based microscopy techniques are Scanning Electron Microscopy (SEM) and Transmission Electron Microscopy (TEM). TEM allowed *operando* measurements of SEI deposition on a glassy carbon electrode thanks to a specially designed cell [49], while SEM has been used to morphologically characterize the SEI in *ex situ* conditions [50]. These techniques use electrons to obtain a clear picture of the sample with a nanometric spatial resolution. While SEM collects the scattered electrons and thus obtains very precise information on the surface of the sample, TEM analyses the transmitted electrons, thus obtaining information on the inner structure. However, both these techniques require vacuum due to the low mean free path of electrons, and this limits the choice of electrolytes to those with low vapor pressure, as ionic liquids, polymers, or ceramic-based ones. Moreover, high energy electrons induce damage to the sample, constituting a further drawback for these techniques [49]–[51]. TEM also requires thin samples, meaning that the sample must be prepared accordingly through destructive procedures. Other possible techniques are Atomic Force Microscopy (AFM), Scanning Electrochemical Strain Microscopy (CESM) or Scanning Ion Conductance Microscopy (SICM), all of them offering further perspectives for the investigation of SEI proprieties and evolution [52]–[54]. AFM coupled with electrochemical measurements (EC-AFM) make possible to directly follow the formation of the interphase during the battery electrochemical cycling [55]. Similarly, Scanning Tunnelling Microscopy (STM) enables *operando* measurement of SEI (EC-STM), coupling the growth of SEI on the electrode surfaces with the electrochemical changes [56]. All these techniques, however, are missing the chemical sensitivity needed for the identification of the growing or depositing species, as they provide only morphological information of SEI.
Synchrotrons provide high intensity and high energy X-ray beam, thus widening the range

of possible applications. One of them is the Transmission X-ray Microscopy, providing 2D projection of the sample and, by rotating the sample, the complete 3D reconstruction. This technique is compatible with *in situ* measurements in tailored cells, and it has provided information on the growth of SEI or the cracking of anode particles during cycling, both in the bulk and at the interface [57]–[59]. Combination of Computed Tomography with X-ray Diffraction (CT-XRD) and Pair-Distribution Function (CT-PDF) [60], [61] are emerging techniques for the determination of the species growing on graphene and thus correlating the formation of crystalline LiF with the presence of amorphous species and during the lithiation process [62].

**Chemical information by spectroscopy techniques**

Spectroscopy is the suitable tool to understand the chemical changes occurring at the interphase during the electrochemical processes, but the development of tailored electrochemical cells is a crucial step to overcome the experimental constraints, and the adaptation of the electrode preparation is mandatory.

Vibrational spectroscopies as Raman Spectroscopy or Fourier Transform Infrared Spectroscopy (FT-IR) are powerful tools to obtain real-time information through a non-destructive laser beam, that can preserve the integrity of the sample. With these techniques, the reaction mechanisms at the interface of the electrode/electrolyte can be investigated: *in situ* IR spectro-electrochemical experiments are used for monitoring the soluble products, the intermediates and the reactants of electrochemical reactions [63], [64], while *in situ* spectro-electrochemical Raman tracks the intermediate species and reaction products [65], [66]. The many different species forming the SEI, composed mainly of light elements, and their heterogeneous distribution through the nanometric-thick SEI represent a drawback for the understanding of this interphase. X-ray photoelectron spectroscopy (XPS) has a strong chemical sensitivity to different species and light elements, with the capability of probing nm-thin interfaces [67]. However, XPS is limited by both the low probing depth of photoelectrons and the ultra-high vacuum (UHV) environment where it operates in relation to

the possibility to access to the SEI. For this reason, most of the SEI studies using XPS were performed on *ex situ* electrodes, especially in the case of conventional laboratory XPS using Al X-ray sources.

Thanks to the possibility to obtain high energy and high intensity X-rays in a wide range of energies, synchrotron spectroscopic techniques offer more possibilities than laboratory-based ones. In particular, X-ray Raman Scattering Spectroscopy (XRS) circumvents surface limitations and provides bulk information on light elements using hard X-rays (X-rays with energies in the range of the tenths of keV) [68]. Synchrotrons have also expanded the capabilities of XPS measurements: Hard X-ray Photoelectron Spectroscopy (HAXPES) uses high energy photons to produce photoelectrons with higher kinetic energy. This means that the relative escaping depth is higher than in conventional XPS, allowing to have a non-destructive depth profiling of a sample by scanning the incident energy [69]. Moreover, the high beam intensity available at synchrotrons coupled with a dedicated differential pumping setup give the possibility to perform Near Ambient Pressure Photoelectron Spectroscopy (NAP-PES), thus enabling the direct access to the solid-liquid interface through thin layers of liquid [70]. However, *in situ* spectro-electrochemical approaches based on XPS have not yet been fully developed.

## 1.3 The BIG-MAP project

The central role of LIBs has been recognized by the European Commission with the launch of the European Battery Alliance and the BATTERY 2030+ initiative [71]. As a part of this initiative, the Battery Interface Genome - Materials Acceleration Platform (BIG-MAP) has been instituted to develop an unique R&D infrastructure and accelerated methodology to discover new battery materials using artificial intelligence, high performance computing, large-scale and high-throughput characterization and autonomous synthesis robotics [72]. To reach this goal, BIG-MAP efforts were divided between several objectives. The first one was to answer the need to coordinate all the partners and standardize sample preparation

between the different laboratories. Then, while simulation tools were developed to describe the different processes occurring in the LIB, a great set of experiments had to be done between the different laboratories, to accumulate data to be used to improve the simulations. Within the framework of the BIG-MAP project, the aim of my PhD thesis is to develop novel XPS-based approaches to better understand and characterized the solid electrolyte interphase using standardized protocol and materials, thus providing reliable and robust information.

### 1.3.1 BIG-MAP materials

In the framework of the BIG-MAP project, the materials were shared among all the partners. Here is a brief introduction and description about them:

#### Graphite

Graphite exhibits a layered structure made of disordered stacks of graphene planes, where the carbon atoms are arranged in hexagonal lattice. Thanks to its high electrical conductivity and low thermal conductivity, together with its low cost and high abundance, graphite is the most common material chosen for the fabrication of negative electrodes in LIBs. It's layered structure allows easy intercalation of the $Li^+$ that then bonds with carbon atoms in $LiC_6$ compounds [73]. Some limitations as the creation of irreversible Li-C structures, the low capacity and slow kinetics for the insertion mechanism did not hinder graphite to become the most used material for anodes in LIBs.

#### Lithium Nickel Dioxide $LiNiO_2$ (LNO)

LNO is a layered cathode material which is regaining interest as positive electrode in LIBs. Considering its theoretical capacity close to 275 mAh/g and the working potential related to the $Ni^{3+}/Ni^{4+}$ redox couple (4.3 V vs $Li^+/Li$), LNO was an attractive alternative to $LiCoO_2$. The first studies on LNO in 1990s had however already evidenced major drawbacks in terms

of stability at high potential and decomposition upon cycling, thus preventing its commercial application. The mitigation of such issues was possible by partially substituting the Ni by Co and Mn in exchange for a lower capacity, and the doped $LiNi_{1-x}Co_xMn_xO_2$ (NMC) compounds have been targeted for some portable applications. However, the automotive industry always ask for higher capacity material, thus needing a lower amount dopants, and actually getting closer to the pure LNO formulation. For this reason, the material had seen a new rise in interest that asks for a deeper understanding of the intricate interplay between its structural and electronic properties, with a special attention to the parasitic reactions responsible for capacity and voltage fading over cycling[74].

#### LP57

LP57 is a common electrolyte solution composed of 1M of $LiPF_6$ in EC: EMC = 3:7 volume ratio. It is the electrolyte of choice for the BIG-MAP project due to its good performances and established presence in the battery market, showing good SEI formation capabilities and being easily accessible. Studies to further improve its performances are being made, involving the use of additives in the mixture.

### 1.3.2 Other materials used in this project

The use of BIG-MAP materials was not possible due to several experimental constrains met during this work. In that case, other materials have been used:

#### Glassy Carbon (GC)

Glassy Carbon, or vitreous carbon, is a carbon composite often used in electrochemistry. Its chemical structure sees the carbon atoms arranged in a very disordered but compact way, thus allowing many active sites for electrochemical reaction while preventing most of the intercalation processes. For this reason, it is possible to use it to focus on the specifics of processes happening at the surface of the electrode without having to take into account for

the intercalation of $Li^+$. Its structure also has a strong similarity in results compared to the edge planes of graphite.

### Graphene

Graphene can be described as a single plane of graphite, with the carbon atoms ordered in an hexagonal lattice [75], forming an atom-thin membrane. Graphene has interesting physical and mechanical properties as high electronic conductivity and high resistance to mechanical strain. In our case, graphene works as an ideal carbon-based anode, similar to the basal plane of graphite in terms of active sites but also thin and resistant enough to be used as a window.

### Propylene Carbonate (PC)

PC is one of the possible solvents used for LIBs. While its low melting point and high vapor pressure make it interesting for the use in LIBs, it has been rarely used because PC can be intercalated in the graphite planes together with the $Li^+$ ions, exfoliating the graphite planes and highly reducing the reversible capacity of the systems [76], [77].

### Ethylene Carbonate (EC)

While EC has a structure similar to PC (as can be seen from figure 1.4), its performances related to LIB and SEI formation are very different: EC forms a thinner but more stable SEI [78], [79] compared to PC. This has brought EC to become one of the first choices for LIB solvents, although it also has some flaws, namely its smaller working temperature range compared to PC.

### Vinylene Carbonate (VC)

In order to further improve the SEI formation process, VC has been proposed as an additive able to suppress gas evolution [80] and improve performances of PC based electrolytes.

The improved performances are related to the inhibition of solvent reduction and thus the formation of a thinner and more stable SEI derived mostly from the reduction of the additive [80]–[82].

## 1.4 Aim of this work

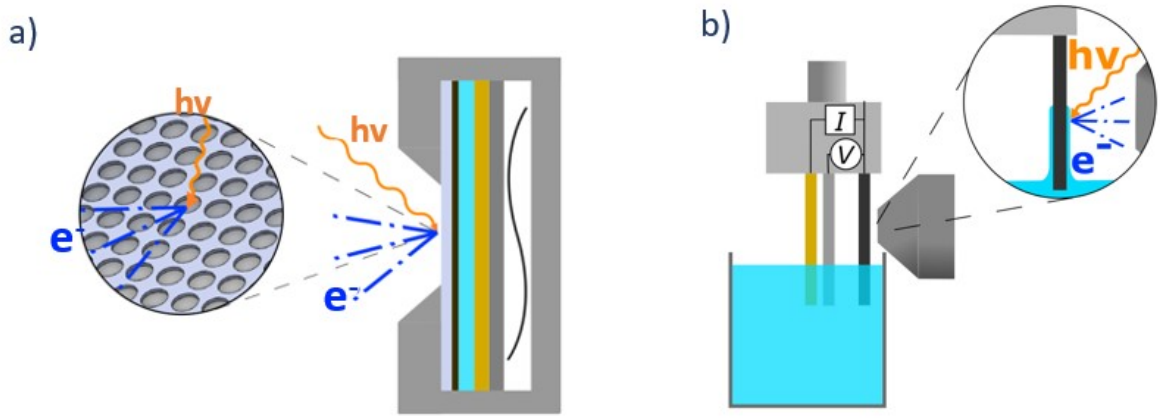


Figure 1.6: Schematic of the a)*in situ* cell for *operando* HAXPES and the b)Dip & Pull NAP-PES setup

After describing the SEI with its heterogeneous and metastable nature, it should be clear how an *in situ* approach, linked to techniques with a strong chemical sensitivity, could be crucial to answer to some of the many questions still open on the SEI formation and its relation to electrochemical properties.

During my PhD, I have addressed this challenge through the development of techniques for *in situ* studies of the SEI formation based on X-ray Photoelectron Spectroscopy (XPS), using two techniques available on Synchrotron lightsources, namely Hard X-ray Photoelectron Spectroscopy (HAXPES) and Dip & Pull Near Ambient Pressure Photoelectron Spectroscopy (NAP-PES), both providing a complementary observation of the SEI. The experiments were performed at two different beamlines in two different synchrotrons, GALAXIES at SOLEIL and HIPPIE at MAX-IV.

The HAXPES unique capability to probe up to tens of nanometers in depth permits to

access the solid-liquid interface from the solid side through a thin membrane, and probe the formed SEI (Figure 1.6, left side). For this purpose, we have developed an electrochemical cell tailored for the HAXPES end-station of the GALAXIES beamline. In this cell, a $Si_3N_4$ membrane separates the liquid electrolyte from the UHV, while a voltage is applied between the two electrodes, thus enabling *operando* HAXPES measurements on the SEI.

On the other hand, NAP-PES offers the possibility to have liquid electrolytes in the analysis chamber. The electrochemical set-up available on the HIPPIE beamline allows studies of the SEI through the liquid electrolyte: a thin electrolyte meniscus is created on the surface of the electrode using the Dip & Pull setup (Figure 1.6, right side). It is thus possible to perform *in situ* XPS on the SEI, when the appropriate combination of substrate and liquid electrolyte is chosen.

In the first chapter, an overview of the Li-ion battery and a focus on the solid-electrolyte interphase has been provided, along with the open issues associated to the SEI formation and stability. Then the European BIG-MAP project was briefly introduced, together with the list of studied materials.

The second chapter of this thesis will be focused on introducing the applied techniques and the developed approaches, giving a description on the experimental methods. At first, a brief introduction to X-ray Photoemission Spectroscopy will be given, with a focus on the synchrotron-based XPS techniques. After that, the beamlines and the setup experiment will be presented.

In the third chapter, the results on the *operando* NAP-PES studies will be presented. In particular, three different electrolyte formulation were chosen to understand their influence on the SEI formation, namely PC ($C_4H_6O_3$), PC + VC ($C_3H_2O_3$) and PC + EC $(CH_2O)_2CO$

In the fourth chapter, the specially designed *in situ* cell for HAXPES experiment will be shown. This cell was developed to overcome the experimental constraints of HAXPES

along with good electrochemical properties. In particular, different membranes were tested, to maximize the photoelectrons collection. Despite some issues related to the membrane robustness and electrochemical performances, our preliminary tests were promising, and further improvements could finally lead to a hands-on HAXPES electrochemical cell.

In the fifth chapter, the conclusion of this work along with the future perspective will be discussed.

# Chapter 2

# Experimental method

In this chapter, an introduction to X-ray photoelectron spectroscopy (XPS) technique is given, describing the basic principles and experimental setup. Then, I will show the two main approaches developed to study the SEI formation in operando conditions, namely the HAXPES and the NAP-PES. Finally, I will present the procedure applied to the data analysis.

## 2.1 Theory of X-ray Photoelectron Spectroscopy

X-ray Photoelectron Spectroscopy (XPS) originates from the explanation of the photoelectric effect provided by Albert Einstein in 1905 [83]. In the following years, the comprehension of the effect improved and from the late 1950s the technique started to become a powerful tool to study the composition and electronic structure of matter. This leads to the the Nobel prize of physics awarded to Kai Siegbahn in 1981 for the development of high resolution XPS [84].

To understand the principles of XPS, it is important to introduce the following equation, describing the fundamental energy conservation in photoemission process:

$$\begin{aligned} h\nu &= E_{binding}^{vacuum} + E'_{kinetic} + V_{charge} + V_{bias} \\ h\nu &= E_{binding}^{Fermi} + \varphi_{spectrometer} + E_{kinetic} + V_{charge} + V_{bias} \end{aligned} \tag{2.1}$$

Here, $h$ is Planck's constant, $\nu$ is the photon frequency, $E_{binding}^{vacuum}$ is the binding energy

of a given electron relatively to the vacuum level of the sample, $E'_{kinetic}$ is the kinetic energy of the emitted photoelectron just as it leaves the sample, $E_{kinetic}$ the kinetic energy as measured when reaching the spectrometer, $E^{Fermi}_{binding}$ indicates the binding energy relative to the Fermi level, $V_{charge}$ is for a charging potential that could build up in case of an absence of a compensation of current, while $V_{bias}$ stands for any ulterior bias potential that could be found between the sample and the analyser. Finally, $\phi_{spectrometer}$ is the work function of the spectrometer used to measure the kinetic energy. Through this relation, knowing the kinetic energy of a measured electron and the work function of the spectrometer allows to also calculate the binding energy of core or valence electrons. It is then possible to obtain precise information on the elements, the electronic structure and chemical state of species near to the sample surface, as per the following slimmer equation:

$$E_{binding} = h\nu - E_{kinetic} - \Phi_{spectrometer} \tag{2.2}$$

A scheme of the XPS experimental setup is shown in figure 2.1: the main components are a photon source and an electron analyser with the typical hemispherical shape.

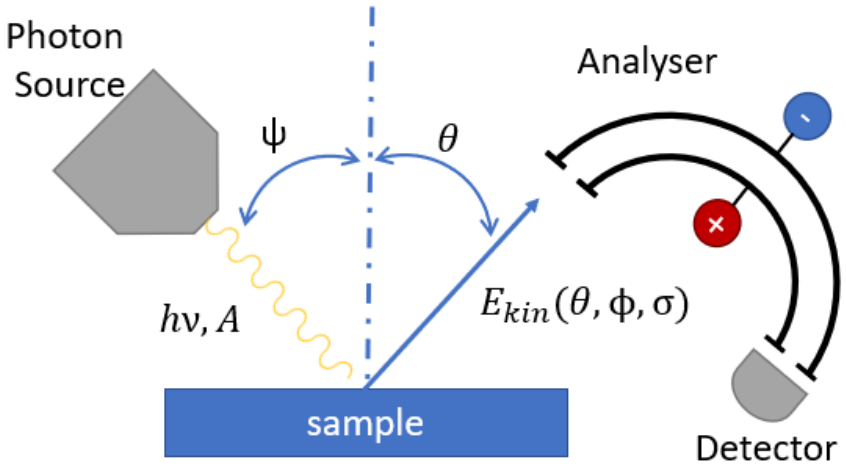


Figure 2.1: Scheme of an XPS experiment.

The photons hit the sample with an incidence angle of $\theta$ and photoelectrons are emitted and collected by the analyser. In the hemispherical part, a slit and an electrostatic field

allow to select the different kinetic energies of the electrons. While its true that the process involving the excitation of a photoelectron is quite complex, it can be simplified enough for our needs as it is shown in Figure 2.2 [85].

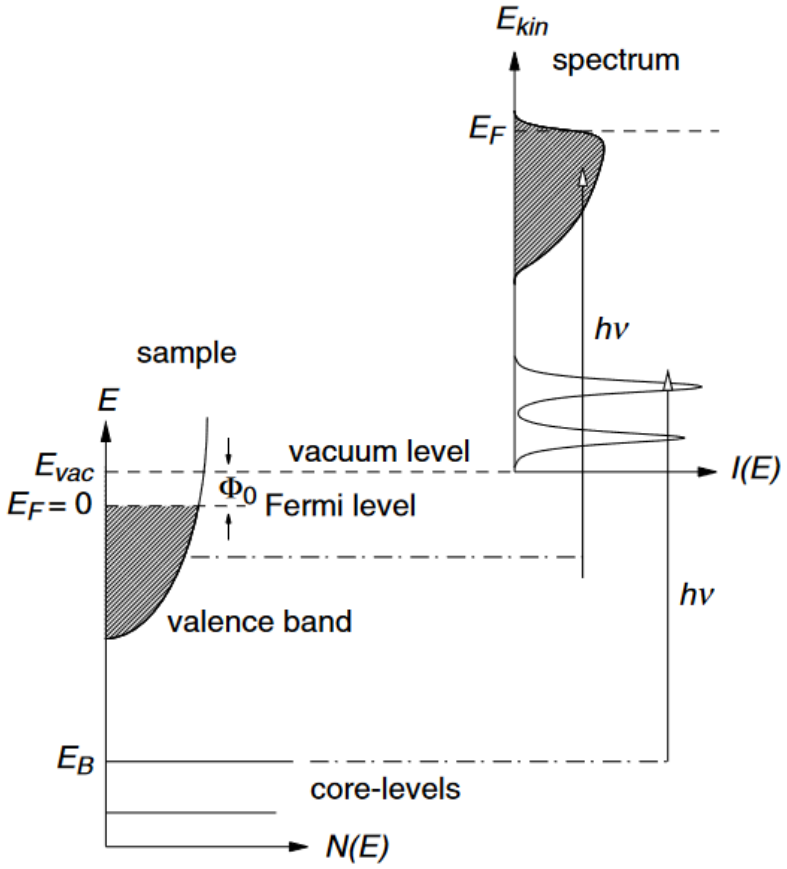


Figure 2.2: Different energy levels involved in the XPS process [85].

Here we can see how from the core levels at energy $E_B$, an electron is excited by a photon of energy $h\nu$ over the vacuum level. While it is trute that in a sample we always deal with a many-body system, when the electronic correlation effect is small enough, it is possible to approximate the process to a single-particle problem. The photoelectric process can then be described using the Fermi's golden rule that results from a first order application of perturbation theory. We will have a photocurrent $J$ as a result of a photon-induced excitation of a system with initial state $|\Psi_i\rangle$ and a final state $|\Psi_f\rangle = |\Psi_{k,f}\rangle$ , that results in a photoelectron with momentum $\mathbf{k}$ and kinetic energy $E_{kin}$, plus the remaining system with now $(N-1)$ electrons. The equation is then written as follows:

$$J_\kappa(\nu) = \frac{2\pi}{\hbar} \sum_s |\langle \Psi_{\kappa,s}|H_{PE}|\Psi_i\rangle|^2 \, \partial(\epsilon_\kappa - \epsilon_s - \nu) \tag{2.3}$$

Where $s$ is an index that spans over the set of quantum numbers containing all possible excitations of the final state. Then, the $H_{PE} operator describes the interaction of an electron system with an electr$ = -i$\hbar\nabla$ transformed to $p \to p - \frac{e}{c}A$ in the unperturbed Hamiltonian $E_0 = \frac{p^2}{(2m_e)} + eV(r)$. With this, $H_{PE}$ can be expressed as follows:

$$\begin{aligned} H &= \frac{1}{2m_e}\left[\mathbf{p} - \frac{e}{c}\mathbf{A}\right]^2 + eV(r) \\ &= \frac{p^2}{2m_e} + \frac{e}{2m_e c}(\mathbf{A}\cdot\mathbf{p} + \mathbf{p}\cdot\mathbf{A}) + \frac{e^2}{2m_e c^2}A^2 + eV(r) \\ H &= H_0 + H_{PE} \end{aligned} \tag{2.4}$$

Where $H_{PE}$ is then

$$H_{PE} = \frac{e}{2m_e c}(\mathbf{A}\cdot\mathbf{p} + \mathbf{p}\cdot\mathbf{A}) + \frac{e^2}{2m_e c^2}A^2 \tag{2.5}$$

Since $\mathbf{A}$ becomes relevant only for high photon intensities, the quadratic term can be neglected. Then, since $[\mathbf{p}, \mathbf{A}] = -i\hbar \xrightarrow{\nabla} \cdot\mathbf{A}$, and considering that using the Coulomb gauge $\xrightarrow{\nabla} \cdot\mathbf{A} = 0$, we can then rewrite Equation 2.5 as

$$H_{PE}^{vol} = \frac{e}{2m_e c}[-\mathbf{A}\cdot\mathbf{p}] \tag{2.6}$$

In order then to be able to calculate a spectrum, a final important approximation need to be made: the so-called *sudden approximation*. In this approximation, the final state of the system, namely $|\Psi_{k,s}\rangle$ and the photoemitted electron are decoupled, so that any interaction between the two can be neglected. With this approximation the final state can be written as

$$|\Psi_{k,s}\rangle = |\kappa; N-1, s\rangle \to c_\kappa^\dagger |N-1, s\rangle \tag{2.7}$$

Where the $c_\kappa^\dagger$ is the creation operator for the photoelectron. The Fermi's golden rule equation then becomes:

$$J_\kappa(h\nu) = \frac{2\pi}{\hbar} \sum_k |\Delta_{\kappa k}|^2 \, A_k^<(\epsilon_\kappa - h\nu) \tag{2.8}$$

With $A_k^< = \sum_s |\langle N-1, s|c_k|N\rangle|^2 \frac{\partial}{\partial(h\nu - \epsilon_s)}$ representing the one-electron spectral function, and $\Delta_{\kappa k} = \langle \Psi_\kappa | H_{PE} | \Psi_k \rangle$ the photoemission matrix element, giving the probability of the transition of an electron from a state $|\Psi_k\rangle$ to a state $|\Psi_\kappa\rangle$. While the sudden approximation is especially well-suited to describe high kinetic energy electrons in finite systems, it does not work as well for solids, where extrinsic losses must also be considered. This was implemented by Berglund and Spicer [86] with their three-step model, where the whole process from the absorption of the photon to the emission of the electron from the solid bulk is described separately by three different steps as shown in Figure 2.3 [87]:

1. The electron is excited from the initial energy level to the final virtual orbital stage. This is what was calculated before and is referred to as "intrinsic processes".

2. The transfer of the photoelectron to the surface. The processes here are called extrinsic processes and take into account the scattering processes that electrons undergo in the bulk.

3. The escape of the electron from the surface to the vacuum.

The three-step model provides a good approximation of the photoemission process for bulk systems and can also take into consideration secondary electron emission processes that can result in the emission of an electron, such as plasmons, or shake-up/shake-off processes involving valence electrons. We will now go further into the details of the second step, regarding the emission of the photoelectron.

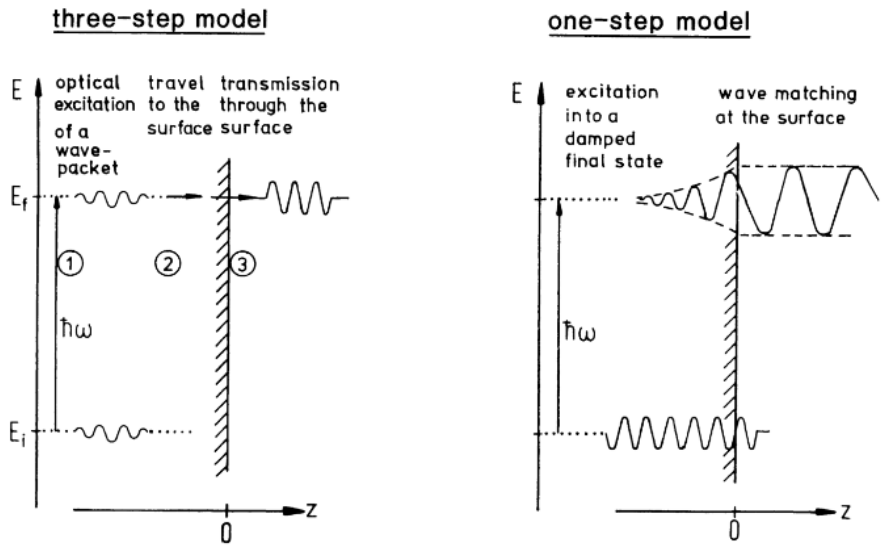


Figure 2.3: Illustration of the three-step and one step models for XPS [87]

It can be understood how the interaction the electron undergoes when traveling from the emitting atom to the bulk plays a central role in the XPS process. Due to their high interaction rate, electrons have a very strong probability of undergoing inelastic scattering processes with other atoms when they are photoemitted. This means that it becomes difficult to measure the exact emission kinetic energy of them and thus obtain clear information unless they reach the analyzer without losing energy due to prior scattering processes.

This brings forth two different aspects of XPS: Firstly, to minimize the photoelectrons' interaction, XPS chambers need an Ultra High Vacuum (UHV) environment, both to avoid scattering processes of the electrons with the air molecules and to prevent surface contamination. The latter is also related to the second aspect of XPS, the surface sensitivity. The low escape depth of electrons means that XPS cannot probe more than the first nanometers of the sample, and it also implies that if a layer of deposition products from the atmosphere (moisture, dust, $CO_2$) would form on the sample, the measurement would be strongly affected.

Now, neglecting inelastic scattering, it is possible to express the intensity of an electron flux from a material (and thus the amount of electrons that reach the surface without

suffering energy loss) with the Beer-Lambert law as:

$$I = I_0 \cdot e^{-\frac{d}{\lambda \cos \alpha}} \tag{2.9}$$

With $I_0$ indicating the initial flux originating at depth $d$, and $\alpha$ as the angle formed between the normal to the surface and the analyzer direction. Then $\lambda \cos \alpha$ stands for the mean escape depth (MED) and indicates the possibility for an electron to pass through a medium without undergoing inelastic scattering processes. MED can then be defined as

$$\Delta = \lambda \cos \alpha \tag{2.10}$$

This value gives then an indication of the average depth normal to the surface from which the electrons can escape, where $\lambda$ indicates the inelastic mean free path (IMFP), and $\alpha$ is the emission angle. The values for $\lambda$ have been measured and calculated for several materials [88], and the results [89] were fitted with a modified version of the Bethe equation for inelastic electron scattering in matter that goes as the following:

$$\lambda = \frac{E_{\text{kin}}}{E_{\text{p}}^2 \left[\beta \ln(\gamma E_{\text{kin}}) - \frac{C}{E_{\text{kin}}} + \frac{D}{E_{\text{kin}}^2}\right]} \tag{2.11}$$

Where $E_{\text{kin}}$ indicates the energy of the photoemitted electrons, $E_{\text{p}}$ stands for the free electron plasmon energy and is expressed as $E_{\text{p}} = 28.8(\frac{N_v \rho}{M})^{1/2}$, with $\rho$ as the density of the material, $N_v$ the number of valence electrons per atom (or molecule), and $M$ is the atomic or molecular weight. Then, $\beta, \gamma, C, D$ indicate adjustable fit parameters. From these calculations, the curve shown in Figure 2.4 was calculated theoretically for different materials. It shows that the IMFP strongly depends on the energy, increasing with the increased electron energy.

From this, it can be calculated that of the total electron flux that is escaping from the bulk, 63% of it is coming from the first $d = 1 \cdot \lambda \cos \alpha$ while the value goes to 93% for $d = 3 \cdot \lambda \cos \alpha$, meaning that the information depth of a photoemission experiment is usually said to be three times the ME [90].

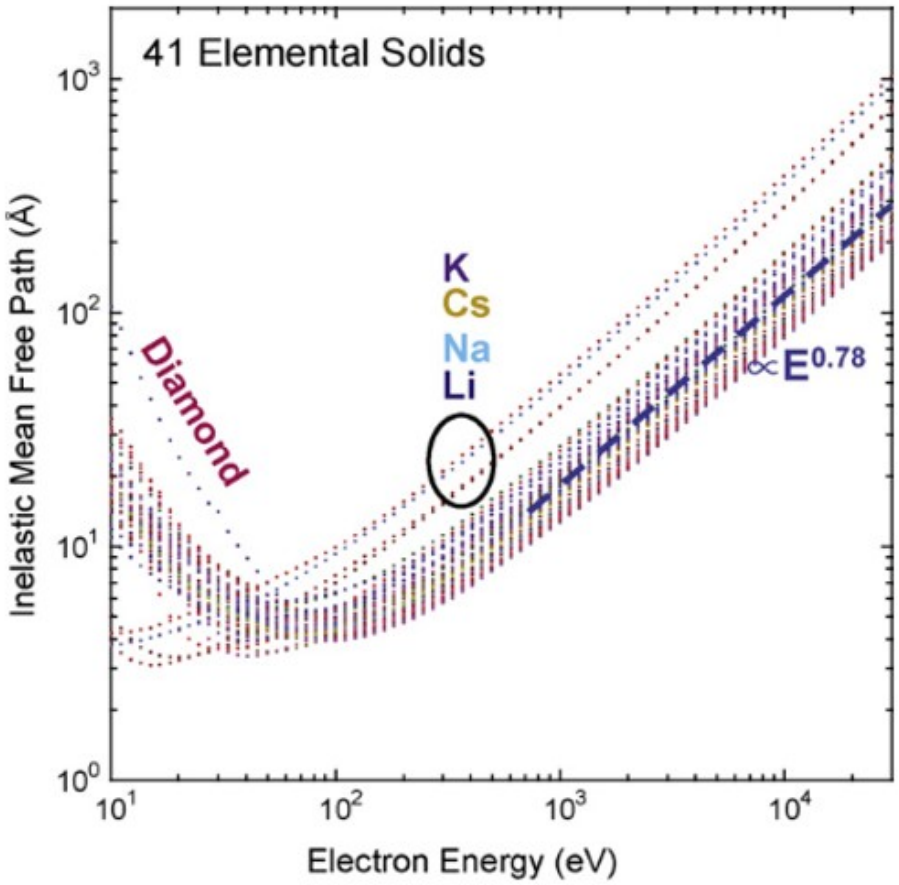


Figure 2.4: Universal curve for IMFP [90]

### 2.1.1 Core-level analysis

Chemical and electronic information are provided by the analysis of XPS spectrum of the core levels. They are related to the photoexcitation of an electron coming from the inner shells of an atom. Core level electrons have very specific binding energies related to their electronic shell, their spin, and the atomic mass of the excited atom. Thus, a first analysis of core level binding energies allows identifying all the different elements present in a given sample.

Moreover, in the case of high-resolved measurements, core level analysis shows further useful characteristics. In fact, electrons coming from the same element and core level may slightly differ in binding energy based on other important details: the chemical environment or spin-orbit splitting give rise to shifts in the binding energy, yielding information

on the presence of differently bonded atoms on the sample surface. Therefore, it is possible to characterize the chemical environment of specific atoms or their charge distribution or oxidation state.

The reliability of a photoemission spectrum is determined by two main parameters: resolution and intensity of the peaks. If we describe the peaks using a Voigt function, then the resolution can be calculated as:

$$\Delta E^2 = \Delta E^2_{\text{peak}} + \Delta E^2_{\text{instrum}} = \Delta E^2_{\text{peak}} + \Delta E^2_{X-rays} + \Delta E^2_{\text{ana}} \tag{2.12}$$

Where $\Delta E_{\text{peak}}$ is the natural width of the peak, usually described by a Lorentzian function, and $\Delta E_{\text{instrum}}$ is related to the instrumental resolution and is described by a Gaussian. This is represented by the line width of the incident X-rays and the energy resolution of the analyzer itself.

Then, it is possible to express the intensity of the peak $P_i$ as:

$$P_i = c\sigma_i\phi\lambda T n_i \tag{2.13}$$

Where $c$ is a proportionality factor, $\sigma_i$ stands for the cross-section of the photoemission, $\phi$ is the angular distribution factor, $\lambda$ the inelastic mean free path (IMFP), $T$ the analyzer transmission efficiency, and $n$ the number of emitting atoms in the considered volume.

There are also other phenomena contributing to an XPS spectrum, aside from the main peaks coming from photoelectrons that avoided inelastic scattering. These phenomena are actually the majority of intensity recorded in a spectrum and are all the electrons that suffered intrinsic and extrinsic energy losses, forming the secondary structure, made of the background and the satellite peaks. The intrinsic energy losses are related to any additional excitation accompanying the photoexcitation, thus reducing the initial energy of the photoelectron.

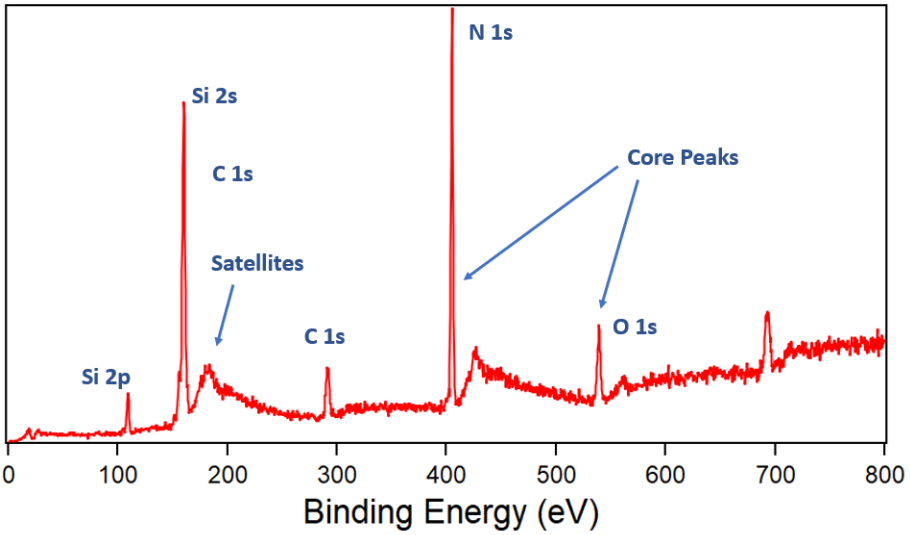


Figure 2.5: Survey spectra on $Si_3N_4$ chip collected at GALAXIES with $h\nu$ = 7 keV

This can be caused by the sudden changes in electric fields made by the core-hole created by the photoemission, that then perturbs the valence electrons. These processes are, for example, the shake-up and shake-off features, that give the so-called satellite peaks. In these cases, electrons from the valence band are either promoted to an unfilled band of higher energy or directly promoted to the vacuum level. Shake-up satellites will be observed at higher binding energy than the parent peak, while the shake-off ones falls in the broad inelastic tail of the peak and would not be observed.

The extrinsic losses are instead any kind of loss due to the passage of photoelectrons from the atom to the surface and are caused by the interaction of the electron with other electrons; they are evenly distributed and are the main component of the continuous background of the low kinetic energy of the spectrum. In Figure 2.5, a survey spectrum showing some of the features here described can be seen.

### 2.1.2 Calculation of the binding energy

A way to compute the energy of the emitted core-level photoelectron is to take the difference between the ground state energy of the system and the energy of the system with a core-hole in the final state. For an N-electron system, then

$$\xi = E_{\text{fin}}^{\text{exact}}(N-1) - E_{\text{in}}^{\text{exact}}(N) \tag{2.14}$$

Where $E_{\text{in}}$ and $E_{\text{fin}}$ are the total energies of the system before and after the ionization that can be computed through the application of the Hartree-Fock (HF) method to the Schrödinger equation. In this method, each electron is treated as if it were decoupled from the motion of the other electrons, so that the system can be solved as a set of independent single particles; in order to account for the electron-electron interaction, however, some approximations have to be added: the kinetic energy, the Coulomb potential, and the exchange terms for each particle are calculated as if the rest of the electrons form an effective electric field in the system. However, the energies calculated with HF do not exactly match the total energy of the system, since the electron-electron interaction is not considered. The HF energy can then be "corrected" with the addition of a term $E^{\text{c}}$ so that:

$$E^{\text{exact}} = E^{\text{HF}} + E^{\text{c}} \tag{2.15}$$

And then the energy of the core-level electron becomes:

$$\xi = E_{\text{fin}}^{\text{exact}}(N-1) - E_{\text{in}}^{\text{exact}}(N) + \Delta E^{\text{c}} \tag{2.16}$$

This may be a good approximation, but it must be noted that the energies obtained from the HF method are not actually representative of the properties of the system. Indeed, using the HF method we are also assuming that when the electron gets removed, the other electrons remain unchanged, as for Koopman's theorem, also called the frozen orbitals approximation. We then also have to consider the relaxation term $E^{\text{R}}$, giving:

$$\xi = E_{\text{fin}}^{\text{exact}}(N-1) - E_{\text{in}}^{\text{exact}}(N) + \Delta E^{\text{c}} + E^{\text{R}} \tag{2.17}$$

So that to have a final value of the binding energy of the photoemitted electron, we can define the difference between initial and final state energies as the initial-state contribution $-\Delta\varepsilon_i$ and considering that the binding energy is taken for solid materials referencing it to the Fermi level of the sample $E_{\mathrm{F}}$:

$$E_{\mathrm{b}}(i) = -\Delta\varepsilon_i + \Delta E^{\mathrm{c}} + E^{\mathrm{R}}(i) + E_{\mathrm{F}} \tag{2.18}$$

Thus obtaining a theoretical value of the binding energy for a given electron [91].

## 2.2 Instrumentation

In this section, we will briefly describe the main instrumentation used during the project, from the X-ray synchrotron radiation to the experimental setup available for the HAXPES and NAP-PES studies, performed at the GALAXIES (SOLEIL, France) and HIPPIE (MAX IV, Sweden) beamlines.

### 2.2.1 Synchrotron radiation

While the sources for X-ray light can be manifold (from X-ray tubes to ultra-fast lasers with a harmonic generation system or free electron lasers), this work focuses on X-ray synchrotron radiation. In fact, while X-ray tubes are the most convenient choice for laboratory XPS experiments, being relatively cheap, easily accessible, and yet reliable, synchrotron sources offer a higher quality X-rays, with an extremely high flux, narrow line width, tunable energy and polarized light. An outline of a typical synchrotron can be seen in Figure 2.6.

A synchrotron produces photons in a very wide energy range (from the far-infrared to hard X-ray) thanks to a basic principle derived from the Maxwell equations: when accelerated, charged particles (in this case, electrons) emits electromagnetic waves.

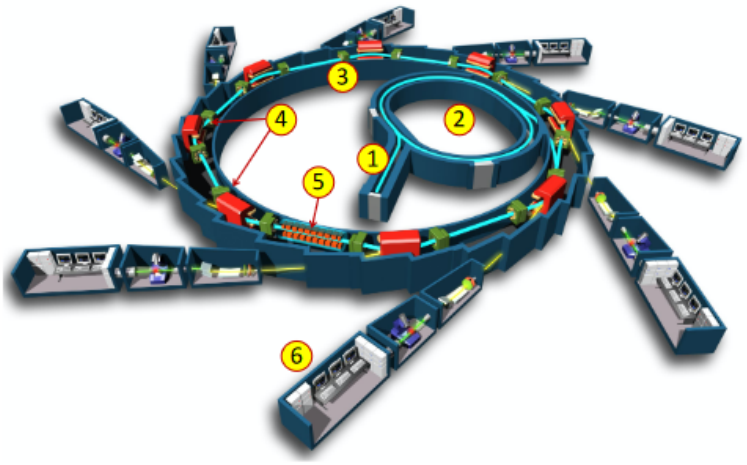


Figure 2.6: Schematic picture of a synchrotron with (1) linac, (2) booster, (3) storage ring, (4) and (5) are bending magnets and focusing undulators and (6) beamlines.

The process starts with electrons emitted by an electron gun and accelerated in a linear accelerator (LINAC) up to an initial energy of 100 MeV. The electrons are grouped into bunches and then transmitted to the booster, a circular accelerator that further increases their energy up to the GeV range (2.75 GeV for SOLEIL) prior to the injection into the storage ring. There, the electrons circulate for days in the storage ring, where magnetic devices control their trajectory. These devices are dipoles (bending magnets) or undulators or wigglers (a succession of alternating magnets that make electrons oscillate); the change in linear trajectory given by these devices produces the needed electromagnetic radiation. The light passes then through the different optical elements available on each beamline and the photons are focused, and their energy selected depending on each of the different needs.

A synchrotron radiation source offers many advantages compared to laboratory sources. The brilliance (photons $\cdot$ s$^{-1}$ $\cdot$ mrad$^{-2}$ $\cdot$ mm$^{-2}$ per $0.1\%$ radiation bandwidth) represents both the brightness and angular spread of the beam [92]. A higher brilliance means a higher density of photons of a given wavelength and direction for a unit of time, and the brilliance available at synchrotrons is higher than any laboratory source, from an order of magnitude of $10^7$ up to $10^{20}$ for third-generation synchrotrons [93]. Synchrotron radiation also

allows having highly focused X-rays and tunable polarization of the radiation, thus highly expanding the possible applications. The experiments reported in this thesis were carried out at two beamlines:

- The HAXPES experiments were carried out at the tender/hard X-rays GALAXIES beamline, **SOLEIL** (France, 2.75 GeV).

- The NAP-PES experiments were carried out at the soft X-rays branch of the HIPPIE beamline, **MAX-IV** (Sweden, 3 GeV).

### 2.2.2 Vacuum environment

As already mentioned, XPS experiments usually need ultra-high vacuum to be performed. This is due to both the need to avoid electron scattering through the gas and minimize surface contamination. While a pressure of around $10^{-6}$ mbar is enough to avoid scattering processes, with this pressure, there is still a strong effect of deposition of gas species on the sample surface [94]. For this reason, XPS systems tend to operate at lower ranges (below $10^{-8}$ mbar). Nowadays, UHV systems consist of a combination of different solutions that are applied depending on the desired pressure. These include turbomolecular pumps or ion pumps, all combined with several gauges and valves to control the system. When higher vacuum needs to be achieved, Ti sublimation pumps, getter pumps, and cryogenic pumps are also employed. Moreover, an occasional "bakeout" on the whole system is needed to remove adsorbed molecules from the walls of the chambers. During a bakeout, the whole instrument is brought to around 100 - 200°C for a few days, using heating cables. The high temperature causes a further release of adsorbed gases and moisture from the inner parts of the measurement chamber.

### 2.2.3 Analyser

To perform spectroscopic measurements of photoelectrons, an analyzer is needed. An electron analyzer in modern XPS satisfies two main criteria: high energy resolution and high collection efficiency, to maximize the final resolution and intensity of the spectrum. The most used analyzer in modern XPS systems, satisfying both requirements, is the hemispherical sector analyzer (HSA).

The structure of a typical HSA is shown in Figure 2.7. Two concentric hemispheres of radius $R_1$ and $R_2$ form the hemispheric part, the entrance slit collects and focuses electrons, that also adjust the kinetic energy of the electrons to match the so-called pass energy ($E_p$) of the analyzer. Then a potential difference is applied across the two hemispheres so that the inner one is electrically grounded and a negative bias is applied to the outer one. This means that the electrons will disperse according to their kinetic energy, and only a selected portion can exit from the exit slit of the HSA to reach the detector. By scanning the different potentials, a spectrum can be collected. Then the relation between pass energy and applied potential can be calculated by:

$$e\Delta V = E_p \cdot \left( \frac{R_2}{R_1} - \frac{R_1}{R_2} \right) \tag{2.19}$$

Where $\Delta V$ is the potential difference between the two hemispheres. The energy resolution is then:

$$\Delta E_{\text{ana}} = E_p \cdot \left( \frac{\omega}{2R} - \frac{\alpha^2}{2} \right) \tag{2.20}$$

showing that it mainly depends on the entrance slit width $\omega$, the mean radius $R$, the pass energy $E_p$, and the acceptance angle $\alpha$. It is clear how the resolution for a fixed analyzer can be tuned by choosing the pass energy [95]. Low pass energy will give better resolution because higher ones mix spatial and energy information on the electrons, resulting in a

less resolved spectrum. However, greater resolution also implies a lower count rate and a worse signal-to-noise ratio. Resolution can also be improved by reducing the width of the entrance slit of the HSA or having an analyzer with a larger radius. Larger sizes come, however, with higher requirements for vacuum and mechanical stability [96].

Once the electrons pass by the exit slit of the analyzer, they are counted by a detector. Modern systems use 2D detectors based on micro-channel plates combined with a read-out method that can be a CCD camera or a delay-line detector.

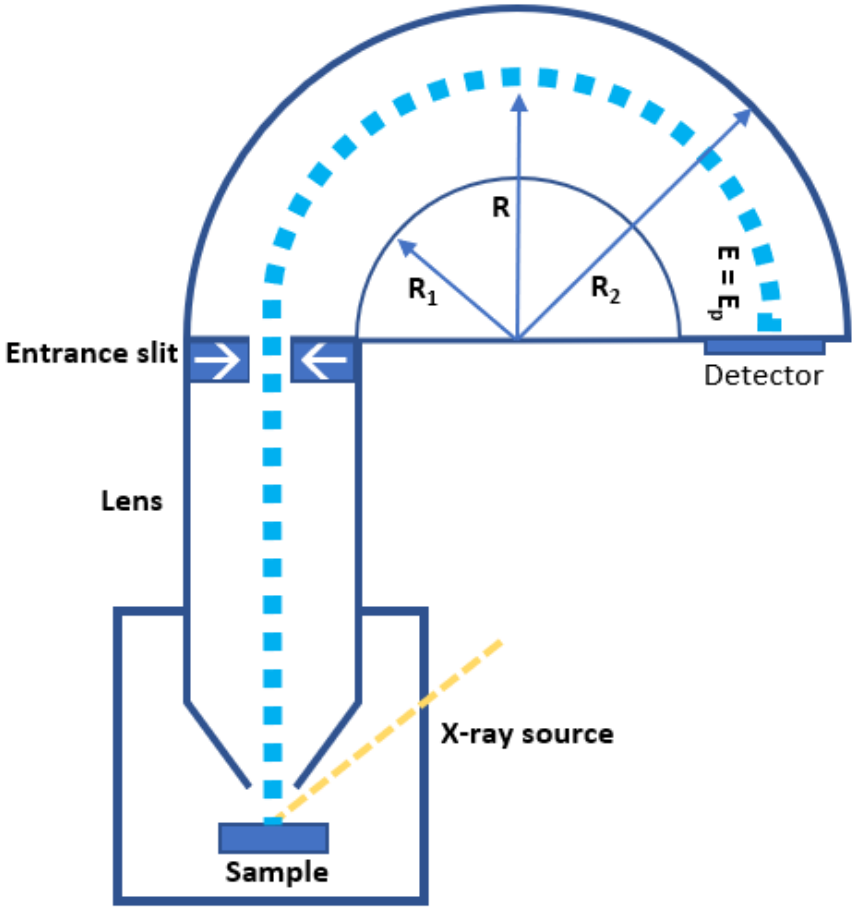


Figure 2.7: Scheme of a hemispherical photoelectrons analyser.

## 2.3 HAXPES end-station at GALAXIES

Hard X-ray Photoelectron Spectroscopy (HAXPES) is a method of growing importance for the investigation of materials [97], coupling the sensitivity of XPS to the local chemistry with the possibility to access to the bulk. This is thanks to the extended range of photon energy obtainable in a synchrotron, that significantly improves the probing depth of XPS, as seen before when discussing the IMFP.

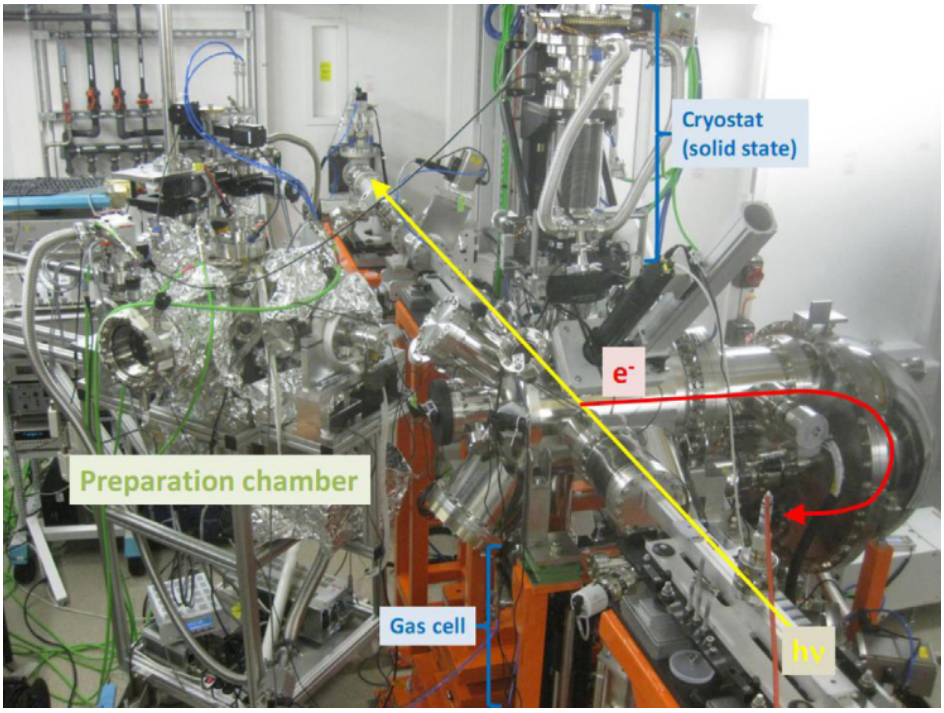


Figure 2.8: HAXPES end-station at GALAXIES beamline, SOLEIL.

The GALAXIES beamline, located at SOLEIL synchrotron, offers an HAXPES end-station dedicated to these experiments. The X-ray photons are produced by an in-vacuum U20 undulator installed in the storage ring of the synchrotron. The beamline has an optimized flux between 2.3-12 keV with a photon energy bandwidth between 100 meV and 1 eV. The X-ray energy is then selected through a double crystal cryogenically cooled Si(111) monochromator (DCM) after which there's a 4-bounce high-resolution monochromator (HRM) equipped with Si(110) symmetric and asymmetric crystals. It is also possible to obtain high-energy

resolution ($\Delta E \approx 150$ meV FWHM) using higher-order reflections of the Si(111) monochromator above 6.9 keV for Si (333). Downstream of the DCM and HRM, a first mirror is used to reject high-energy harmonics and then to collimate the beam on a second, toroidal mirror that focuses it at the sample position on a spot size of $30 \times 80\ \mu m^2$.

The HAXPES end-station (Figure 2.8) is equipped with an EW4000 SCIENTA hemispherical electron analyzer that is mounted in the analysis chamber at 90° with respect to the incident photon energy. The analyzer is equipped with an extra-wide lens that allows a collecting angle of up to 60°, which helps to increase the counts also considering the low photo-ionization cross-section at high kinetic energies. It is possible to perform measurements from $10^{-5}$ up to $10^{-9}$ mbar [98].

## 2.4 NAP-PES end-station at HIPPIE

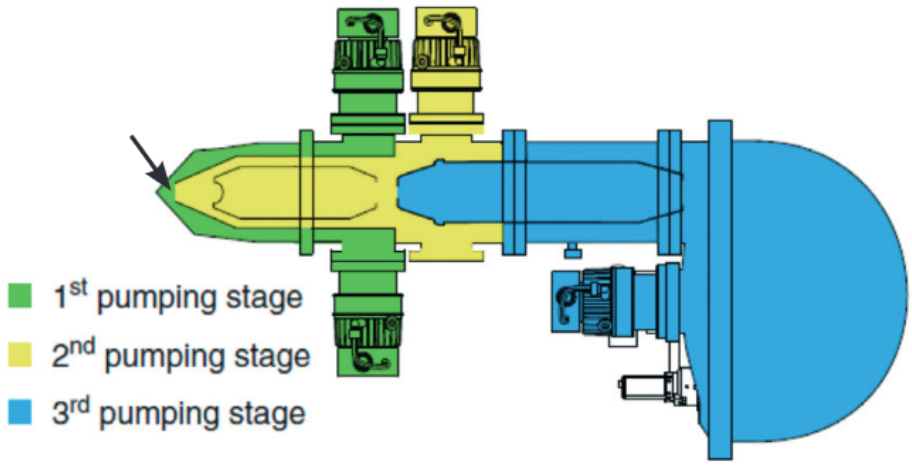


Figure 2.9: Scheme of the differential pumping of a HiPP-3 analyser.

Near Ambient Pressure Photoemission Spectroscopy (NAP-PES) experiments have been conducted at the HIPPIE beamline of MAX-IV synchrotron. HIPPIE is a soft X-ray beamline dedicated to in situ and operando X-ray photoelectron spectroscopy experiments, allowing control of the gaseous atmosphere with pressures up to 30 mbar. The photon energy range goes from 250 to 2200 eV with planar polarization. There are two end-stations, one for catalysis and the other for electrochemical liquid systems, where our studies were done.

This end-station is designed for studies at the solid-liquid or liquid-gas interface, allowing full electrochemical control of the system. The X-ray source is an EPU53 undulator, followed by a collimating mirror with gold coating and then a plane grating monochromator. A toroidal mirror then collimates vertically the light over a monochromator, and then a cylindrical mirror; finally, the beam is refocused by a single toroidal mirror. The beam size is 25 $\times$ 60 $\mu m^2$ [99]. The analyzer is a Scienta HiPP-3 analyzer compatible with high-pressure measurements, up to 30 mbar [100], thanks to its differential pumping design, which allows having UHV in the hemispherical analyzer without being connected to higher pressure systems, as shown in Figure 2.9.

### 2.4.1 Dip & Pull method

The electrochemical cell is dedicated to *operando* measurements and is equipped with an analysis chamber connected to an external glovebox to allow sample manipulation under an inert atmosphere. In the chamber, a system with two motors allows controlling the position of the sample: the top one, with four axes (XYZ and rotation), has a three-electrode configuration and is expected to mount the electrodes. On the bottom one, with three axes, it is instead possible to put a container filled with a liquid of choice (an electrolyte in the case of electrochemical experiments). This system is designed to carry out Dip & Pull experiments, as shown in Figure 2.10.

In this kind of experiment, meant to study the solid-liquid interface in operando conditions, the solid electrode is dipped inside the liquid electrolyte during the electrochemical procedures, to be then slightly taken out. XPS measurements were carried out through the thin meniscus that forms on the electrode surface. Using this approach, it is possible to measure the liquid electrochemical system by XPS without interrupting the contact between solid and liquid phases. In Figure 2.11 a picture taken on HIPPIE shows the Dip & Pull setup used.

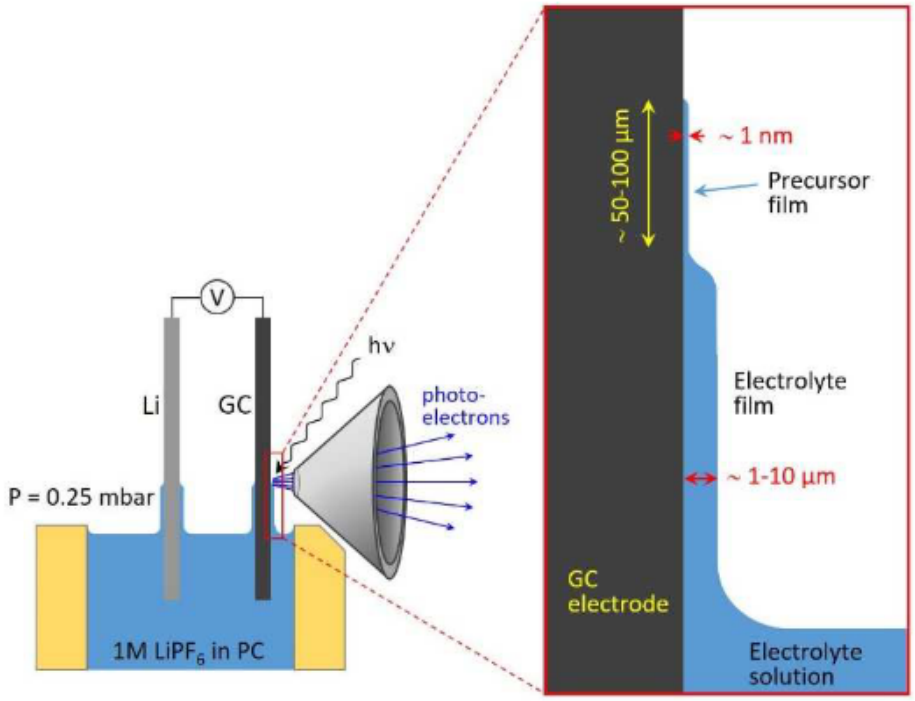


Figure 2.10: Schema of a Dip & Pull NAP-PES experiment [101].

## 2.5 General procedure for XPS data analysis

In this paragraph, we describe the data analysis procedure applied on the XPS spectra and our choice related to the definition of the binding energy in the case of applied potential. Peak fitting is commonly used to extract meaningful information from XPS spectra such as the peak position, FWHM, integrated area, and line shape. This set of parameters will define a peak. A typical XPS core peak spectra is done by the sum of one or more peaks and finally a background function. The choice of the background function depends on several parameters, and is needed to subtract the contribute of photoelectrons coming from inelastic scattering processes from the peak. A proper XPS peak fitting is also heavily dependent on the type of background used. The easiest approach is a linear background and can be used for low energy peaks. A more sophisticated approach is to use the Shirley background: in this case, the assumption is that the background comes only from inelastic scattering processes of the high kinetic energy photoelectrons, and is then proportional to the intensity of the peak measured at that given kinetic energy. This background works

well when the selected energy range includes only the main core peaks. When trying to fit higher energy range, Tougaard model appears more appropriate: originally developed for transition metals, this model includes the energy loss function and provides a better background in higher energy range, while showing difficulties when there are numerous overlaps between peaks.

Once a starting set of curves and a background are chosen, the fit is mathematically done through a process of minimization of the figure of merit. It is thus highly dependent on the initial guesses made on the data to generate the fit components, and very often, choices that give a perfect fit are not necessarily good, since they are deprived of physical or chemical sense. A good choice of starting parameters derives from a good physical and chemical knowledge of the sample, that is always needed to obtain a reliable fit.

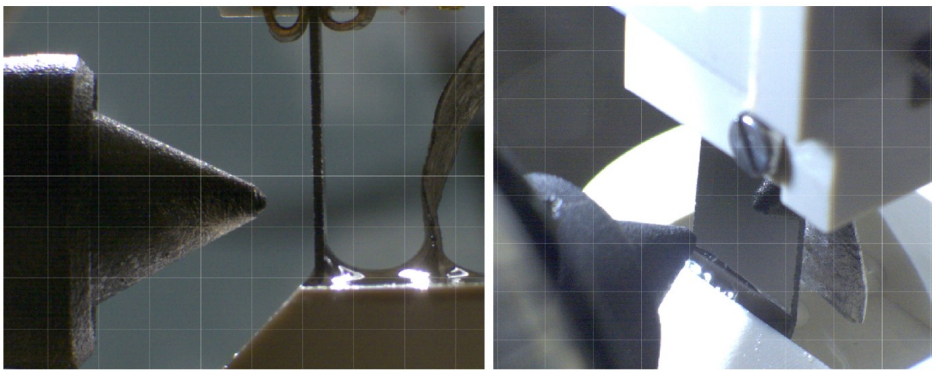

Figure 2.11: Pictures of the Dip & Pull NAP-PES setup at HIPPIE beamline.

### 2.5.1 Choices for this manuscript

A general set of rules and procedures were chosen to fit the data presented in this work. While the basic photoemission process would give a single energy value directly related to the binding energy of the electron in the orbital, the uncertainty principle gives a Lorentzian distribution of that energy. To this Lorentzian, an additional Gaussian contribution related to instrumental factors - depending on the analyzer and physical factors as phonon broadening - must be added. The result is the so-called Voigt function, defined by the convolution of the two different exponential functions as

$$\phi_{\text{voigt}}(x, \sigma, \gamma) = e^{-\frac{\sigma^2 x^2}{2-\gamma|x|}} \tag{2.21}$$

To distinguish between the Gaussian and Lorentzian character of the function, a parameter called "Gaussian/Lorentzian mix" can be defined as

$$glmix = \frac{lhm}{lhm + ghm} \tag{2.22}$$

Where a value of 0.0 will describe a pure Gaussian while 1.0 a pure Lorentzian. For our analysis, a $glmix$ of 0.3 was chosen. Going then to the background choice, the nature of our data, with many peaks overlapping, and the possibility to consider the area just around the peaks, made us choose the Shirley background; lastly, the matter of the calibration of the data is, in the case of operando measurements, a delicate matter that will be further discussed in the next paragraphs.

### 2.5.2 Data calibration and BE levels in electrochemical cell

As already anticipated, the accuracy of the information that can be obtained by XPS is heavily dependent on an appropriate calibration of the energy scale. However, this is no trivial task, especially when dealing with in situ experiments where chemical reactions take place and voltages are applied to the system, all during the measurements. We will try to introduce the basic notions necessary to understand this topic.

Raw data coming from an XPS measurement will have counts per second against kinetic energy as measured by the analyzer. However, most of XPS data are usually presented in terms of binding energy. The relation that binds binding energy and kinetic energy is usually written as follows:

$$E_b \approx h\nu - E_k \tag{2.23}$$

Thus, it is necessary to subtract the measured kinetic energy from the photon energy used for the measurement. While this could seem trivial, especially with lab sources with fixed energy (for example, using the Al K$\alpha$ source at 1.48 keV), it is always important, especially in synchrotrons, to carefully calibrate all the peaks on some well-known binding energies that can be used as references, as for example, the hydrocarbon $CH_x$ at 285 eV, partially coming from natural surface contamination, and partially from other (organic) species. We will now get into further details regarding the physics behind the process of photoemission to clarify some points that will be addressed in the next chapters.

### 2.5.3 Electrochemical potential of electrons

The electrochemical potential of the electron is derived from the laws of thermodynamics and can be expressed mathematically as:

$$\bar{\mu} = \left(\frac{\partial G}{\partial n}\right)_{T,p} \tag{2.24}$$

This expresses the work relative to a change in the number of particles for a system with constant temperature $T$ and pressure $p$. To have equilibrium between two phases, their electrochemical potential must be equal [102], such that:

$$\bar{\mu}_1 = \bar{\mu}_2 \tag{2.25}$$

When dealing with charged particles as electrons are, any work must also include the eventual electrostatic potential for the region taken into consideration, expressed as $eV$ where $e$ is the electron charge and $V$ is the applied electrical potential. This potential can be influenced by any external factor, and thus $\bar{\mu}$ becomes a function depending also on external factors [103]. It is convenient then to separate the electrochemical potential into a part only depending on the chemical nature of the material, and another one taking into account the electrostatic potential:

$$\tilde{\mu} = \mu + eV \tag{2.26}$$

Where $\mu$ is referred to as the chemical potential. For an uncharged particle or a system with no electrical potential applied, the electrochemical potential is equal to the chemical potential. It is also possible to show how $\tilde{\mu}$ is identical to the energy parameter of a Fermi-Dirac distribution function when the energy is calculated for an electron taken from its ground state to vacuum, $E^{\infty}_{\text{VAC}}$:

$$f(E) = \frac{1}{1 + e^{(E-\bar{\mu})/(k_B T)}} \tag{2.27}$$

where $f(E)$ is the probability to have an electron with energy $E$ according to the Fermi-Dirac equation, $T$ is the temperature, and $k_B$ is the Boltzmann constant. Then, $-\bar{\mu}$ equals the binding energy of a Fermi-level electron with respect to $E^{\infty}_{\text{VAC}}$. For this reason, $\tilde{\mu}$ is also referred to as the Fermi level [91], [104].

### 2.5.4 Work function

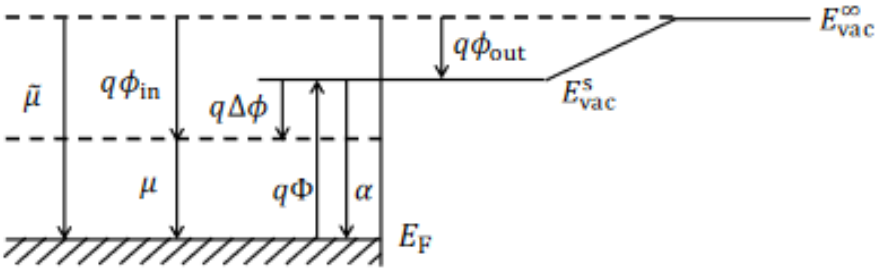


Figure 2.12: Energy Levels diagram [105]

A general definition of work function $\phi$ is the work needed to extract the photoelectron from the solid, which usually accounts for the difference between the incident photon energy and the residual kinetic energy of the photoemitted electron when measured. Thermodynamically, this can be expressed as:

$$q\phi = q\phi_{\text{out}} - \tilde{\mu} \tag{2.28}$$

Where $q$ is again the charge of the electron, and $\phi_{\text{out}}$ the electrostatic potential just outside of the system. Now, if we define the internal electrostatic potential of our solid as $\phi_{\text{in}}$, then we can rewrite the electrochemical potential as:

$$\tilde{\mu} = \mu + q\phi_{\text{in}} \tag{2.29}$$

And then we can rewrite the work function equation as:

$$q\phi = q\phi_{\text{out}} - \mu - q\phi_{\text{in}} = q\Delta\phi - \mu \tag{2.30}$$

Where $q\Delta\phi$ is also known as the surface dipole layer or potential barrier. The work function is then the sum of the bulk chemical potential $\mu$, independent of the surface, and the energy needed to get the electron through the surface dipole layer. The first term depends on the chemical species and the second term is related to external parameters such as the different faces of a single crystal or external electrical potentials.

All of this can also be expressed in an energy levels diagram, as shown in Figure 2.12 [105]. Here we see the energy level diagram for a metal crystal that clearly shows the different quantities introduced just before in the formulas. There, the difference between $\tilde{\mu}$ and $q\phi$ can be seen in a more straightforward way: it can be seen how the former is referenced to the $E^{\infty}_{\text{VAC}}$, which does not depend on the crystal plane, while the latter is referred to a vacuum level $E^{S}_{\text{VAC}}$ that depends on the electronic structure of the investigated surface. It is indeed for this reason that it is not possible to consider the work function as an intrinsic property. Technique and condition of the material will change the value of the work function, as in the case of the slight difference between the thermionic work

function (when an electron is taken out of a heated metal through a high temperature) and the photoelectric work function. While this matter can be neglected in common XPS measurements as we will see in the next section, it is important to keep it in mind when external perturbations are applied to the system, as is the case for *in-situ* electrochemical measurements.

### 2.5.5 Calibrating energies for XPS solid samples

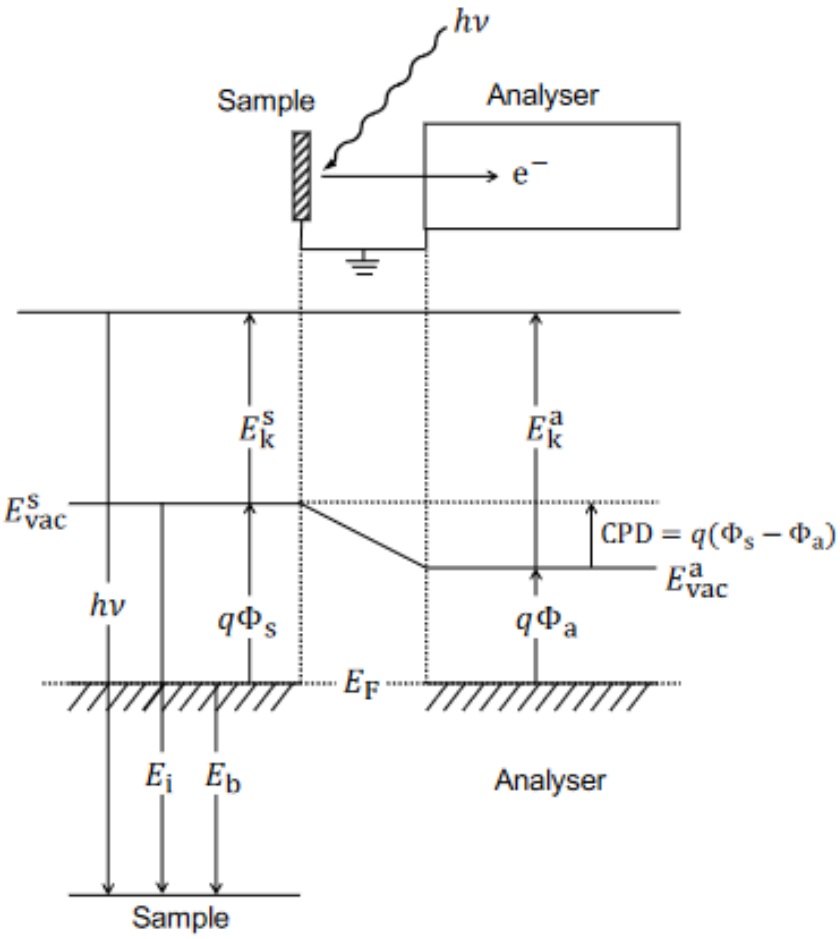


Figure 2.13: Energy levels diagram for XPS [105].

We already mentioned how the binding energy in XPS is usually expressed relatively to the Fermi level, $E_F$. In fact, the Fermi level is the most easily accessible reference in the sample, specifically when dealing with conductive materials. To calibrate the binding energy, we make a simple assumption: through electrical connection, the sample is grounded

together with the analyzer, thus implying that the two are in equilibrium and so their Fermi levels are aligned. This translates into the energy diagram shown in Figure 2.13. An emitted photoelectron must surpass the sample's work function $q\phi_s$ to be ejected and sent through the analyzer to have its kinetic energy measured. Such an analyzer is, however, going to have its own work function $q\phi_a$, which the electron will also experience. Then if we write the energy of the photoemitted electron as:

$$E_k^s = h\nu - E_b - q\phi_s \tag{2.31}$$

Then the kinetic energy that will ultimately get measured will be $E_k^s$ plus the difference in work function of the sample and the analyzer, so that:

$$E_k^a = h\nu - E_b - q\phi_s + (q\phi_s - q\phi_a) = h\nu - E_b - q\phi_a \tag{2.32}$$

It can be seen how, in the end, the two $q\phi_s$ values cancel each other, and it is then possible to ignore the value of the sample's work function, as long as the work function of the analyzer is known.

# Chapter 3

# Study of the SEI formation using operando NAP-PES

In this chapter we will present the results obtained on the SEI formation on a carbonaceous electrode by NAP-PES. First, the experimental procedure will be described, together with the procedure for the data analysis. Three different electrolyte formulations, namely PC ($C_4H_6O_3$), PC + VC ($C_3H_2O_3$) and PC + EC ($(CH_2O)_2CO$), were selected to understand their influence on the SEI in terms of both composition and formation.

## 3.1 Description of the Dip & Pull experiment

The electrochemical chamber available at HIPPIE permits to perform XPS experiments at pressures higher than what is normally available, from the $10^{-8}$ mbar usually needed for laboratory XPS to up to $10^{-2}$ mbar. This means that it is possible to have liquid species in the analysis chamber, thus having possible easy access to the solid-liquid interface.

Near Ambient Pressure X-ray Photoelectron spectroscopy (NAP-PES) setups have been already used to study liquid systems and the solid-liquid interface [106]–[108], but while the Dip & Pull methodology was well established in the works of Källquist et al [70], [109], [110], an application to the case of the SEI formation was still missing. The difficulties in accessing the solid-liquid interface with XPS have already been explained before. The low mean free path of photoelectrons and the need for UHV usually limit both the presence of

liquids in the analysis chamber and the probe depth of the technique. In the Dip & Pull procedure, the NAP-PES setup overcomes the limitation related to the presence of liquids, allowing the interphase to be measured directly. In fact, by slowly pulling out the electrode from the electrolyte, a thin meniscus can be formed. With the right combination of flat surface and liquid viscosity, it is possible to obtain a meniscus thin enough to allow the access to the interface. Through this meniscus, it is also possible to maintain in electrical contact the probed electrode and the electrolyte for *in situ* electrochemical experiments.

### 3.1.1 Choice of materials and validation

The first step was to choose the right combination of electrode and electrolyte: it was crucial to have a system that would resemble closely a real battery, while also allowing performing the measurements, forming a good and thin enough SEI.

In this work, we opted for glassy carbon (GC) as carbonaceous electrode. This carbon composite strongly resembles the edge planes of graphite, while having a microscopically "flat" surface similarly to glass. Moreover, its structure prevents $Li^+$ intercalation, thus heavily simplifying the electrochemistry processes happening at the interface and allowing a first study that could focus only on the degradation and deposition ones. The liquid part in this system is the electrolyte. The electrolyte of choice for BIG-MAP, however, was not compatible with the requirements of the NAP-PES setup: in fact, the vapor pressure of EMC, one of the two solvents used in the mixture of LP57, was too low to enable measurements, evaporating at $39$ mbar and thus saturating the atmosphere of the analysis chamber. PC, instead, had a vapor pressure of around $4 \times 10^{-2}$ mbar, thus allowing to measure at lower pressures with a good signal to noise ratio. The PC was then mixed with $1$ M of $LiPF_6$ salt, as is the same used in LP57. Lastly, the cell was assembled in half-cell configuration, meaning that the cathode is a simple metallic lithium ribbon to trigger mainly the reactions occurring at the anode surface. This simplifies the processes at the cathode surface and allows to focus on the anode, while assuring a continuous supply of $Li^+$.

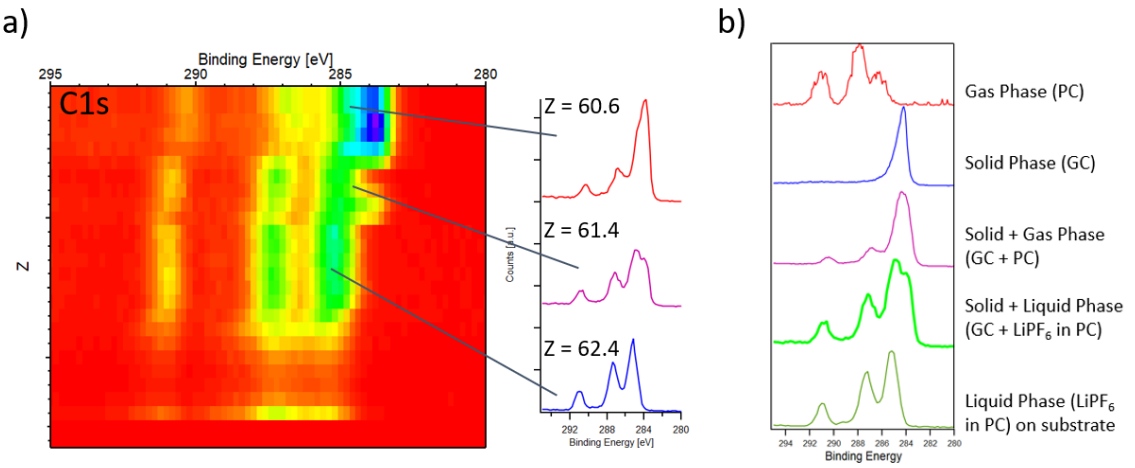


Figure 3.1: a) C 1s XPS spectra collected at different vertical positions on the GC electrode. b) C 1s XPS spectra of different phases measured in our system.

The last step was to verify that the combination of electrolyte and glassy carbon would allow a meniscus thin enough to access their interface. The result is shown in Figure 3.1: the glassy carbon electrode was dipped into the electrolyte, and was then slowly pulled out by scanning the vertical position by $0.1$ mm (the smallest step available with HIPPIE motors stage). At each vertical position, a fast acquisition of C 1s XPS spectrum was collected. To identify the different chemical phases, we have compared their XPS spectra to those obtained on relevant references. We have then also acquired the XPS spectrum corresponding only to the gas phase of PC, as we have decreased the pressure enough to evaporate the PC; the glassy carbon electrode was measured under vacuum on the clean sample, to have only the contribution coming from the surface of the electrode; the C 1s XPS spectrum on PC covering the glassy carbon electrode was collected as well. The comparison between the XPS spectra as a function of the vertical position along with the references was applied to distinguish between three interesting regions: i) only the electrode and eventually the PC vapor; ii) only the PC liquid bulk electrolyte; iii) the thin interphase between the glassy carbon and the PC. To obtain the signal from the PC liquid bulk electrolyte, we measured the bottom part of the electrode, where the liquid PC formed a thick layer, and the XPS spectrum can be assigned to PC because of its similarity with previous XPS data. In fact, XPS measurement of the PC solvent was performed at IPREM laboratories in Pau, in UHV

at low temperature (-140 °C) where the PC is a solid and is then possible to measure it with conventional XPS. The result, shown in Figure 3.2 [101], indicates a strong resemblance with our data, confirming that we were indeed measuring the liquid phase of the electrolyte. The spectrum at the top (z=62.4 mm) was very close to the one of bulk PC. The spectrum collected in the intermediate z position (z=61.4 mm), was a combination of the solid GC and the liquid PC electrolyte: it represents the area where is possible to measure through precursor wetting layer up to the solid GC substrate. This procedure simplified the search of the SEI region: for the first time, a carbonaceous material has been used as electrode, acting as internal reference for the energy calibration and position validation.

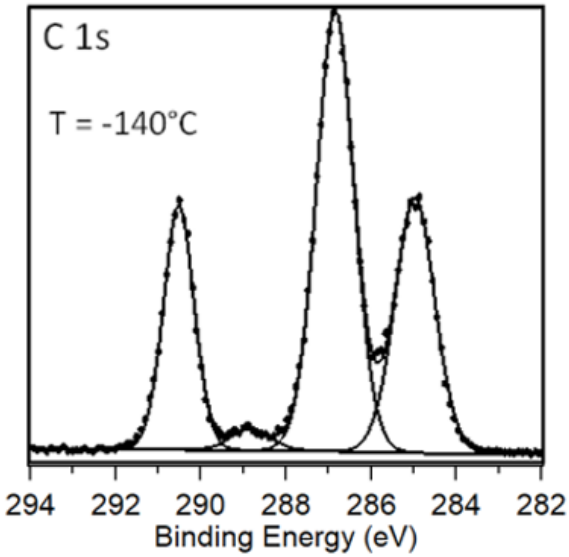


Figure 3.2: C 1s XPS spectrum of PC solvent in measured at T=-140 °C with an Al $K_\alpha$ source. ($h\nu = 1489$ eV) [101]

### 3.1.2 Experimental procedure

Figure 3.3 summarizes the experimental procedure applied during the *operando* Dip & Pull NAP-PES experiment. Before starting any measurements, the system was slowly pumped to go from ambient pressure to the lowest pressure compatible with our electrolyte, around $0.25$ mbar. Reaching that value from ambient pressure causes evaporation of traces of moisture in the electrolyte, thus releasing bubbles during the change in pressure and for an additional amount of time after reaching the desired value, until an equilibrium between the

electrolyte and the chamber atmosphere is reached. Then, when the bubbling has stopped, it is possible to start the procedure without the risk of having liquid from the bubbles enter in the analyzer. The experiment starts at open circuit voltage (OCV), corresponding to the equilibrium position $x_0$, with the electrode dipped into the electrolyte and with no potential applied.

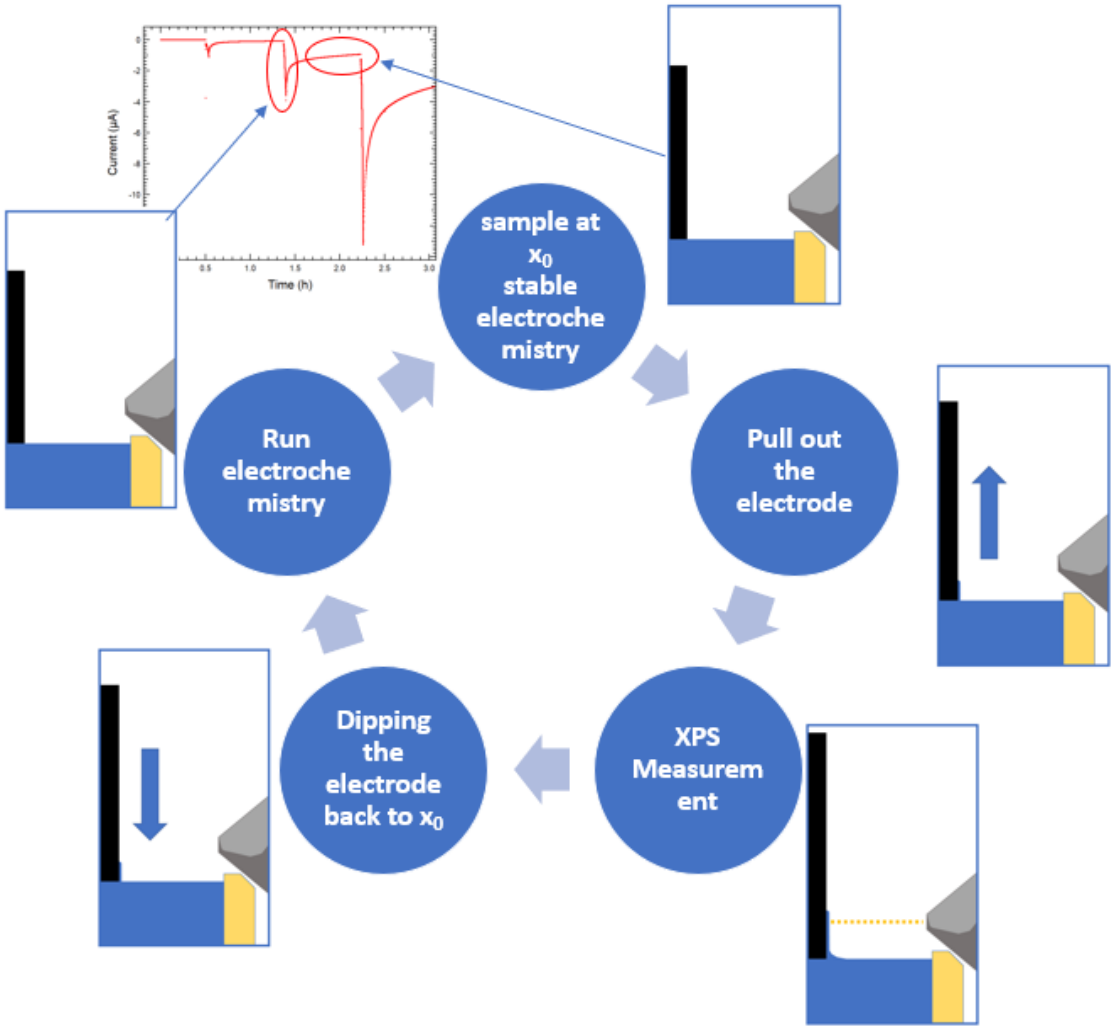


Figure 3.3: Experimental procedure applied for the Dip & Pull NAP-PES experiment.

Then, to find the suitable spot, the electrode is slowly pulled out, and the C 1s spectra at different vertical positions are collected. First, just the glassy carbon can be measured then the interface as shown in Figure 3.3. To make sure that the measurement is taken on the thin meniscus connected to the bulk electrolyte and not on a single drop, the electrode is pulled out more to observe the signal originating only from the liquid phase. When a

good position is identified, the core peaks of interest are acquired. Finally, the electrode is brought back to the position $x_0$, and the electrochemical procedure is started. In our case, the electrochemical procedure mimics a cyclic voltammetry (CV), scanning the voltage of the system from OCV vs $Li^+$/Li (around $3.1$ V for Carbon vs Lithium) to nearly $0$ V vs $Li^+$/Li, without reaching $0$ to avoid lithium plating. This was done through several voltage steps: starting from OCV, the system is slowly brought with small voltage steps to a new applied voltage, then the voltage is held for around $1$ h until the current is stabilized. This is crucial to probe the system as close as possible to the equilibrium. When the equilibrium is reached, it is possible to pull out the electrode and start again with the XPS collection.
Note that when we refer to "meniscus", it is actually not on the meniscus that our measurements take place. Indeed, the meniscus is usually very thin but not thin enough ($1-10\,\mu$m) to allow the measurement of the interface with the low energy photons available at HIPPIE. Instead, our beam is focused on the so-called "precursor wetting layer", a thinner ($\sim 1$ nm) precursor film that forms on the wet solid surfaces just in front of the meniscus [111].

## 3.2 Energy calibration of NAP-PES spectra

This approach brings forth new challenges in relation with the calibration and the interpretation of the spectral binding energies: the presence of two different phases, one of which is electrically insulating, and the addition of the electrochemical counterpart during the XPS measurement calls for a new effort on data interpretation.

### 3.2.1 Calibration and interpretation of the binding energies

Dealing with *in situ* measurements where a voltage is applied to the system and the system itself changes during the measurement was proven not to be an easy task. As seen in the chapter 2.5.5, XPS binding energies can be approximated from the measured kinetic energy and the work function of the analyzer.

The situation is different in systems under applied potential. The approach here pre-

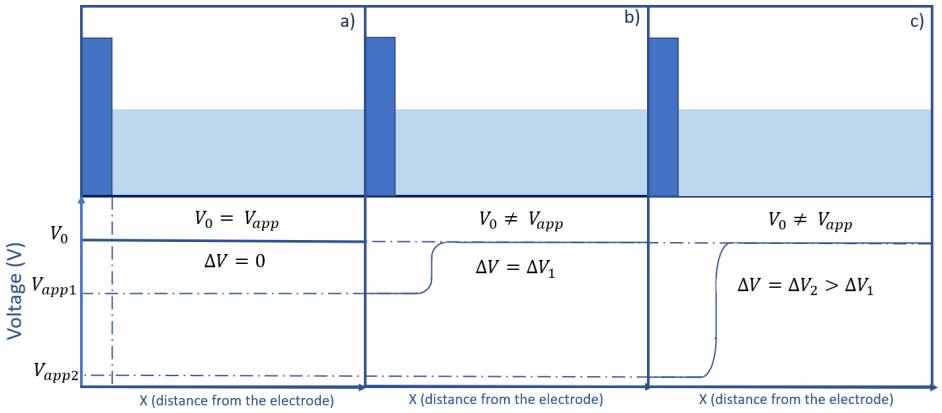


Figure 3.4: a) At OCV, the electrolyte and the electrode have the same electrochemical potential. b) and c) effects on the applied voltage on the liquid electrolyte as a function of the distance from the electrode.

sented was firstly described by Källquist et al. [112]. Taking into account the applied potential, we can express the measured binding energy $E_b^{\text{eff}}$ as:

$$E_b^{\text{eff}} = E_b + \mu_{\text{el}} + \mu_{\text{chem}} \tag{3.1}$$

It is then possible to correlate the actual binding energy $E_b$ of the photoelectron to the measured value $E_b^{\text{eff}}$, that is dependent on the electrical $\mu_{\text{el}}$ and chemical potential $\mu_{\text{chem}}$ of the system. We can start with an easy approximation thanks to our choice to measure the system only when the electrochemistry reaches an equilibrium, so that it is reasonable to assume that no chemical processes are happening. Thus the $\mu_{\text{chem}}$ term can be considered as null, and we can simplify:

$$E_b^{\text{eff}} = E_b + \mu_{\text{el}} \tag{3.2}$$

Here $\mu_{\text{el}}$ is the applied potential, thus $\mu_{\text{el}} = \Delta V_{\text{app}} \cdot q_{\text{el}}$ with $q_{\text{el}}$ indicating the electrical charge of the single electron. This provides a linear relationship between the binding energy $E_b$ of a system upon applied voltage and the measured binding energy $E_b^{\text{eff}}$. Keeping in mind the definition of eV, in which the binding energy is usually expressed,

$$1\,\text{eV} = 1\,\text{V} \cdot q_{\text{el}} \tag{3.3}$$

then we can expect to have a 1 eV shift in BE for 1 V of applied voltage.
This relation explains the shift of the binding energy observed in the system when a voltage is applied. However, it does not consider the effective voltage at the interface where different situations coexist: due to the cabling choices on the beamline, the anode is always grounded together with the analyzer while the rest of the system is actually subjected to a potential. Thus, the binding energy of the species coming from the solid phase of GC will not be dependent on the applied voltage while the BE of the bulk liquid electrolyte that actually is subject to $\Delta V$, will shift accordingly. The intermediate condition between these two represents the interphase between the electrode and the bulk electrolyte, where the formation of SEI takes place.

Note that due to the electronic insulating character of the electrolyte, it is actually the electrolyte that has a "constant" voltage while a $\Delta V$ is applied on the anode. However, since the anode is grounded with the analyzer, we consider the voltage of the anode as the reference, defining as $V_0$ the voltage on the anode, and $V_{\text{app}}$ the voltage applied on the system, such that $\Delta V = V_{\text{app}} - V_0$ will be equal to $V_{\text{app}}$ since $V_0 = 0$ by construction. Figure 3.4 summarizes the different cases. The top panel shows the electrode on the left and the electrolyte on the right. When there is no applied voltage (OCV), the whole system is at equilibrium, and the electrical potential is the same. Under applied voltage, a potential difference $\Delta V$ appears between the glassy carbon electrode and the electrolyte, which also affects the BE energies of the respective species. Moreover, since the electrode is grounded to the analyzer, the BE of the electrolyte species will shift linearly with the applied voltage. This kind of result was already obtained by Källquist et al. [70], [109], [110] and validated also by our experiments. In this work, however, our goal is not to study the formed species dissolved in the electrolyte but the species formed at the interface. This implies some additional steps to the interpretation of the binding energies. When a voltage is applied, the

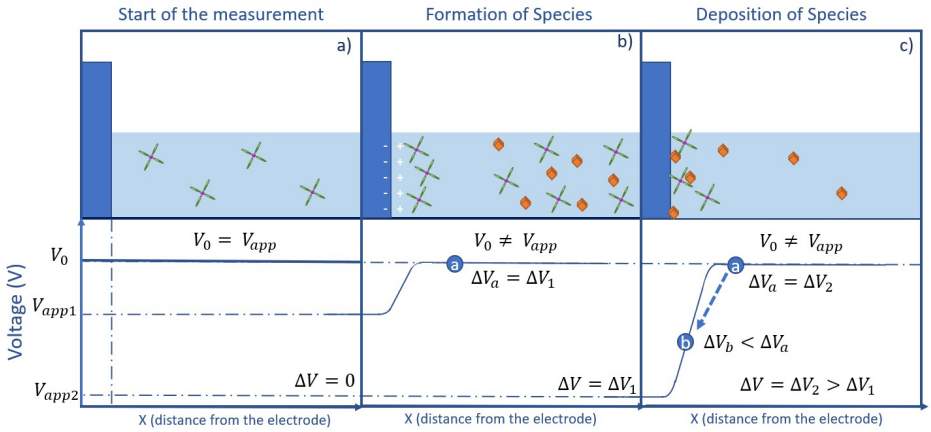


Figure 3.5: a) Chemical species dissolved in the electrolyte at OCV. b) Some of the degradation species dissolved in the electrolyte, thus having the same voltage applied. c) The SEI species start to deposit on the electrode, and "feel" a different applied voltage.

charged species in the electrolyte form an electrical double layer [106], [113]–[115]. Due to the fast kinetics of this process, we cannot describe directly this process. However, the slower processes of formation of species and their deposition can be probed at the interface during discharge. We show the possibilities related to this in Figure 3.5. While it seems intuitive that the formation of a new species implies the appearance of a new peak in the XPS spectra, it is less obvious how the shift of species BE from the interface upon discharge could provide their distance from the glassy carbon electrode. In fact, the chemical species formed during the electrolyte reduction will be subjected to the external potential acting on the system, and their BE will shift accordingly; however, when the electrolyte is reduced around 1 V, some of these species will deposit on the surface of the electrode to form the SEI. According to their position with respect to the glassy carbon, the effective voltage will influence the binding energy of the core level peaks. It will then be possible to observe different trends in the BE vs voltage graphs: i) species shifting linearly with respect to the applied voltage will be related to the ones in the bulk liquid. Lower slopes are related to species on the interface where the applied voltage is lower. ii) species at the surface not shifting during voltage changes. iii) species that form in the electrolyte will have an initial behavior as for the electrolyte, with their BE linearly shifting with applied voltage. However, their BE will stop shifting in the moment they get deposited on (and, thus, in contact

with) the surface of the electrode, becoming then grounded to the analyser. In the end it was decided to treat the data hereby discussed without any kind of calibration, such that the binding energies showed are just the result of the subtraction of the KE measured and the photon energy. This way there is no risk to lose information on the important BE shift that could happen on the species. This work will mainly focus on the information that can be extracted from the different Binding Energies and their shift in relation with the applied voltage.

### 3.2.2 Peaks intensity ratio

XPS peak intensities and their relative ratio provide useful information on the relative presence of species on the measured sample area.
Ideally, an *operando* experiment would allow to follow the presence of each chemical species through the relative intensity of the respective peak compared to the wole area of the ensemble. However, the peak intensity is not depending only on the quantity of species but also, firstly, on the beam intensity and the counting time and number of scans. During our experiment, these factors were kept unchanged, but other possible sources of changes in intensities are actually present during an XPS experiment: the distance from the analyser, the relative depth of the photoemittor and the subsequent loss of electrons due to inelastic scattering processes are also possible ways to variate the final intensity of the peak. This becomes a great factor of uncertainty when the thickness in front of a buried sample changes over time, as in the case of a non controllable meniscus layer. For this reasons, extracting the correct XPS intensity was a difficult task, as we could not obtain a proper calibration of the intensities that could take into consideration all the different changes in our system.
Firstly, the nature of the system implies that the thickness of the layer of electrolyte is not constant over measurement. Even when each dip and pull is performed at the same positions, the shape, thickness and exact position of the meniscus edge change at each iteration, making it impossible to have a constant thickness of electrolyte on the glassy carbon. This means that even when taking different measurements of the system at V = OCV, where no

SEI is formed yet and the different thicknesses are the only source of changes in the intensities, there would be different results, where the signal coming from the GC substrate would be more or less intense depending on the relative position of the beam on the electrolyte layer. However, the Glassy Carbon could have served as a good reference for calibration if this where to be the only source of uncertainity. Regrettably, there is a second point to take into consideration that made using the GC peak for intensities calibration impractical: indeed, lower intensities of the GC peaks would mean a thicker electrolyte and vice versa, but during discharge the SEI would also form, presenting species at the same binding energies as the electrolyte. This adds a new factor to the loss of intensity of the electrode peak, since then it cannot be estimated if the loss of intensity of GC is due to a thickening of the SEI or just a thicker liquid meniscus, or, to be more exact, which of the two is more or less responsible for the intensity loss of the GC peak, making it difficult to have a proper calibration that would allow to extract informations from the XPS peak intensities. For these reasons, in the following we will focus solely on the binding energies, while the relative intensity variation of the different species will not be discussed in depth.

## 3.3 The SEI formation using PC-based electrolyte

We will now present the results obtained in the electrolyte with only PC solvent. First, we will show the results on the thick PC meniscus, then on the precursor wetting layer. All the XPS measurements were collected with photons of 1.8 keV which represents the best trade-off between probing depth, photon intensity and cross section.

### 3.3.1 Results on the thick liquid meniscus

Firstly, the XPS C1s spectrum of the electrolyte was measured to compare it to the XPS C1s spectrum of PC measured at low temperature (seen in 3.2). As shown in Figure 3.6, the two spectra are very similar, all presenting three main peaks related to the three environments of C atoms in the PC molecule. These correspond to (from the lower BE to the higher) the

C-H bonds (blue), the C-O bonds (green) and $CO_3$ (purple). An extra minor component is found between C-O and $CO_3$, at around 292 eV and related to carbon atoms bound to two oxygen atoms.

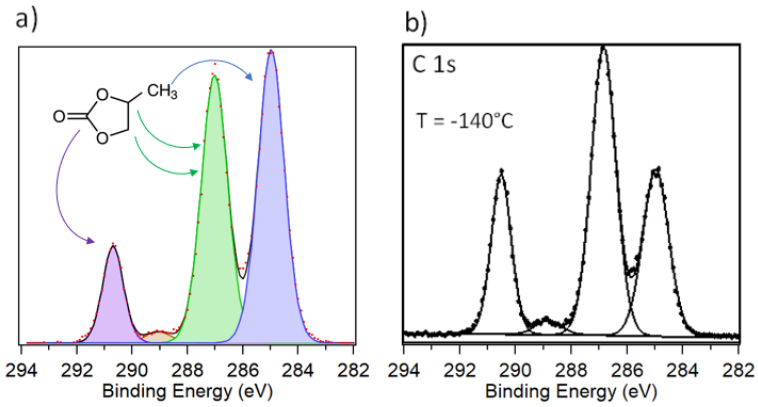


Figure 3.6: C 1s XPS spectra of PC as solvent of the liquid electrolyte measured at HIPPIE beamline (a), and as a frozen drop of PC at IPREM (b).

The structure of the PC molecule would suggest that the ratio between the C-H and the $CO_3$ peaks should be similar, as is observed in Figure 3.6. However, due to the surface contamination in the analysis chamber during an ambient pressure experiment, we can expect to have unavoidable extra hydrocarbon species. The experiment was performed with the methodology illustrated in Figure 3.3. The electrochemical results are displayed in Figure 3.7: in a), measured current and applied voltage are shown as a function of time. The blue line shows how the stepped voltage was applied, going from OCV (3V) to 0.05 V through different steps.

At each step, we waited around 40 minutes to stabilize the flowing current before starting the XPS measurements (red curve). The steep changes in current are related to the changes in height of the electrode after the "pulling" process and the subsequent change of the exposed area. The resulting voltage vs current curve is shown in right panel of Figure 3.7.

The resulting XPS curves are shown for the three main core peaks of our system: carbon, oxygen, and fluorine. In Figure 3.8a), the C 1s peaks are shown. The shape and relative intensity of the components do not change significantly over the discharge and are related

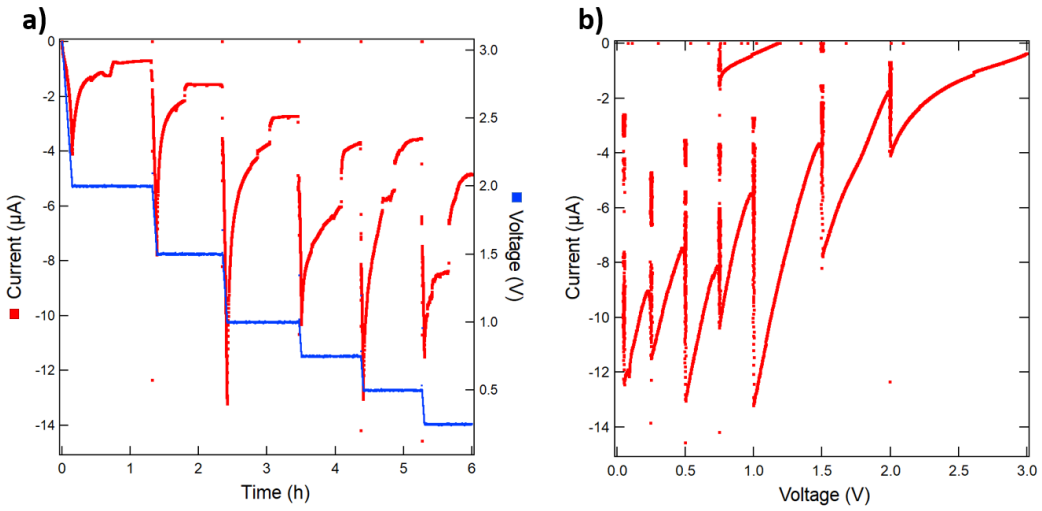


Figure 3.7: Electrochemical profile of the applied potential and resulting current during the *in situ* experiment. a) The applied voltage (blue) and the resulting current (red) as a function of time. b) The profile I vs V shows the resulting "stepped" CV.

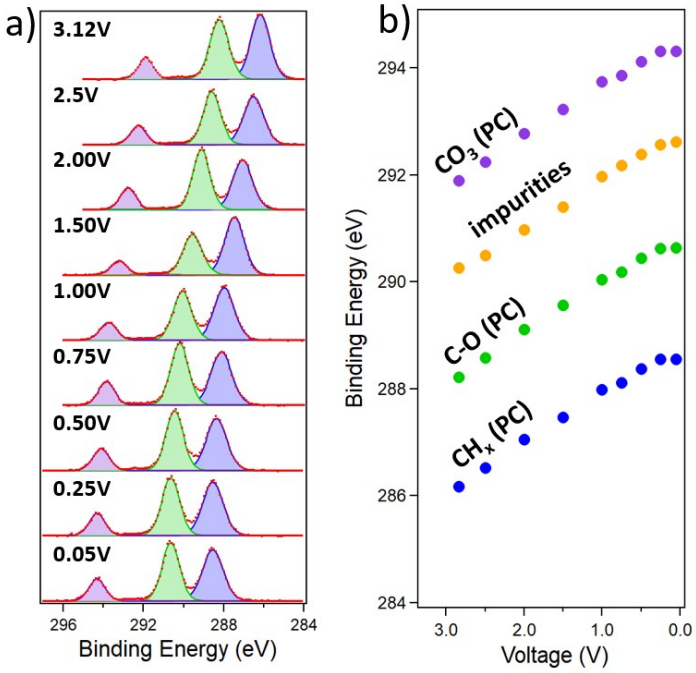


Figure 3.8: a) C 1s XPS spectra measured during discharge on the PC bulk liquid meniscus. b) Evolution of the C 1s binding energies of the main components as a function of applied voltage.

to the PC molecule structure. In Figure 3.8 b), the binding energy of the peaks versus voltage is shown: as expected, the three carbon peaks related to the PC solvent molecule shift linearly with the applied voltage until 1 V, while they exhibit a slightly lower slope below 1 V. This behaviour was already observed [110] and is related to the charge transfer

occurring at the electrode/electrolyte interface, leading to a local change in the electrolyte electrostatic potential. Importantly, the kink in the linear shift of the binding energies is observed at 1 V vs $Li^+$/Li, where the electrolyte is expected to be reduced and triggering the SEI formation.

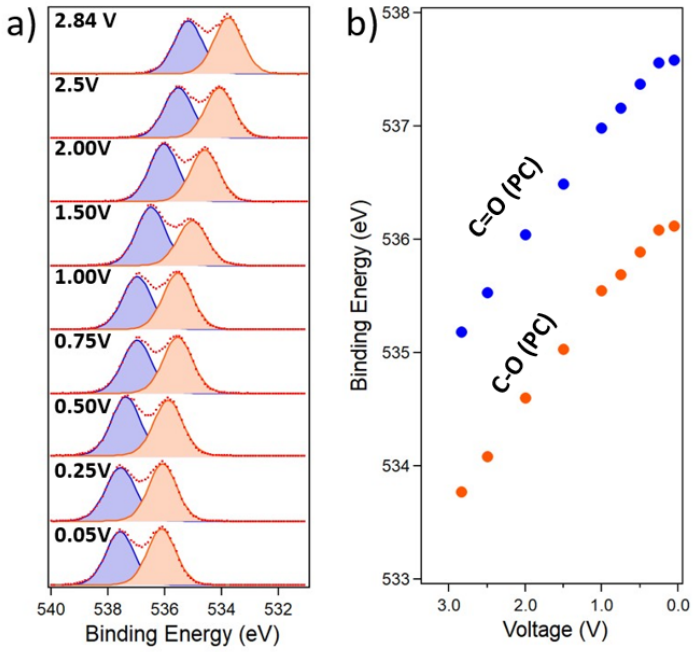


Figure 3.9: a) O 1s XPS spectra measured during discharge on the PC bulk liquid meniscus. b) Evolution of the O 1s binding energies of the main components as a function of applied voltage.

As a support to our interpretation, we can also extract the information related to the core level peaks of oxygen and fluorine, in Figure 3.9 and Figure 3.10, respectively.

The signal of these species comes from either the oxygen atoms in the PC molecule or the fluorine of the $LiPF_6$ salt, exhibiting the same behavior as the carbon peaks. In Figure 3.9a), the oxygen 1s XPS core peaks show two main signatures related to the C-O and C=O bonds of the PC molecule. Their relative ratio is stable upon discharge, and their binding energy evolution, as seen in Figure 3.9b), follows the expected linear behavior already observed for C 1s. Similar observations can be made for the fluorine 1s spectra in Figure 3.10: in Figure 3.10b), we see two main peaks related to the dissolved $LiPF_6$ salt (yellow) and dissolved intermediate reduction products (green) shifting linearly with voltage as seen

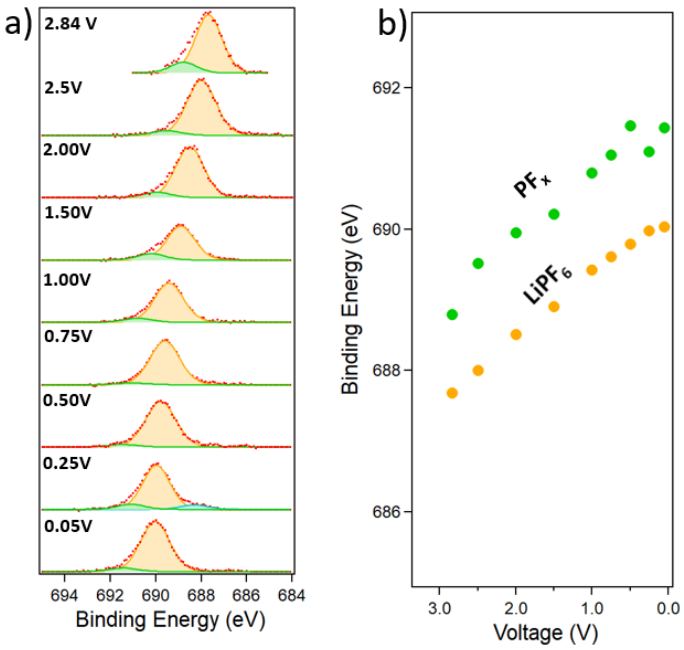


Figure 3.10: a) F 1s XPS spectra measured during discharge on the PC bulk liquid meniscus. b) Evolution of the F 1s binding energies of the main components as a function of applied voltage.

before. The shapes and ratios do not change during the discharge, as seen in Figure 3.10a), while the appearance of another peak has to be noted at 0.25 V and is probably related to a distortion of the signal due to charging effects.

### 3.3.2 Results on the PC || GC interphase

Focusing on the thinner precursor wetting layer, a different shape of the C 1s XPS spectra is obtained. Looking at the C 1s signal in Figure 3.11 a), several peaks are already observed at OCV. The red peak at lower binding energies (285.5 eV) is related to the signal of the glassy carbon electrode. Its asymmetric shape is commonly observed in carbonaceous electronic conductors as graphite or carbon black. As already explained, since the electrode is grounded to the analyser, the BE of the GC electrode does not shift as a function of applied voltage, showing only fluctuations of around $\pm 0.1$ eV compatible with the measurement uncertainty.

We then have two other additional components, compared to the results in 3.3.1. One

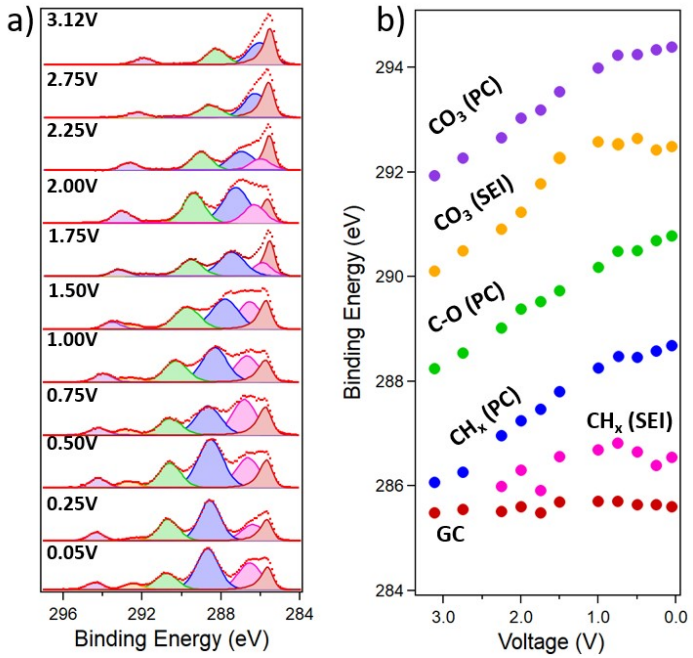


Figure 3.11: a) C 1s XPS spectra measured during discharge on the PC||GC interphase. b) Evolution of the C 1s binding energies of the main components as a function of applied voltage.

is the orange peak that is located between the purple and the green one corresponding to C-O and $CO_3$. While a peak is present at this energy also on the thick liquid meniscus, its behavior and intensity prove that is arises from a different species, as also confirmed from the results on the O 1s peaks. Indeed, this peak reaches up to 80% of the $CO_3$ peak intensity at the end of the discharge. Moreover, its binding energy changes are strictly related to the ones of the new component present in O 1s indicated as SEI in figure 3.12. This indicates a different origin compared to the weak parasitic peak observed in Figure 3.2 and hits for the formation and deposition of inorganic carbonates species as could be $Li_2CO_3$ or other carbonates. The second additional component is the pink one between the red GC electrode and the $CH_x$ blue one. While its binding energy is subject to a significant error due to the overlap with $CH_x$, upon discharge their energy splitting allows for a more accurate identification. Looking at the evolution of the binding energies in Figure 3.11 b), we can notice that both the pink and the orange peaks behave differently from the previously observed ones: both peaks first exhibits a positive linear shift between OCV and 1 V vs. $Li^+/Li$ of 1 eV/V, then they change the trend between 1 V and 0.05 V, with a slope of around -0.15

eV/V. We can explain the behavior of the pink and orange peaks following the description in Figure 3.5.

The potential difference between the electrode surface and the liquid electrolyte provokes a different shift on their BEs, as the different position of the species with respect to the GC electrode results in an effective applied voltage. Between OCV and 1 V vs $Li^+$/Li, the binding energy of the orange component shifts linearly, similarly to the behavior of the meniscus species. However, below 1 V vs $Li^+$/Li, the negative shift implies that the potential difference decreases, meaning that the species are getting closer and depositing on the electrode surface. We conclude that this component corresponds to an inorganic carbonate such as $Li_2CO_3$ or $ROCO_2Li$, formed by decomposition of PC at the surface of the electrode of species like lithium propylene decarbonate ($LiO_2CO$-$CH(CH_3)CH_2$-$OCO_2Li$). These components' chemical nature probably changes during the decrease of potential, and decomposition reactions are triggered. The similar evolution of the pink component makes it possible to assign it to the same chemical species, as for example the $CH_3$ group in the lithium propylene carbonate, while it could also be related to any kind of chemical species deposited on the surface that is containing hydrocarbon groups.

We can find additional proof of the formation of SEI from the other core peaks collected: in Figure 3.12 and Figure 3.13, we can see the O 1s and F 1s core peaks' evolution and the components BE versus voltage. In the case of the O 1s, there are two main components that can be attributed to C=O (red) and C-O (blue) coming from the PC molecule. This attribution is based both on the BE value at OCV and their behavior during discharge, coherent with the one showed from the oxygen species in the liquid sample. There is, then, a third component, that follows the same behavior as the inorganic carbonates shown in Figure 3.11. The shift is 1.1 eV/V before 1 V and of -0.15 eV/V for the voltage between 1 V and 0.05 V vs $Li^+$/Li. Also taking into consideration the BE difference between the C 1s and the O 1 orange components, being constant at ~241.8 eV, we can conclude that this component is coming from the same $Li_2CO_3$ from where we have a signal in the case of C 1s,as well as other different lithium alkylcarbonates $ROCO_2Li$, thus validating our hypothesis. Then in

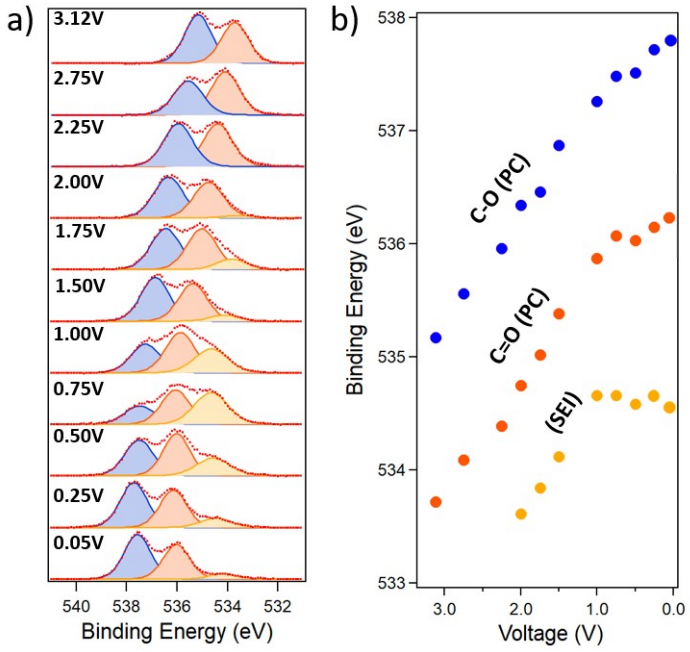


Figure 3.12: a) O 1s XPS spectra measured over discharge on the PC||GC interphase. b) Evolution of the O 1s binding energies of the main components as a function of applied voltage.

Figure 3.13, we can see the peaks for F 1s over discharge and their BE vs voltage. At the start of the experiment, the only component visible is the one that can be associated with the $LiPF_6$ salt in the electrolyte. This component (orange) behaves accordingly for the whole discharge cycle, confirming its provenance from the liquid electrolyte. However, another weaker component comes out at 2.5 V vs $Li^+/Li$. This component is positioned at the BE assigned for LiF, a typical component of SEI for our system. The BE for this component does not seem to be affected by the applied potential (when taking into consideration the error due to its weak intensity and low signal to noise ratio) but, according to our model, it means that LiF is in direct electronic contact with the electrode from the start. When taking into consideration the insulating character of LiF, we can also conclude that the LiF layer remains very thin after this first cycle, since otherwise the outer part of the layer would not give this kind of result. We have here demonstrated the interest of NAP-PES for the study of solid-liquid interface, bringing results on the SEI formation as a real-time direct observation of the deposition and formation of chemical species.

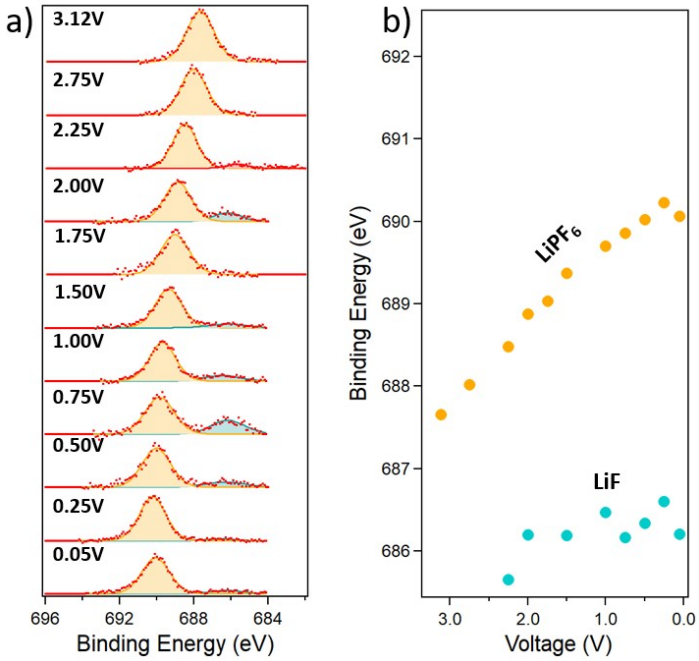


Figure 3.13: a) F 1s XPS spectra measured over discharge on the PC||GC interphase. b) Evolution of the F 1s binding energies of the main components as a function of applied voltage.

## 3.4 The influence of EC solvent

Propylene Carbonate (PC) and Ethylene Carbonate (EC) have a very similar structure (Figure 3.14), however their differences when forming the SEI have been often reported, and referred to as the "EC-PC mystery" [78], [79]. In fact, the two solvents show several electrochemical differences, especially in the formation of SEI: while PC has a much more extensive reduction, forming an initially thick layer of organic species over the inorganic one, this layer then rapidly dissolves, leaving just the inorganic one. On the contrary, the EC reduces less and forms a thinner but more stable SEI. These differences have been explained by the bulk properties of their reaction products [116] or on their different competitiveness on solvating $Li^+$ over $F^+$ [79]. However, there is an ongoing debate on the exact mechanism of the SEI formation for the two solvents.

To solve this puzzle, we used *operando* NAP-PES to study the SEI formation using a mixture of PC and EC solvents (2:3). The choice for the ratio between PC and EC was derived from the need to incorporate the EC in the formulation while maintaining a density that would

still allow to form a thin enough layer on the surface to let us access the interface.

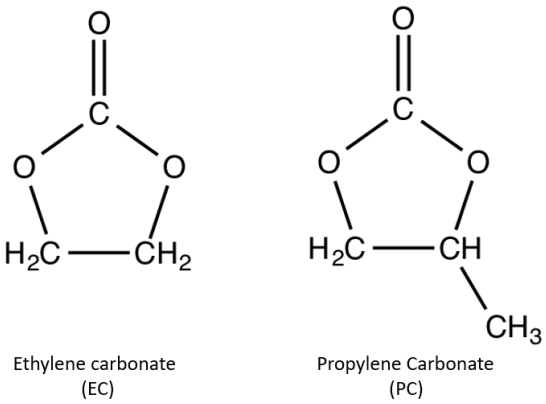


Figure 3.14: Structure of EC and PC molecules.

### 3.4.1 Results on the thick liquid meniscus

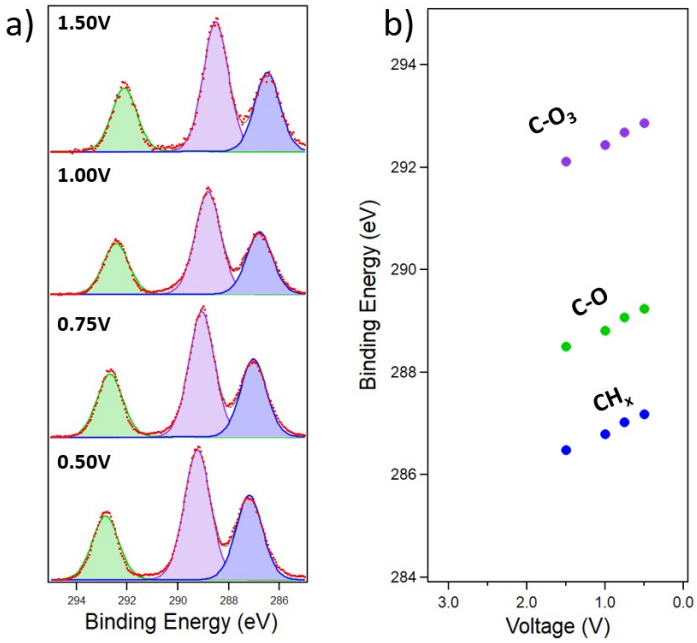


Figure 3.15: a) C 1s XPS spectra measured during discharge on the PC:EC bulk liquid meniscus. b) Evolution of the C 1s binding energies of the main components as a function of applied voltage.

In Figures (3.15, 3.16, 3.17), the C, O and F 1s XPS spectra are shown as a function of applied voltage, along with the BEs of the chemical components. Due to some problems during the beamtime, only a limited dataset was successfully obtained. Similarly to the

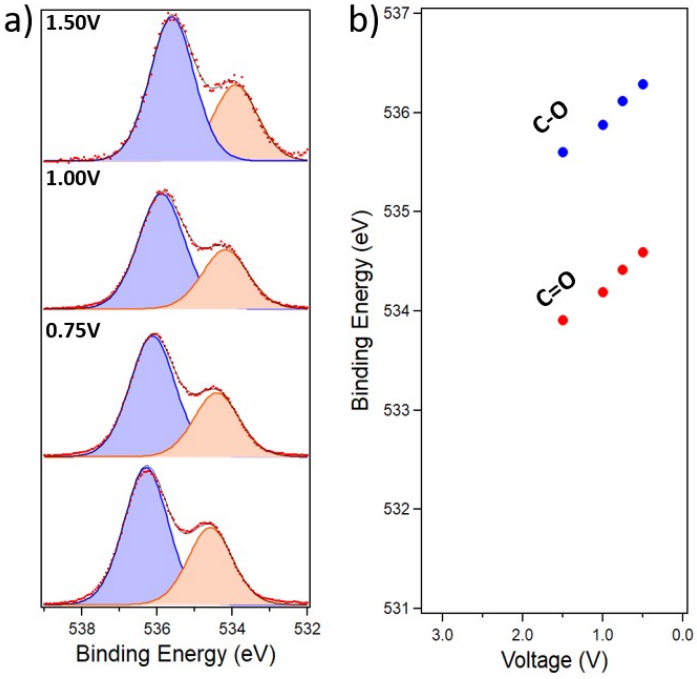


Figure 3.16: a) O 1s XPS spectra measured during discharge on the PC:EC bulk liquid meniscus. b) Evolution of the O 1s binding energies of the main components as a function of applied voltage.

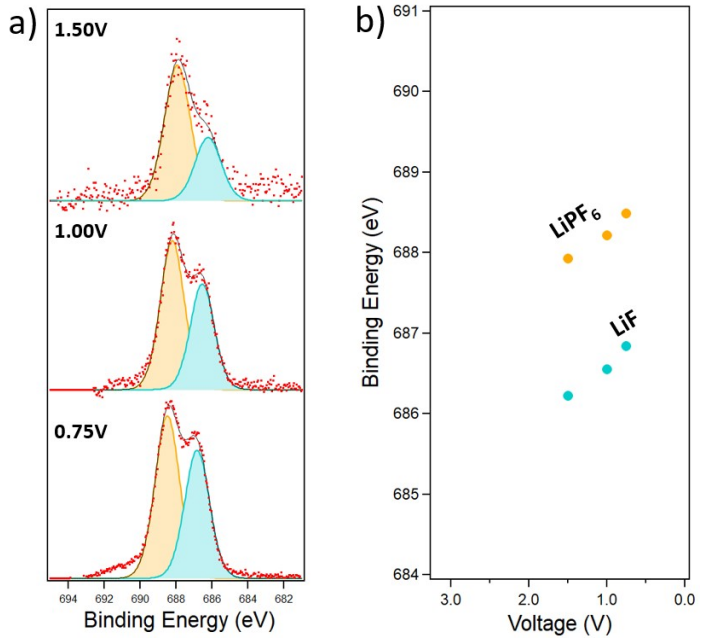


Figure 3.17: a) F 1s XPS spectra measured during discharge on the PC:EC bulk liquid meniscus. b) Evolution of the F 1s binding energies of the main components as a function of applied voltage.

case of pure PC solvent, three main chemical bonds are identified, and their BEs linearly shifts, as expected.

### 3.4.2 Results on the PC:EC || GC interphase

In the case of the interphase of PC:EC mixture, the measurements were performed in the same way as in section 3.3.1. Figure 3.18 shows the results obtained from the C 1s core level spectra. The typical asymmetric peak of glassy carbon can be observed at lower binding energies, followed by the $CH_x$ peak, the C-O, the inorganic carbonates, and the organic $CO_3$. Before focusing on the binding energy (BE) evolution, a qualitative comment on the intensity of the different components can be made in comparison to the PC case. The observation of the GC component indicates that the spectral information comes from the interphase. The evolution in BE of the different peaks shows a difference compared to the one seen previously: here, the behaviour of deposition detected for the inorganic carbonates species previously happens for also the other components, that show a decreas in the slope for voltages lower than 0.75 V.

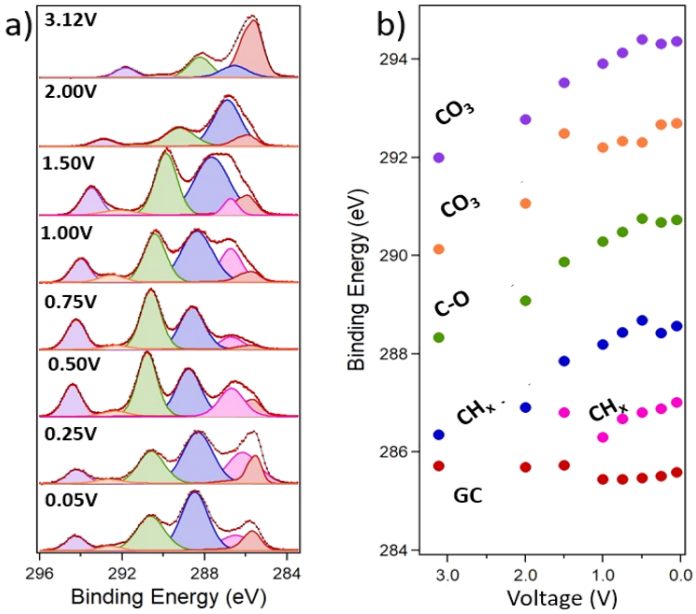


Figure 3.18: a) C 1s XPS spectra measured during discharge at the PC:EC||GC interphase. b) Evolution of the C 1s binding energies of the main components as a function of applied voltage.

The results of O 1s and F 1s core levels are shown in Figure 3.19 and Figure 3.20, respectively. The O 1s spectra show the same number of components with respect to the PC solvent case: The C-O and C=O peaks follow the novel behaviour of the species in C 1s

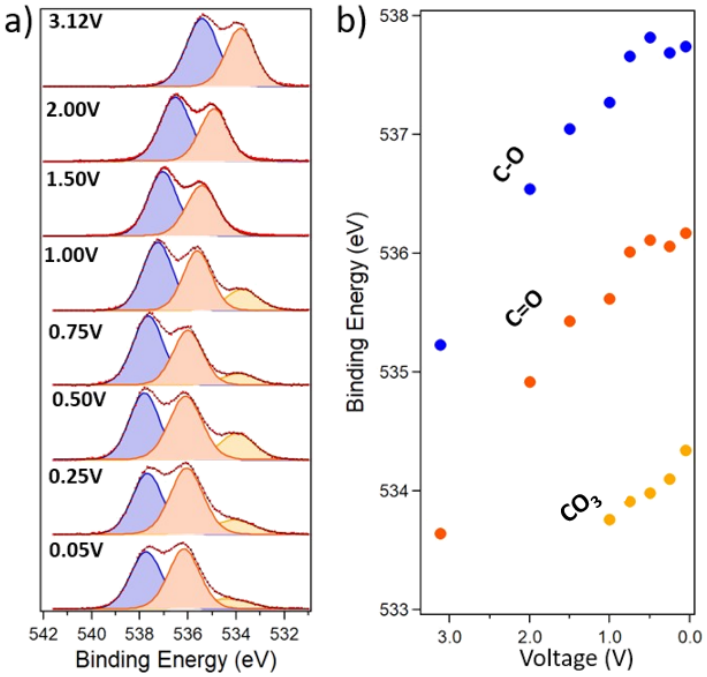


Figure 3.19: a) O 1s XPS spectra measured during discharge at the PC:EC||GC interphase. b) Evolution of the O 1s binding energies of the main components as a function of applied voltage.

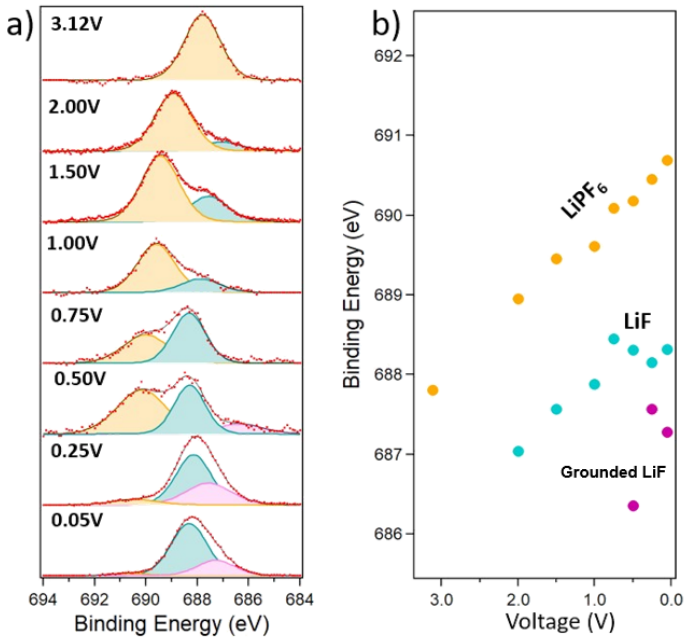


Figure 3.20: a) F 1s XPS spectra measured during discharge at the PC:EC||GC interphase. b) Evolution of the F 1s binding energies of the main components as a function of applied voltage.

for the BE, while the peak at lower energy, that appears at around 1 V (in opposition with the previous case where it is already seen at 2 V) seems to shift accordingly to the applied voltage. This could be because it is related to a different specie, coming from other degradation products. Looking at F 1s, at OCV, only the peak attributed to $LiPF_6$ is observed in the F 1s spectra. Above 2 V, another spectral component attributed to LiF (light blue peak in Figure 3.20) start to arise and it becomes dominant at low voltage. Moreover, a weak component (pink in Figure 3.20) appears below 1 V vs $Li^+$/Li, that could be assigned to a more grounded LiF component. To interpret these results, it is important to notice how it has previously been reported that EC can follow several pathways to reduce to different species, of which the most common is $CH_2OCO_2Li$. Considering this and other possible degradation products are indicated as to be less soluble than the PC-produced ones, the presence of a richer SEI forming on the surface could explain the behaviour of deposition detected for the other species.
Looking at the O 1s this is confirmed by the other peaks, which were originally shifting in the case of PC but deposit here. The behaviour of the $CO_3$ peak is then not explainable through the same way as done before. Its shifting trend and low intensity suggest that the main specie contributing to it is still dissolved in the electrolyte or, alternatively, deposited over a thicker layer of insulating SEI tht prevents its electrical contact to the electrode, conserving the shifting behaviour.

The behavior of LiF, showing a strong relative intensity and shifting during the discharge until low values of voltage, in contrast with the non-shifting, weak, LiF present in the PC sample and accordingly to the literature [117]. This could suggest that the insulating layer that forms at first may be of a mostly inorganic character, being mainly composed of F reduction products as LiF. This product grows then at voltages below 1 V vs $Li^+$/Li becoming the main F component that can be found at the interface. We can then detect two different signal coming from LiF, one for the components closer to the GC electrode, that remain at low BE, and another for the deposited LiF which is then insulated from the surface and shifts, being moreover on the outer layer of the SEI and thus contributing more

on the signal.

Taking this assumption as correct, we can confirm the formation of a thick insulating inorganic inner layer followed by an organic outer layer, as already reported by other techniques for EC based electrolytes.[78], [116].

## 3.5 The influence of VC additive

Further electrolyte formulation, 1M of $LiPF_6$ in PC with 3% VC was investigated, as the VC additive has been reported to impact the SEI formation [118]–[120]. In fact, VC improves the cycling capabilities of a Li-ion battery, reducing the usual solvent components and forming a stable SEI film. The SEI formed is reportedly rich in $Li_2CO_3$, also presenting polymers coming from VC reduction, and lithium vinylene dicarbonate $(CHOCO_2Li)_2$. Moreover, it presents a lower quantity of fluorinate species.

### 3.5.1 Results on the thick liquid meniscus

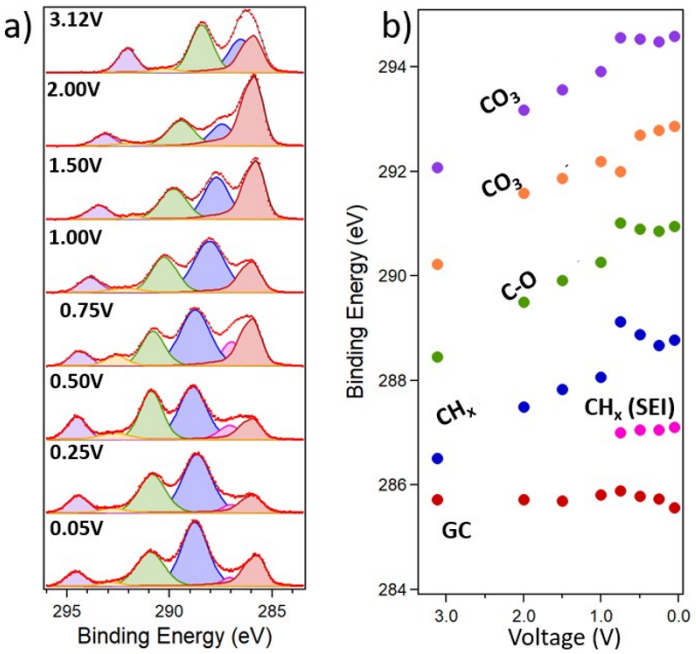


Figure 3.21: a) C 1s XPS spectra measured during discharge at the PC+VC thick liquid meniscus. b) Evolution of the C 1s binding energies of the main components as a function of applied voltage.

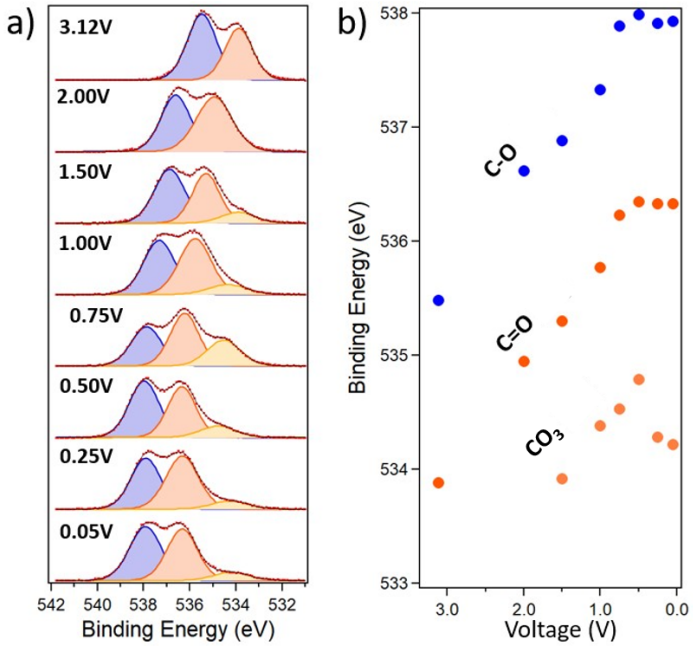


Figure 3.22: a) O 1s XPS spectra measured during discharge at the PC+VC thick liquid meniscus. b) Evolution of the O 1s binding energies of the main components as a function of applied voltage.

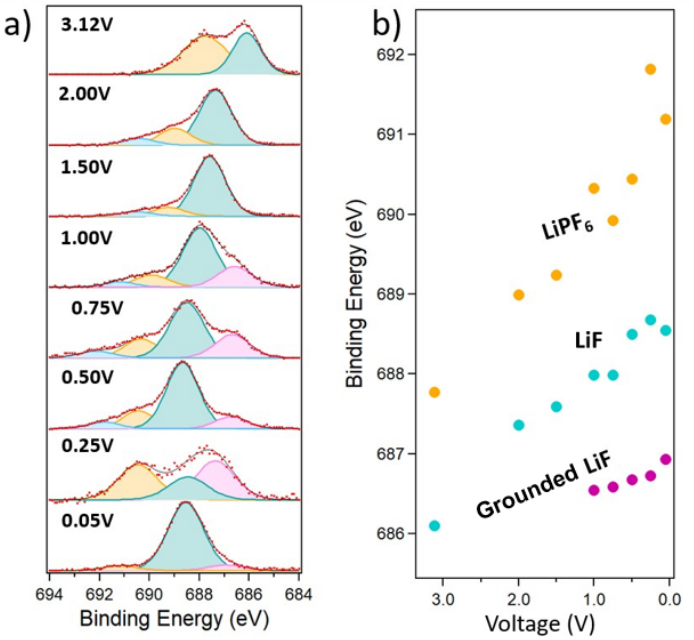


Figure 3.23: a) F 1s XPS spectra measured during discharge at the PC+VC thick liquid meniscus. b) Evolution of the F 1s binding energies of the main components as a function of applied voltage.

The results on the bulk PC solvent with 3%VC electrolyte are reported in Figures (3.21, 3.22, 3.23). The main species from the solvent can be recognised, similarly to previous

electrolyte formulation, with an overall linear shift over discharge. The points follow the expected linear shift aside from the ones in O 1s at 1.5 V, voltage where also the impurities peak at 1.5 V of C 1s in 3.24 shows a similar behaviour, being slightly outside the expected trend for a linear shift, contrarily to the other carbon species and the fluorine ones. The reason could be found in a difference in spatial positioning of the beam on the system for that voltage point. While the electrolyte was thick enough to not allow to see the substrate in the C 1s, it could be that the measure of 1.5 V was taken at a position where the thickness would allow access to an area closer to the substrate where the potential was different for some species.

### 3.5.2 Results on the PC+VC || GC interphase

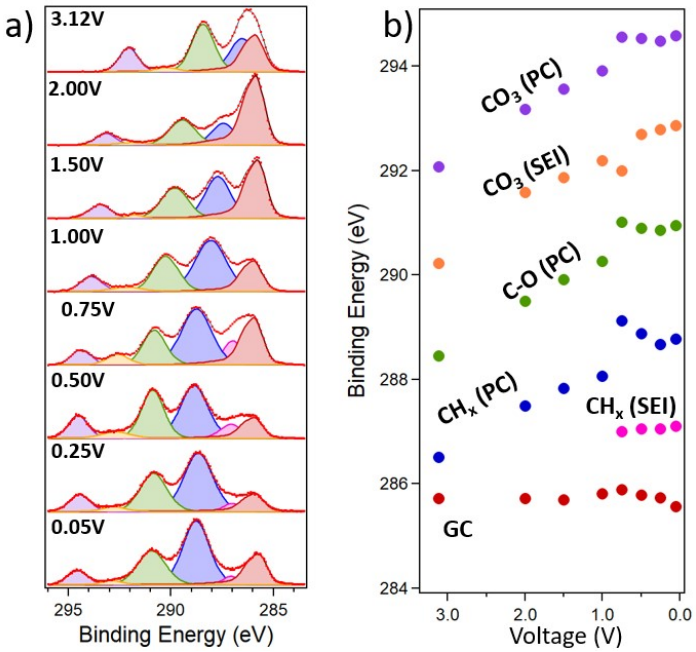


Figure 3.24: a) C 1s XPS spectra measured during discharge at the PC+VC||GC interphase. b) Evolution of the C 1s binding energies of the main components as a function of applied voltage.

The results of C 1s are shown in Figure 3.24. The carbon peaks exhibit the usual collection of components. The shift in binding energies stops for most of the species after reaching 1 V. In this case, a strong discontinuity can be observed on the $CO_3$ (purple), CO (green), and $CH_x$ (blue) peaks right at 1 V, where the said species see an increase in BE in op-

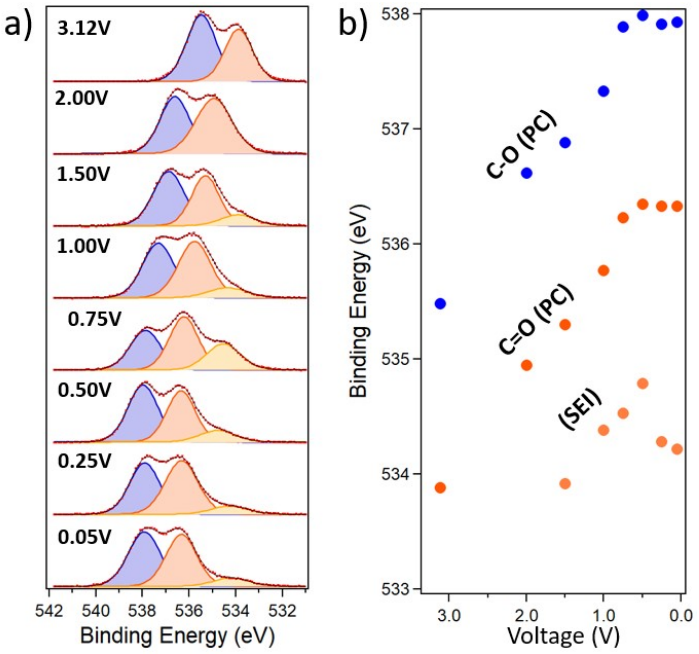


Figure 3.25: a) O 1s XPS spectra measured during discharge at the PC+VC||GC interphase. b) Evolution of the O 1s binding energies of the main components as a function of applied voltage.

position to the inorganic carbonates (orange) that instead have a drop in BE for that point. After this point, the species undergo a back shift that could be related to the deposition on the surface. This evolution could be due to the formation of the first layer made of polymers and dicarbonates, depositing on the surface of the electrode and thus not increasing anymore with Voltage. The behavior of the inorganic carbonates could be then explained as they may deposit after the formation of this first layer, remaining partly insulated from the electrode. The higher binding energies could be relative to the species present not in the solvent but in the polymers that are a result of VC, that showed higher binding energies also in previous studies [121]. That would however not explain the absence of the peaks related to the species in the solvent, since there is no significant change in the width of the peaks, and the volume of the electrolyte should be in any case much higher than the one of the VC reduction products.

We have similar results for the O 1s spectra in Figure 3.25: the linear shift of the species sees a change at 1 V for C-O (blue) and C=O (red), with a sudden increase in the BE that

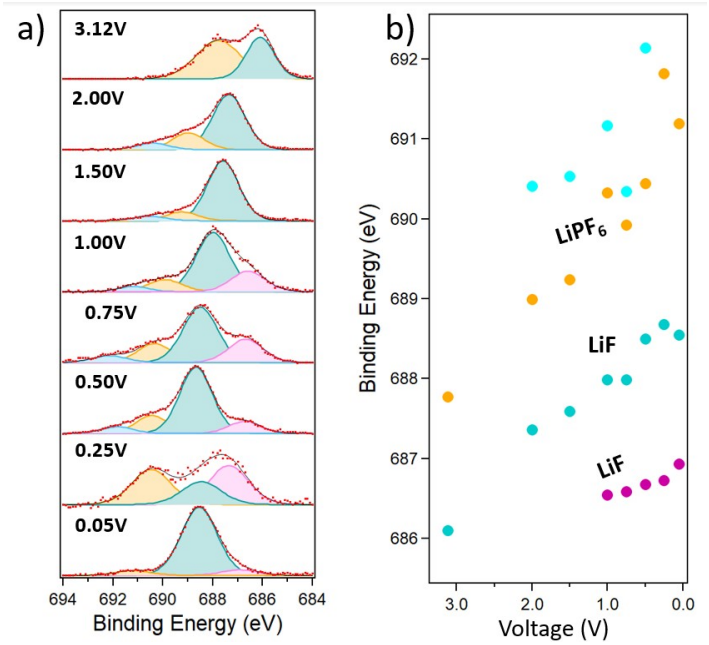


Figure 3.26: a) F 1s XPS spectra measured during discharge at the PC+VC||GC interphase. b) Evolution of the F 1s binding energies of the main components as a function of applied voltage.

then remains stable. Contrary to that, the inorganic $CO_3$ (orange) grows linearly until a drop in energies for the last two points.

Lastly, looking at the F 1s results in Figure 3.26, we notice two main peaks (orange and turquoise) and two additional peaks (light blue and pink). As already saw previously, the F 1s tends to be subject to charging effect issues probably due to the insulating nature of its components. This is probably the origin of the light blue peak that is seen below 2V, and an explanation of the imprecise trend for its BE and the one of the related orange peak, that can be instead assigned to the electrolyte salts. The turquoise peak and the pink peaks, considering their BEs, are to be ascribed to LiF that could be either deposited in direct contact with the surface (pink, no linear shift) or dissolved or anyhow not in contact with the glassy carbon (turquoise, presence of a linear shift).

## 3.6 Conclusion

Accessing the solid-liquid interphase of Li-ion batteries with *in situ* XPS has long been a major goal for battery research aiming to follow the formation of the SEI. The Dip & Pull approach proposed here has for the first time allowed to obtain a real-time observation of the SEI formation, thanks to the possibility to access to the interface and obtain the XPS signal of the GC substrate, the liquid electrolyte and the SEI forming in between, thanks to the possibility to probe through the thin electrolyte precursor film. From the evolution of the binding energies as a function of the applied voltage it was possible to identify the main SEI species and have an indirect access to their distance from the electrode surface. Varying the formulation of the electrolyte, and obtaining confirmations on the previous studies on these system through ex-situ studies, it was possible to validate the capabilities of NAP-XPS as a tool to investigate Li-ion batteries under different conditions.

# Chapter 4

# Development of a HAXPES electrochemical cell

The second approach chosen to investigate the buried SEI interphase in Li-ion batteries in *operando* conditions is based on Hard X-ray Photoelectron Spectroscopy (HAXPES). To that aim, we designed a new electrochemical cell dedicated to *in situ* *operando* hard X-ray photoelectron experiments in batteries materials. In this section, we will motivate and detail the cell design along with the preliminary results obtained at the GALAXIES beamline (SOLEIL Synchrotron).

## 4.1 Cell design

The tailored *in situ* cell has to fulfill several requirements to ensure its suitability for the battery materials research using HAXPES:

- Compatibility with UHV conditions
- Compatibility with omicron sample plate, to facilitate the transfer from the load-lock to the analysis chamber
- Window transparent to the incoming X-rays
- Thin window to allow escape of photoemitted electrons

- Chemical and electrochemical stability with the electrode and electrolytes
- Electrical insulating between the bottom/top part to avoid internal short-circuit

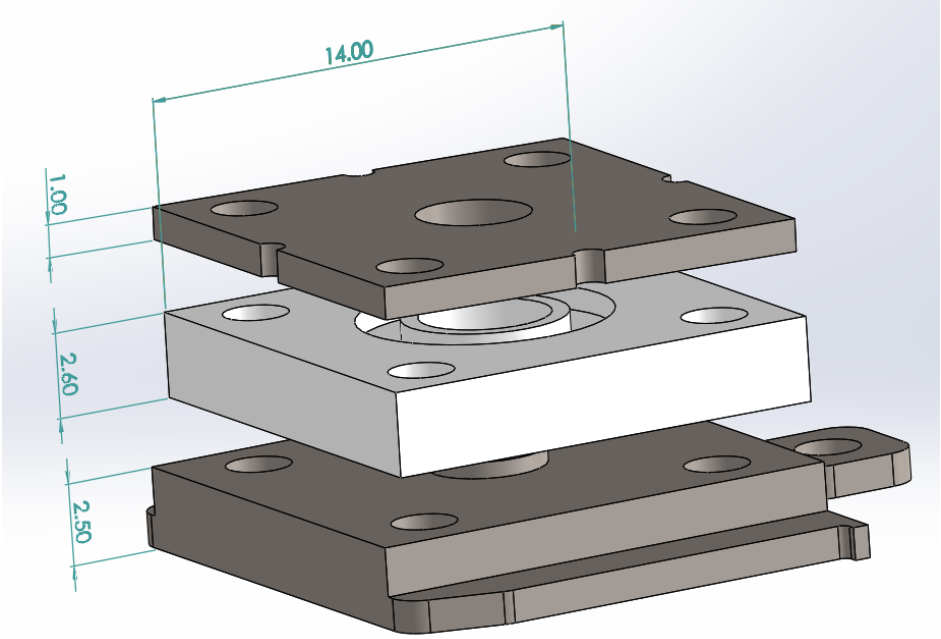


Figure 4.1: Sketch of the *in situ* electrochemical cell for *operando* HAXPES in LIBs.

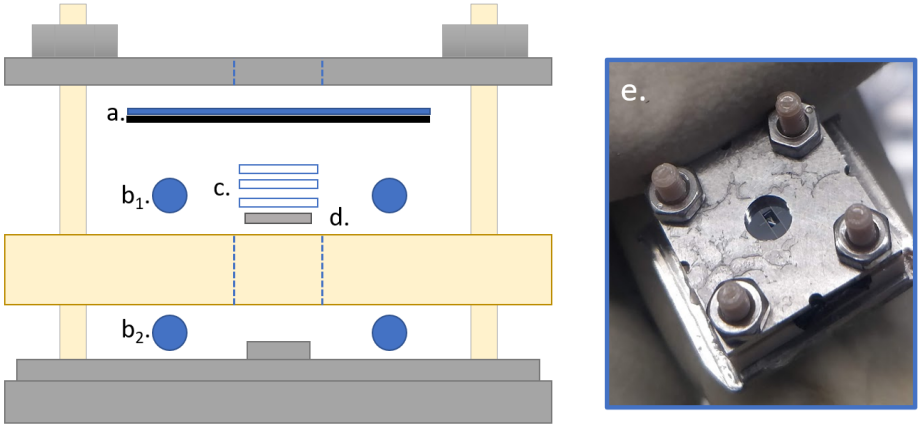


Figure 4.2: Lateral view of the cell showing the carbon coated $Si_3N_4$ chip (a), the O-rings (b1,b2), the glassy fiber separator (c), and the Li metal as anode (d). On the right panel, a picture of the cell inside the glovebox is shown (e).

The final design is shown in Figure 4.1. The bottom part is an adaptation of the omicron flag-type sample plate, with a central step and four holes for the screws. The middle part in white is made of PEEK, a material often used for electrochemical solutions due to its low chemical reactivity [122]. A groove has been included on both sides of this part to assure

a good vacuum compatibility. The top part is made of stainless steel. Four PEEK screws are used to close the cell while keeping the bottom and top parts electrically disconnected, avoiding discharge after assembling. The inner hole diameter is of 3.4 mm. The initial plan was to keep the whole design as close as possible to a standard 18 mm coin cell. However, there were some constraints: firstly, the area of the standard sample plate allows a diameter of up to 14 mm ; however, the whole structure of the cell also needed to be fitted in the 14 $mm^2$ space, and to avoid thin and breakable parts, each part of the cell had to have a thickness of at least 1 mm, especially when dealing with PEEK. Secondly, the groove for the O-rings in the PEEK middle piece also had some fixed dimension related to the sizes (inner radius and section) of the O-ring in use, that had to be matched with the remaining space available to avoid thin parts. The choice of a 3.4 mm inner cell diameter was then driven by all of these different requirements.

A schematic view of the section of the cell is shown in Figure 4.2. In the assembled cell, the electrolyte is soaking the *Whatman* separators (glass fiber), that act both as electrolyte reservoir and also as spacers, ensuring a good internal pressure. The bottom part acts both as a spacer and a way to align the middle PEEK part to the bottom part, while the top part has four dents in the middle of each side to centre the chip with the central hole of the top part. The aperture of the central hole is made to keep the maximum incidence angle possible for incoming X-rays while having the smallest possible central hole. This was done to ensure that there was no risk of bending the cell components to ensure its integrity over time. It also depends on the membrane sizes. About the membranes, four main parameters can be identified in relation to the accessible measuring angle $\beta$:

- $H$, the chip thickness
- $h$, the membrane thickness
- $L$, the membrane main dimension
- $\alpha$, the etching angle between the membrane and chip (fixed due to the etching angle

of crystal plane of the material)

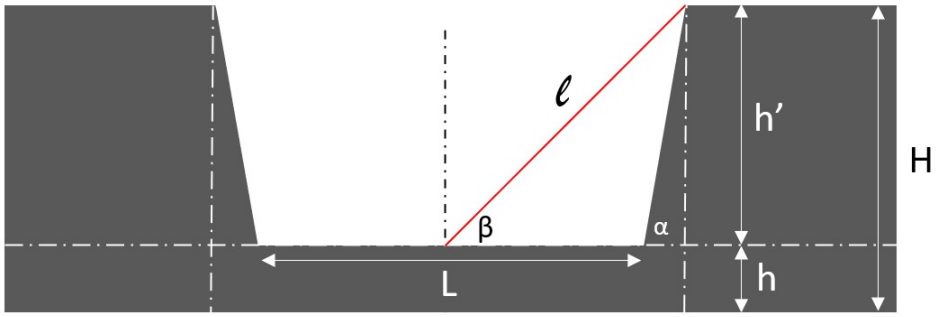


Figure 4.3: Geometric scheme used to estimate the incidence angle $\beta$ for the chip design.

Starting with these parameters (cf. Figure 4.3), it is possible to calculate the minimum incidence angle $\beta$ for each chip design by the following equation :

$$\beta = \arcsin\left(\frac{h'}{\ell}\right) \tag{4.1}$$

with,

$$\ell = \sqrt{\left(\frac{L}{2} + h' \cot\alpha\right)^2 + h'^2} \tag{4.2}$$

$$h' = H - h \tag{4.3}$$

Finally, during the cell assembling, a small metallic strip (copper or indium) was positioned in contact to the inner part of the chip and the outer metallic part of the cell (top part), thus ensuring a good current collection, since $Si_3N_4$ is an electronic insulator. While being in contact with the inner part of the chip, the strip was outside of the O-ring and did not take part to the electrochemistry or hinder the vacuum tightness of the cell.
The final, key part of the cell is the electron transparent membrane which is placed between the top part and the PEEK middle part. It serves to separate the inner part of the cell from the outside while permitting the photoelectrons to go out. The membranes thickness had a major role on the feasibility of this measurements. The prices of specially tailored chips and the time associated to their production asked however for a certain degree of reliability on the concept before actually trying experimentally the feasibility of each design. Simu-

lations played an important role as to validate the membrane thickness and the whole cell assembling.

### 4.1.1 SESSA simulations

To optimize the experimental parameters such as the membrane thickness and incident photon energy, we performed calculations of the photoelectric cross section using the SESSA (Simulation of Electron Spectra for Surface Analysis) software from NIST (National Institute of Standards and Technology). SESSA was used to simulate the photoemission spectra on an absolute intensity scale, based on a 2D model of the system (layer thicknesses, compositions, density, morphology) and the experimental geometry. The calculations rely on a series of databases of physical data from the NIST [123] and an efficient Monte-Carlo algorithm.

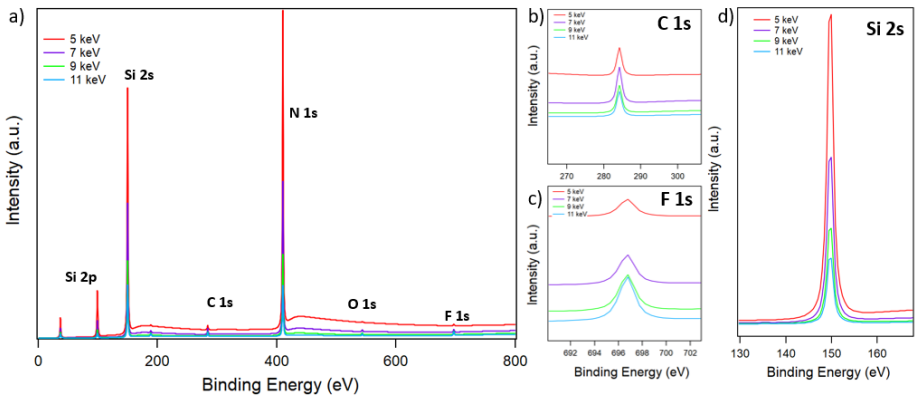


Figure 4.4: a) Survey simulation of our system composed of $LiPF_6$ electrolyte in EC+EMC under 5 nm of amorphous carbon and 20 nm of $Si_3N_4$, at different photon energies ; b)–d) close up of three main core peaks.

We simulated four different geometries and thicknesses to confirm the feasibility of our setup. Figure 4.4 shows the results of a simulation. The model was composed of a substrate made of fluorine, phosphorus, oxygen, carbon, and lithium at the bottom representing the battery system of 1M $LiPF_6$ in EC + EMC covered by 6 nm of carbon, representing the amorphous carbon layer deposited and used as anode, and 20 nm of $Si_3N_4$, the membrane, as depicted in Figure 4.5.

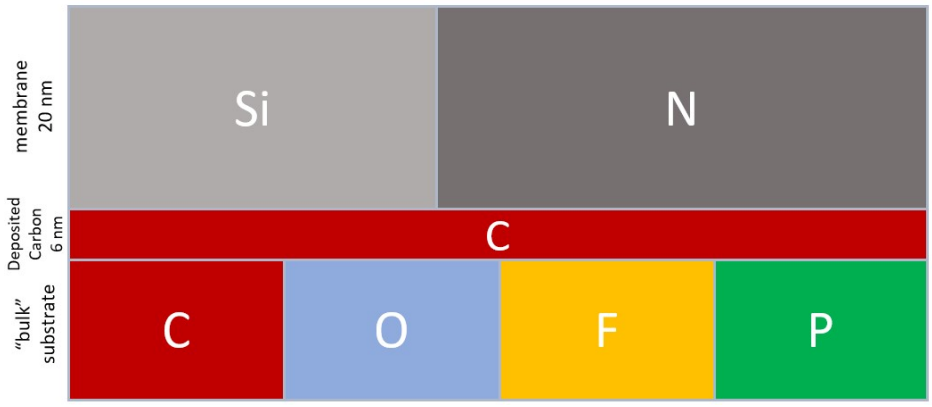


Figure 4.5: Model used for the SESSA simulations.

The simulations were performed by varying the photon energies (Figure 4.4). They demonstrate a clear trade-off - as far as the electrochemical system is concerned - between the gain from the increasing escape depth and the decrease of the cross section as the photon energy increases. Obviously, this does not apply to the Si 2s signal (Figure 4.4d) coming from the surface whose intensity merely decreases as a function of the incident photon energy due to cross-section change. This simulation confirmed that while the signal of Si and N is orders of magnitude stronger than the substrate contribution, the latter, including F 1s, O 1s, and C 1s, is clearly visible through the membrane, theoretically validating our choice for chips and membranes thicknesses.

## 4.2 Chips and membranes

Once the main design of the cell was decided, we focused on the choice of chip, membrane, and substrate. Different designs have been tried to this end, and they will be presented here to allow a complete understanding of the limitations and possibilities of this cell. We opted for $Si_3N_4$ silicon nitride membrane due to its transparency to X-rays and high mechanical stability, permitting it to withstand the pressure difference between the cell inside ($\sim$ 1 bar) and outside ($\sim 10^{-8}$ mbar) even with low thicknesses. Its common use as a membrane material ensured a high degree of freedom in the manufacturing and wide availability.

### 4.2.1 Sputtered carbon on 30 µm-thick $Si_3N_4$ commercial chip

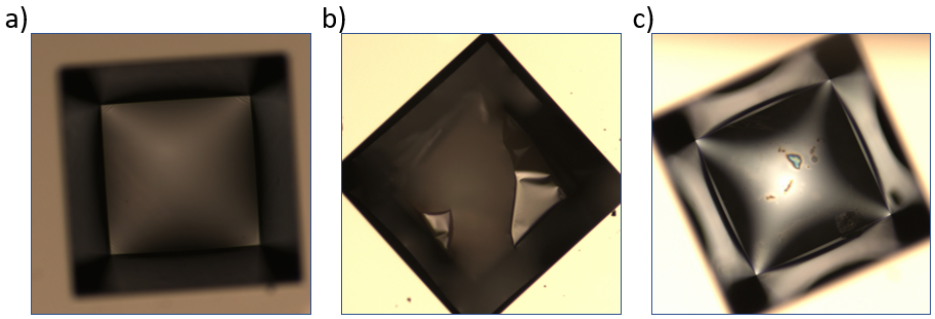


Figure 4.6: a) Pristine membrane before assembling; b) broken membrane after rough pumping from 1 bar to $10^{-3}$ mbar; c) intact membrane after slow pumping from 1 bar to $10^{-3}$ mbar.

A first attempt was made with commercially available $Si_3N_4$ chips with membranes provided by SILSON®, each with a small $50 \times 50\ \mu m^2$ membrane area and a thickness of $30\ nm$. Special tailored membranes were then ordered from them, but due to problems in the manufacturing process, they were not ready for the first beamtime, and we had to turn to commercially available ones instead. The objective was then twofold: first, to check the feasibility with these chips; second, to familiarize with the setup for the future beamtimes.

To have an inner carbonaceous anode, the membranes were covered with a thin amorphous carbon layer. The carbon layer deposition was performed by sputtering at $10^{-6}\ mbar$ in a specialized chamber for the preparation of TEM samples at LPS (Orsay). Thanks to a quartz microbalance in the deposition setup, it was possible to achieve control of the layer's thickness with an accuracy of $\pm 5\ nm$.

However, the pumping procedure was not optimized for the insertion of the cell at UHV, and several membranes were broken. In Figure 4.6, we can see the pristine membrane (a) and the two possible results of pumping to UHV: a broken membrane (b) and an intact one (c); the difference lies in the first moments of pumping. When the vacuum pumps are turned on, the first difference in pressure applied creates a strong mechanical stress on the membrane that breaks it. This was solved through the addition of a valve between the pump and the transfer chamber, allowing for further control of the pumping speed. Going slowly

from ambient pressure to around $10^{-3}\ mbar$, and thus taking around half an hour instead of the usual few minutes, allowed preserving the membrane intact. After the first three orders of magnitude, the actual difference in pressure from $10^{-3}\ mbar$ to $10^{-7}\ mbar$ was low enough to allow pumping at full speed. After managing to insert an intact membrane it was finally noticed a problem in the inner connection of the sample parking, that did not allow to apply potentials during this first test.

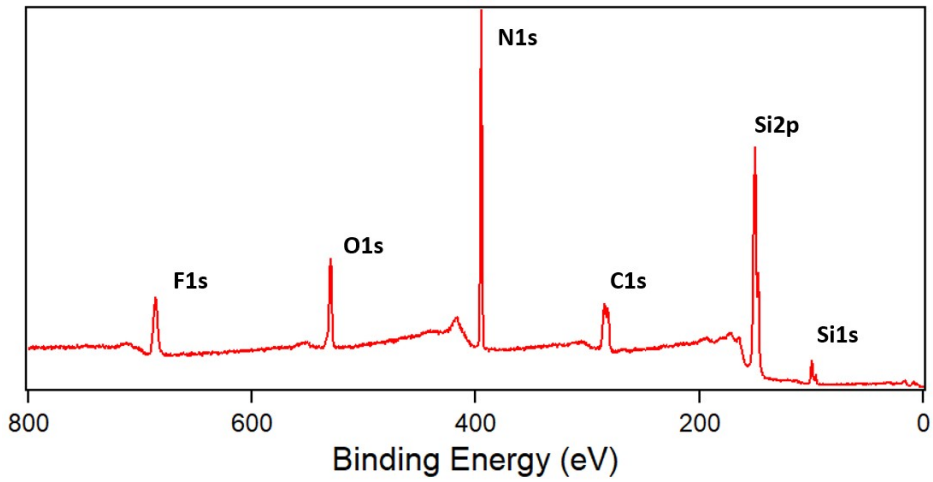


Figure 4.7: XPS survey of a coated 30 nm-thick $Si_3N_4$ membrane at $h\nu = 6.9$ keV (broken membrane).

Regarding the HAXPES measurements, the low success rate of insertion of these membranes did not produce satisfying results : in fact, a first part of the membranes were lost during the assembling process due to the inexperience in managing them in the glovebox together with the cell, while the membranes assembled without problems were lost during the process of fine tuning the pumping parameters not to break them. One of the membranes that was well assembled, shown after assembling in figure 4.6(c), was inserted and pumped, but it was not possible to measure it due to a problem with the beam. Another membrane, well assembled, was inserted with the same procedure and produced the survey spectra shown in figure 4.7. Seeing the F 1s and O 1s levels unexpectedly high, the cell was extracted and under the microscope it was seen that the membrane was in fact damaged by the pumping. In short, while this first test showed us that it was possible to insert the membranes under UHV, a satisfying result on the HAXPES measurement was not reached.

During another beamtime, another coated membrane was measured. The results shown in figure 4.8 present a very different intensity for the F 1s peak compared to the broken membrane and simulations. Despite these indicating the feasibility when using the nominal thickness of the $Si_3N_4$ membrane and of the inner deposited carbon layer, an additional thickness coming from carbon contamination on the membrane impeded full access to the interface. This made species coming only from the inner part of the system, such as fluorine, measurable only with very long acquisition time. Furthermore, the carbon signal coming from below the interface was too low compared to the C amorphous deposited layer and carbon contamination, making it difficult to measure. This limitation posed a risk of losing a significant information from the interfacial C 1s signal which holds considerable importance for interpreting the entire system as demonstrated with the Dip & Pull method.

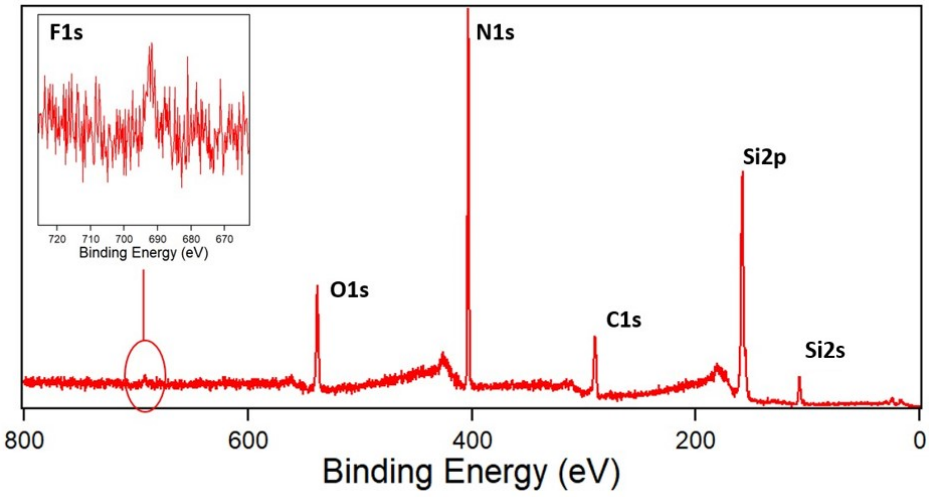


Figure 4.8: XPS survey of a coated 30 nm-thick $Si_3N_4$ membrane at $h\nu = 6.9$ keV (broken membrane).

### 4.2.2 Bilayer graphene on hole pattern $Si_3N_4$ chip

The membrane design chosen for the experiment was based on a previous result obtained in the catalysis field [124]. In this case, a thin bilayer graphene (BLG) was used both as a window – separating the vacuum environment of XPS from the liquid catalysis components – and an actual substrate for catalysis. Similarly, this approach applied a "thick" membrane ($200\ nm$, much larger than the probing capacities of HAXPES) with an array of $1\ \mu m$ diam-

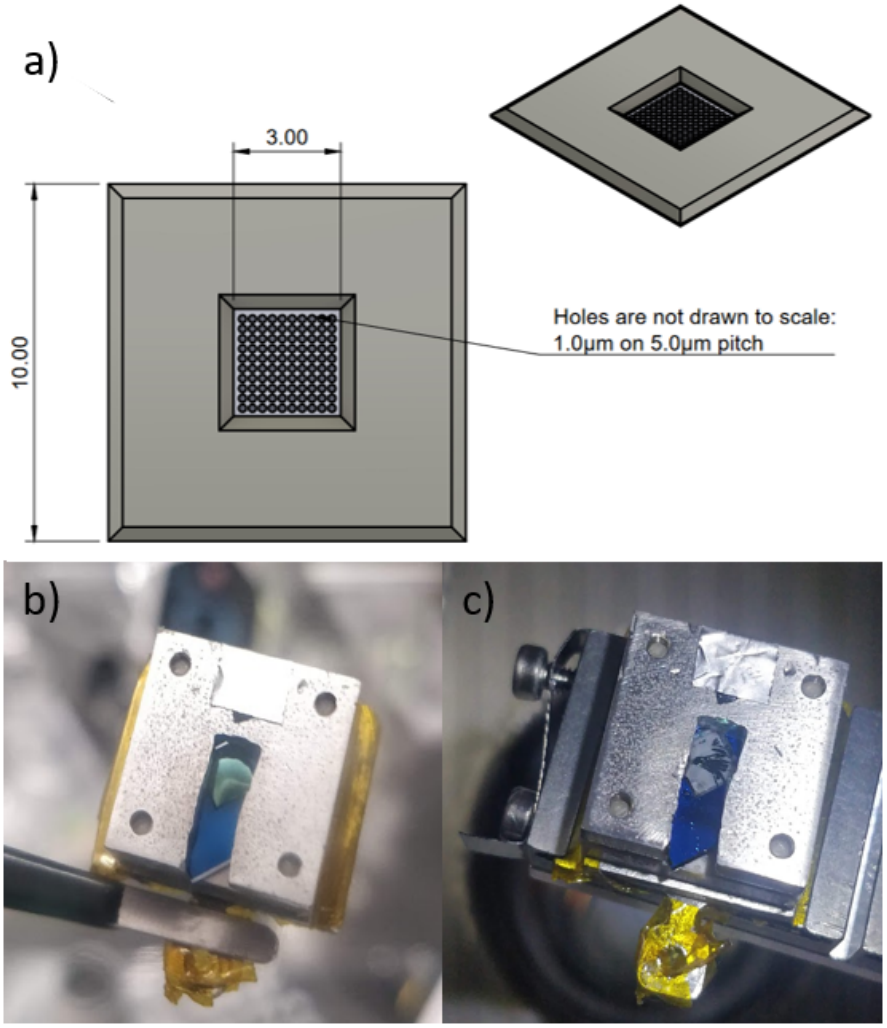


Figure 4.9: a) Schematic drawing of the BLG chip (top view); b) successfully assembled cell c) cell busted after pumping.

eter holes, as schematized in Figure 4.9a). On the inner side, the BLG would work both as a carbon-based anode and as an atom-thin window, "closing" the holes on the membrane, resistant enough to withstand the pressure difference and thin enough to permit photo-electrons from the interface to escape. To ease the detection through the membrane at an incident angle of $10°$, the size of the membrane was chosen to be $3 \times 3\ mm^2$, which was the maximum size to hold the pressure difference according to the specifications.

### Electrochemical response

This first prototype of the chip gave us an initial good confirmation of the electrochemical capabilities of the cell, as shown in Figure 4.10, where a cyclic voltammetry was performed on the cell assembled with the BLG chip in a continuous scan and in the stepped way, as already performed for the dip & pull experiment. Problems arose, however, since the fragility of the membrane to shear mechanical stress caused by any kind of lateral shift of the pieces of the cell during the assembling would cause a breakage of the membrane or a crack that would then break during pumping. In figure 4.9 b) and c) it can be seen the clear difference between an intact and a broken membrane after assembling.

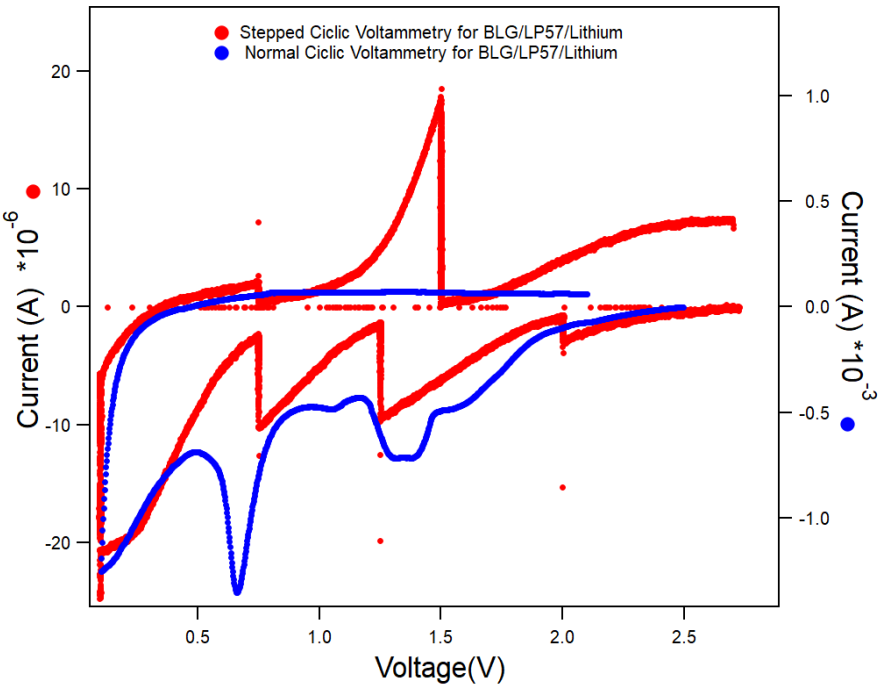


Figure 4.10: Cyclic voltammetry using the *in situ* cell with the BLG chip: in red the voltage step procedure, in blue the standard CV.

### HAXPES results

Among several chips used, only one performed correctly. It was possible to access the inner part of the cell and measure the electrolyte species at $6.9\ keV$, in good accordance with the simulations performed at $7\ keV$ as shown in the survey (Figure 4.11). However, problems

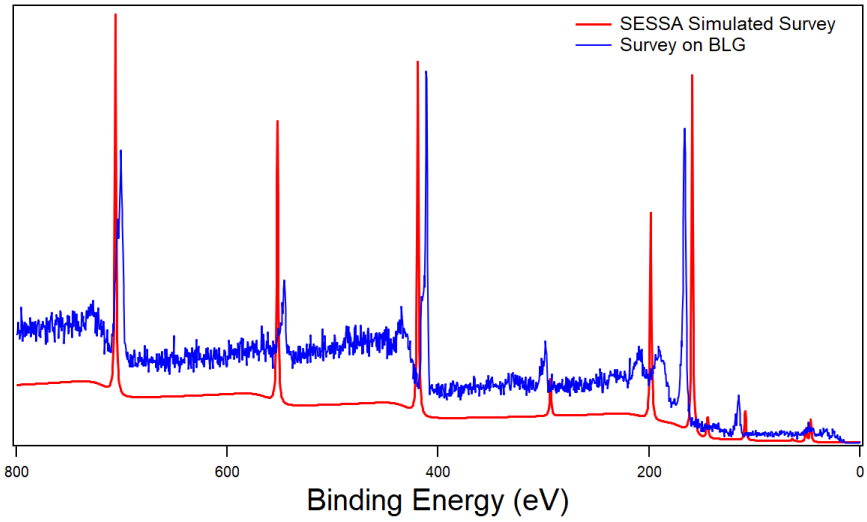


Figure 4.11: XPS survey obtained on the BLG cell (blue) along with the simulated spectrum (red).

with the cabling prevented us from realizing a full electrochemical experiment: already from the survey, it is possible to see how the core peaks show low intensity and shifted binding energy, even though the measurement was taken at OCV with no voltage applied. When applying voltage, we observed a shift (of about $2\ eV$) of the core-level peaks of C 1s and F 1s as shown in figure 4.12, in agreement with the applied voltage. However, the overall peak shape appeared exceedingly large with a width $> 10\ eV$ that does not hold any physical meaning. We believe this shape is due to a charging effect related to cabling issues.

### 4.2.3 Sputtered carbon on home-made $Si_3N_4$ chip

The uncontrollable layer of adventitious carbon on the surface and the error on the thickness of the inner deposited carbon of the first chips showed the need to get a thin membrane to access the interface, while the fragility of the wide windows of the BLG chips made clear that it was important to reduce as much as possible the membrane area. A new chip design was then made together with the group of Jordi Fraxedas and Frances Perez Murano of the IC2N of Barcelona: the chip was the usual $Si_3N_4$ chip of $10 \times 10\ mm^2$ and $0.5\ mm$ thickness, with a $50 \times 500\ \mu m^2$ membrane of $15$ or $20\ nm$ thickness. For these new membranes, a first

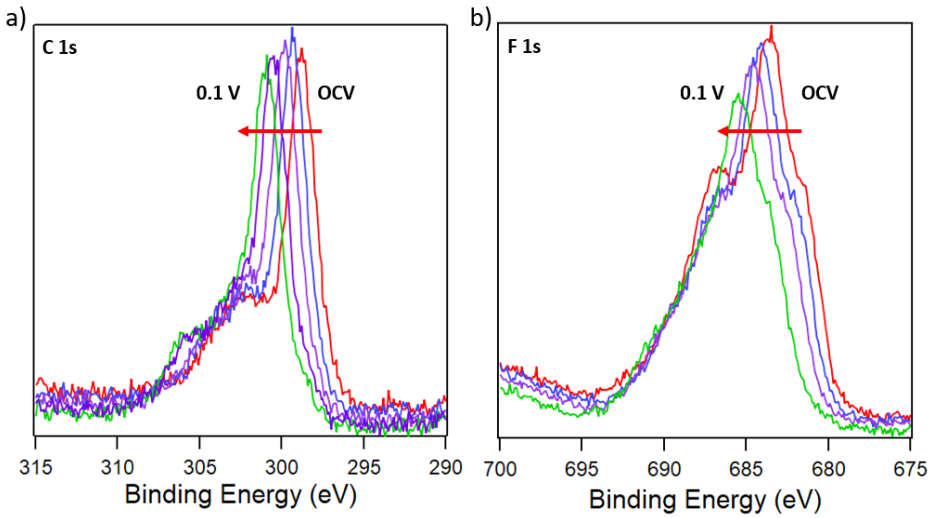


Figure 4.12: HAXPES C 1s (a) and F 1s (b) core levels collected at $h\nu = 6.9$ keV upon discharge.

set was covered with sputtered carbon and a second one with a multilayer of graphene. The carbon thickness was kept around $5$ to $10$ $nm$, while for the graphene multilayer, $5$ sheets were used, with a thickness that can be estimated at around 15 $\mathring{A}$ [125]. The rectangular shape of the membrane was chosen to allow a full exposure of the membrane to the beam while maintaining good mechanical resistance to the difference in pressure, compared to a square one. Moreover, two Pt patterns were etched on the outer side of the chip in correspondence of the membrane to allow easy positioning of the beam on the sample. The design of the chip can be seen in Figure 4.13.

### Electrochemical response

The electrochemical response of these chips, both in the graphene or in the sputtered carbon solutions, showed the need of the addition of an inner current collector grid to the design. In figure 4.14 it is clearly shown how, while it was possible to apply the usual electrochemical procedure, the signal was very noisy for both voltage and current reading. This issue was less prominent in the chips with thicker carbon coatings, that presented however the problems for accessing to the interface.

The inner conductivity of a thin scattered amorphous carbon layer, deposited on an

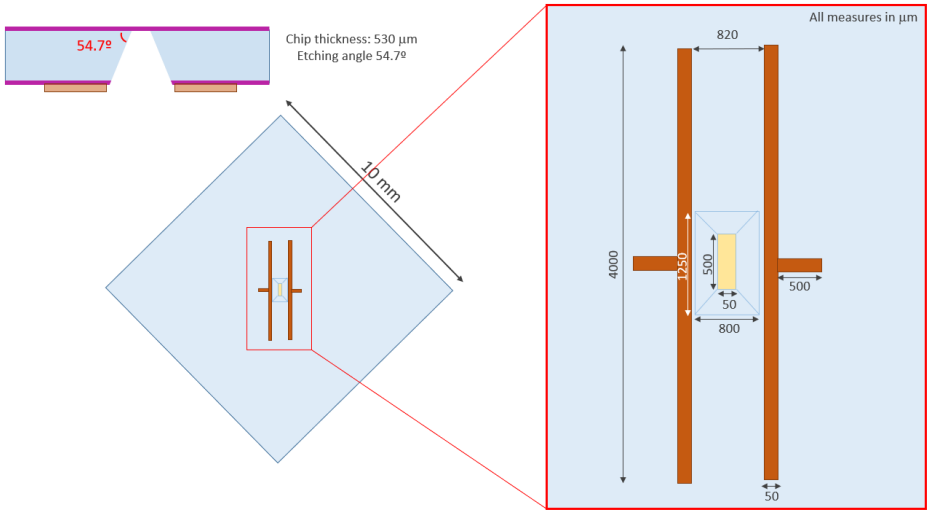


Figure 4.13: chip structure and sizes. In blue, $Si_3N_4$, in dark orange Pt, in light orange the membrane.

insulating substrate as is $Si_3N_4$, is too low for the electrochemical needs of this kind of experiment. We believe however that this can be solved through the etching of an inner grid of conductive material that would work as a current collector.

### HAXPES results

To confirm that the new membranes were vacuum compatible and allowed measurement through them, a first measurement was made on three different cell configurations: a first cell was assembled with the membranes in an open environment so that the atmosphere would get inside the cell. A second one was closed without tightening to pump vacuum inside and be able to measure only the membrane signal with nothing below. Lastly, a third cell was assembled as the first one but with the addition of the deposited carbon layer on the inner side of the membrane. The results are shown in Figure 4.15: in (a) the nitrogen 1s peak is shown; in the red and green spectra, we can clearly see the strong peak coming from the nitrogen of the membrane (lower energies) and the weaker one coming from the $N_2$ gas present in the air under the membrane (higher energies). The absence of such a peak in the empty cell (blue) confirms it is coming from the air inside the cell and through the carbon layer. In (b) the same applies to oxygen with the addition of a wider peak for the

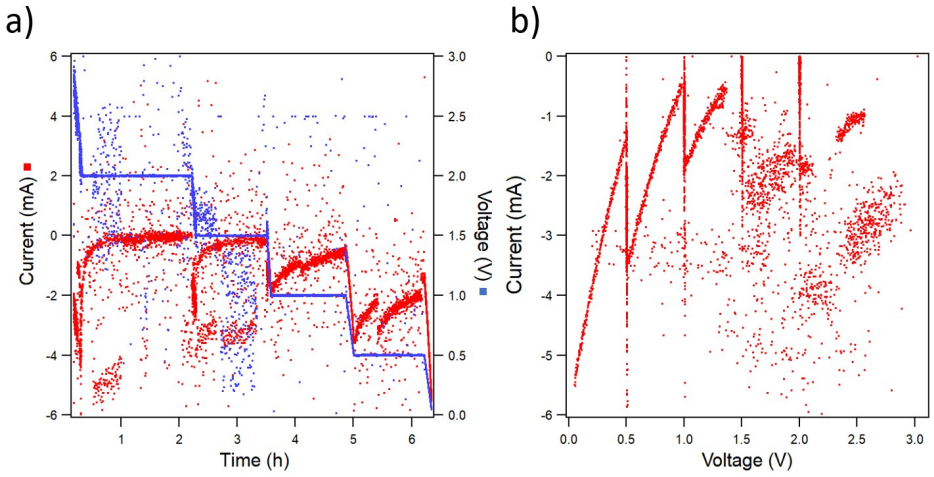


Figure 4.14: Elecrochemical Procedure for the homemade sputtered chip. In (a), the stepped applied voltage as a function of time and the related current flowing. In (b) the resulting CV curve.

green line since there are also the oxidized carbon signatures. We then moved to measure the assembled cells.

The first set with sputtered carbon showed a mix of different results. The membranes resisted well to the pumping process and were always inserted in UHV without problems. The $15\ nm$ membranes allowed reaching the interface, but all $15\ nm$ membranes broke during the measurements after the voltage was applied. This happened while taking the spectra for the second point in voltage starting from OCV when reaching $2\ V$ and in our opinion was probably due to a build-up of gas species inside the cell during discharge due to the start of reduction of electrolyte species on the surface of the anode and the consequential rise in local pressure. Figure 4.16 shows the survey measured on a 15 nm thick membrane at $8.0\ keV$: the main peaks of interest for us (C 1s, F 1s, and O 1s) showed a good intensity that allowed us to then proceed to the measurement. The peaks were measured firstly at OCV, and the results are shown in Figure 4.17without showing the effect seen previously with bad cabling that brought charging effect problems. In (a), the carbon 1s shows several different components: from lower to higher binding energy, we can see the C-C/C-H, the C-O, and then at higher energies $CO_3$. While there are many components in the first group

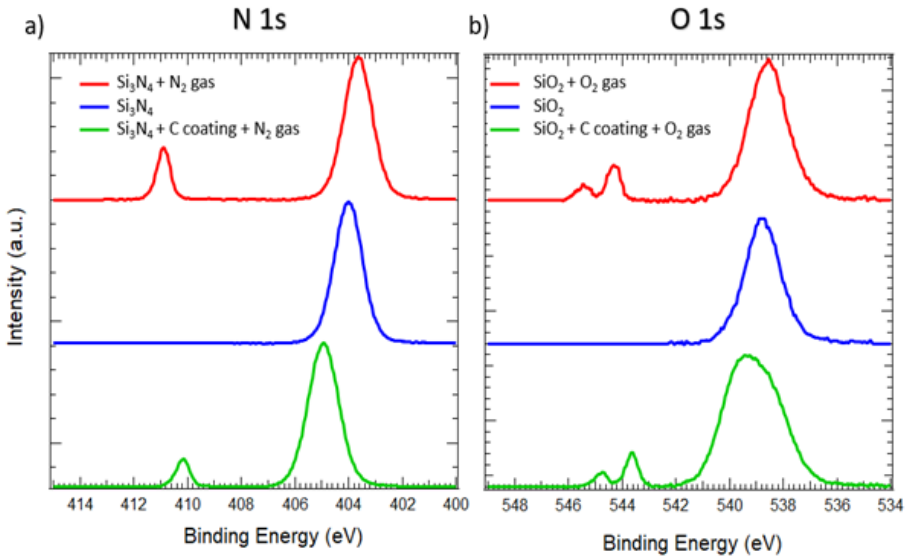


Figure 4.15: Measurement of N 1s (a) and O 1s (b) gas phases through the membrane (red) and through the carbon coated membrane (green) compared to an empty cell.

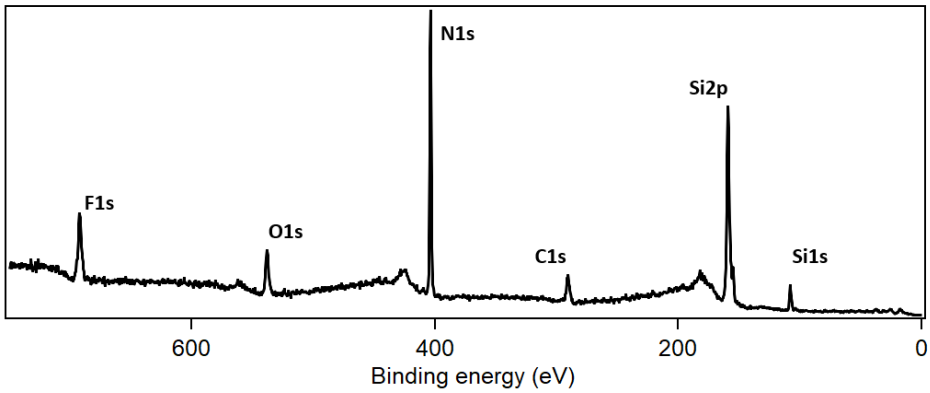


Figure 4.16: Survey spectra of an electrolyte filled cell with a 15 nm membrane

of peaks that can be attributed to the presence of carbon and oxidized carbon both at the inner and outer side of the membrane, such $CO_3$ peak can only come from the electrolyte solvent and is a clear signal of our ability to successfully probe for carbon species below the membrane. Then O 1s is also well seen, in agreement with the fact that we have oxidized species on the surface of the membrane as well as all the oxygen groups coming from below it. This is also the reason why the interpretation of O 1s could prove to be difficult. At last, fluorine 1s has also been detected with a double component that seems to be related to the fluorine salts dissolved in the electrolyte and the presence of LiF. Considering that this was at OCV, this presence could be due to a short circuit in the cell happened during

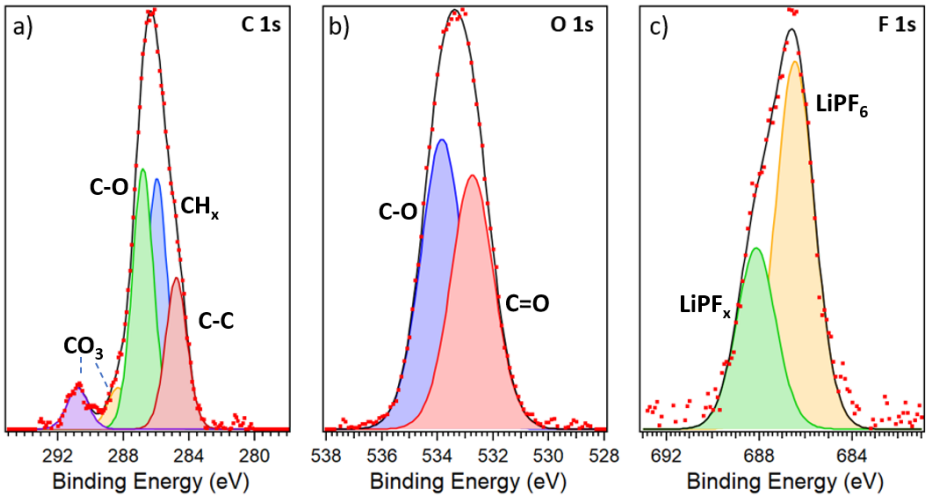


Figure 4.17: Main core peaks (C 1s, O 1s, F 1s) coming from the electrolyte below the membrane. OCV at $h\nu = 8$ keV

either the assembling or the transferring since we do not expect to have LiF at OCV before any electrochemistry start ina fresh cell. While these core peaks were encouraging results for our system, it was not possible to perform operando measurement. The problems that arose during this beamtime can be summarized in three main points that, while reasonably easy to solve with preparation, did not allow obtaining results when the limited time and membrane available are taken into account.

First of all, during this beamtime, the cabling problem that affected the previously shown data was finally addressed and solved. However, two main issues related to the carbon coating remained: first of all, the poor control of the carbon coating thickness produced mixed results, where the $CO_3$ peak from the solvents was not always measurable. Secondly, while a thin carbon coating allowed good measurements like in the case of Figure 4.17, it also meant that there was a poor conductivity on the inner side of the cell as discussed in section 4.2.3. Not being able to collect the current well enough, it was not possible to perform proper electrochemical procedures on the sample. As such, when the carbon layer was thin enough to allow access to the interface, it was not possible to perform the electrochemical part, while when the electrochemical part was good enough, that would mean that the inner layer was too thick to access the interface. Indeed the carbon

sputtering technique did not allow for reproducible results: in fact, depending on the thickness of the layer (that, as mentioned, had a controllable error of around $5\ nm$), the carbon layer would be either too thick to access the interface or too thin to allow good current conductance between the inner layer and the outer current collector.

It was then decided to try to address the thickness reproducibility problem using a multilayer graphene stack. The thickness of the inner carbon layer is both well controlled and thin enough to ensure a good signal from below the anode thanks to good control of the carbon layer. This approach showed, however, two main problems: firstly, the deposition process for graphene was not optimized for the thin membranes : Out of $10$ membranes just one did not break during deposition. Secondly, the multilayer graphene did not exhibit sufficient conductivity without the support of a current collector, and thus the electrical contact between the inner and outer side of the chip was not sufficient. Since the membranes themselves showed good results, minor changes could bring forth a successful experiment: more specifically, an inner grid of conductive material on the chip, etched with the same procedure used for the platinum strips, could ensure good current collection, while mastering the process of deposition of the multi-layered graphene on the chips would ensure obtaining chips with intact membranes and an inner thin, fixed, carbon anode.

## 4.3 Conclusion

The development of the *operando* cell for the GALAXIES beamline has provided initial promising results, demonstrating the feasibility of the project. But a fully functional electrochemical cell remains to be achieved. Specifically, the electrical contacting and current collection have to be improved along with a more robust and reliable assembling process of the cell. Despite these challenges, the cell has already been used by other research groups exploring liquid systems at GALAXIES, holding strong promise for future advancements.

# Chapter 5

# Conclusions and Perspectives

A properly functioning lithium-ion battery relies on the formation of a stable solid-electrolyte interphase (SEI) on the negative electrode's surface. The SEI plays a vital role in maintaining normal battery operation: it widens the electrochemical stability range of typical organic electrolytes, making them compatible with the very low negative electrode's electrochemical potential. Without the SEI, the solvents and salts of the electrolyte would undergo continuous reduction on the negative electrode's surface. The SEI is formed through the deposition of degradation products from the electrolyte on the electrode's surface on the first cycles, creating a nm-thick mosaic-like passivation layer. This film ensures good ionic conductivity, allowing proper diffusion/migration of $Li^+$ ions, while also being electronically insulating. This insulating property prevents further electron exchange at the electrode/electrolyte interface, avoiding continuous electrolyte decomposition. Consequently, the SEI acts as a spontaneous self-healing mechanism.

To understand the composition, morphology and associated formation mechanisms of the thin SEI surface film several techniques as been employed (see the Introduction 1.2.3). Among them, XPS occupies a prominent place due to its probing depth of a few nanometers and its sensitivity to the chemical composition, oxidation states and chemical environments of probed elements. However, this surface sensitivity requires removing the electrolyte from the electrode's surface by rinsing it with pure solvent to avoid salt precipitation at the surface, prior to drying the electrode and transferring it to vacuum. This ex situ preparation

method is widely used in the battery community; however, such experimental conditions are quite far from the actual conditions existing in a battery during its operation, where the electrodes are constantly in contact with the electrolyte.
To overcome this issue, we have developed two innovative approaches based on XPS, enabling spectra collection on the SEI during battery functioning, and thus providing a direct observation of the SEI formation.

The NAP-PES combined with the Dip & Pull setup has been employed to study the influence of the SEI formation on the first cycle as a function of the electrolyte formulation, either changing the solvents (adding EC) or using an additive (3% VC). For this study, a carbonaceous glassy carbon electrode was used as the electrode working as a substrate, against metallic lithium in an half cell configuration, and 1 M $LiPF_6$ in PC as electrolyte.
We were able to localize the thin electrolyte precursor film, which enables the simultaneous detection of the XPS signals from the glassy carbon electrode, the electrolyte and the SEI. The novelty of this study lies in the real-time observation of the SEI formation, enabled by operando NAP-PES, allowing for the identification of the main SEI species and giving an indirect access to their location in space (i.e. their distance to the electrode's surface) by following their binding energy shift as a function of the applied potential. Our results confirm the formation of inorganic carbonates like $Li_2CO_3$, lithium alkylcarbonates and LiF, as reported in previous *ex situ* studies, while the use of other formulations confirmed the SEI formation capabilities of EC as a solvent, that allows for a more stable interphase layer with a thick inorganic component, and of VC as an additive that promotes an early formation of the passivating layer.
This methodology could be expanded to different materials and chemistries, as well as different electrochemical procedures, in order to study the interphase of new electrode / electrolyte couples and in further cycles, paving the way for a thorough understanding on the SEI formation and stability. With this aim, a feasibility test was performed on HIPPIE on Silicon chip as negative electrode, applying the same experimental procedure detailed in the chapter 3. From the results shown in Figure 5.1 and 5.2, it is possible to identified also

in this case the wetting precursor layer, where both the signals from the silicon substrate and the PC solvent are observed. However, the choice of Si instead of glassy carbon complicates the procedure of the data analysis and the interpretation of the BEs shift upon applied voltage.

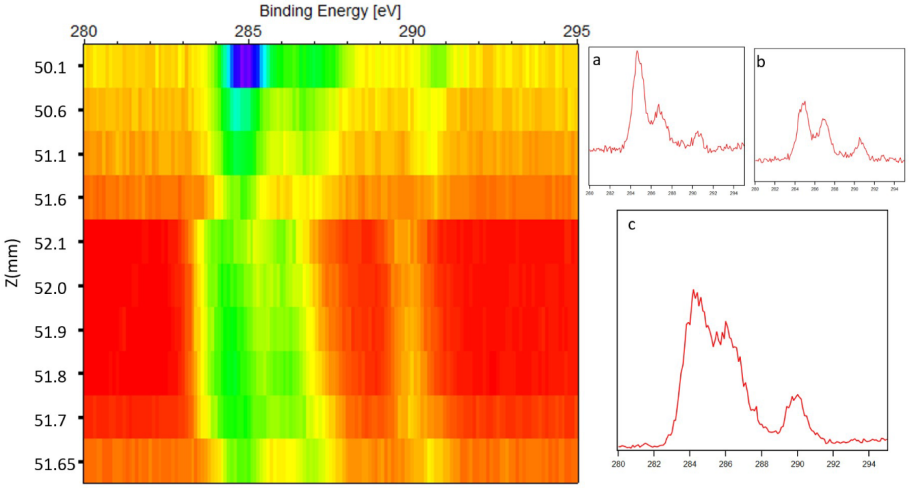


Figure 5.1: Vertical scan over the C 1s core peak on the silicon electrode. Depending on the vertical position, different phase were observed (a) the Si substrate + PC gas phase, (b) bulk PC liquid meniscus and (c) the Si substrate and PC wetting layer.

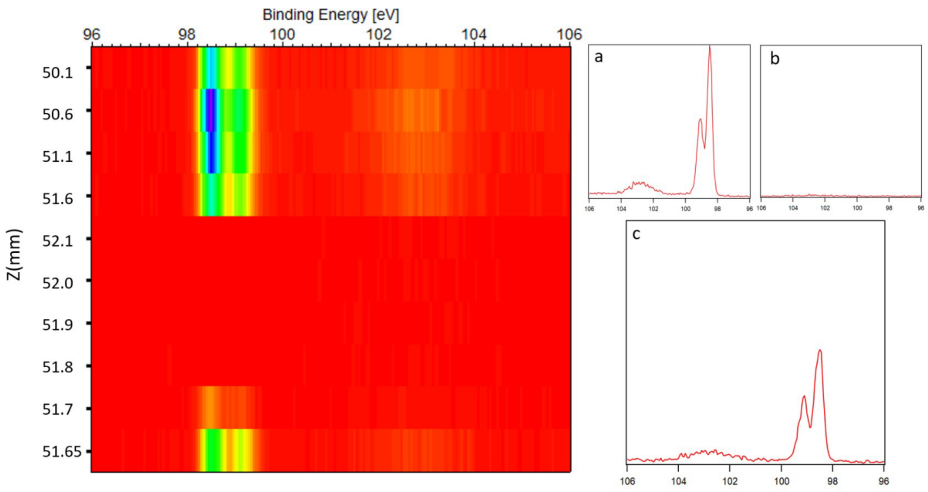


Figure 5.2: Vertical scan over the Si 1s core peak on the silicon electrode. Depending on the vertical position, different phases were observed (a) the Si substrate + PC gas, (b) no signal due to the bulk PC thick meniscus, and (c) the Si substrate and the PC wetting layer, coherently with the C 1s XPS data.

The second goal was to monitor the SEI formation in *operando* conditions using HAXPES. For this purpose, we have designed and developed a tailored *in situ* electrochemical cell

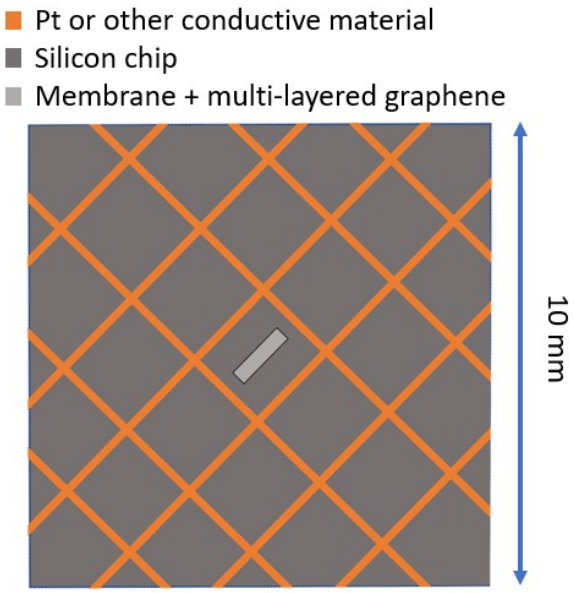


Figure 5.3: Model for a possible improvement of the inner side of the chip with a grid of Pt (or Au or other conductive material) acting as a current collector

compatible with both UHV environment and photoelectrons collection. Additionally, we expected a closer electrochemical behavior to that observed in a standard coin cell compared to the system used in the Dip&Pull approach. $Si_3N_4$ membranes were chosen as transparent window to incident X-ray and emitted photoelectrons, with different geometries and thicknesses. Despite several trials at the GALAXIES beamline, we were unable to obtain reliable results. The delicate process of assembling the cell inside the glovebox, having to deal with nm thin membranes and thin chips, led to a long process of trial and errors before an adequate procedure for the assembly that would keep the cell intact but also air tight was devised. Moreover, difficulties related to the electrolyte evaporation in UHV, the brittleness of the $Si_3N_4$ membrane, or the poor electronic conduction of the current collectors of the anode side have been raised during the experiments, as well as the difficulties related to the trade-off between thickness of the membrane, its brittleness, and the possibility to measure the interface. Despite these concerns, we were able to have a proof of concept of the HAXPES electrochemical cell. In particular, we demonstrate that when properly assembled, the cell is air-tight; moreover, the signal coming from the electrolyte was detected on the buried carbon coated interphase, confirming that the 20 nm-thick $Si_3N_4$ membrane was

suitable to ensure the photoelectron collection. Finally, it was also possible to monitor the peaks shifting during the discharge, albeit the data were not physical due to problems with the cabling. A further improvement of the membrane design is still needed, especially on the procedure for the graphene multilayer deposition - to avoid membrane breakages - and on the current collectors, as suggested in figure 5.3. This could represent the last step to unlock the potentialities of *operando* HAXPES studies on Li and Na-ion batteries.

# Bibliography


[1] A. Mikhaylov, N. Moiseev, K. Aleshin, and T. Burkhardt, "Global climate change and greenhouse effect," *Entrepreneurship and Sustainability Issues*, vol. 7, no. 4, 2897–2913, 2020.

[2] N. Abas, A. Kalair, and N. Khan, "Review of fossil fuels and future energy technologies," *Futures*, vol. 69, 31–49, 2015.

[3] K. Protocol, "Unfccc website, kyoto protocol," 1997, Available online: [Online]. Available: http://unfccc.int/kyoto_protocol/items/2830.php.

[4] J. Barton and D. Infield, "Energy storage and its use with intermittent renewable energy," *IEEE Transactions on Energy Conversion*, vol. 19, no. 2, 441–448, 2004.

[5] P.-C. Chiang, Y.-C. Chiang, E.-E. Chang, and S.-C. Chang, "Characterizations of hazardous air pollutants emitted from motor vehicles," *Toxicological & Environmental Chemistry*, vol. 56, no. 1-4, pp. 85–104, 1996.

[6] C. Fetting, "The european green deal," *ESDN report*, vol. 53, 2020.

[7] D. Hook, S. Porter, and C. Herzog, "Dimensions: Building context for search and evaluation," *Frontiers in Research Metrics and Analytics*, vol. 3, p. 23, 2018.

[8] W. Meyers and J. Simmons, "Electric current-producing cell with anhydrous organic liquid electrolyte," *Google Patents*, 1969.

[9] P. Moses, A. Taylor, and M. Turchan, "Non-aqueous li/mno2 cell," *Google Patents*, 1983.

[10] R. Bugga and M. Smart, "Lithium plating behavior in lithium-ion cells," *ECS transactions*, vol. 25, no. 36, p. 241, 2010.

[11] M. Whittingham, *Batteries à base de chalcogénures*, Mar. 10, 1975.

[12] J. Goodenough, K. Mizushima, and P. Wiseman, *Electrochemical cell and method of making ion conductors for said cell*, 1979.

[13] J.-M. Tarascon and M. Armand, "Issues and challenges facing rechargeable lithium batteries," *nature*, vol. 414, no. 6861, 359–367, 2001.

[14] P. Albertus, S. Babinec, S. Litzelman, and A. Newman, "Status and challenges in enabling the lithium metal electrode for high-energy and low-cost rechargeable batteries," *Nature Energy*, vol. 3, no. 1, 16–21, 2017.

[15] L. Croguennec and M. Palacin, "Recent achievements on inorganic electrode materials for lithium-ion batteries," *J Am Chem Soc*, vol. 137, no. 9, 3140–56, 2015.

[16] P. Verma, P. Maire, and P. Novák, "A review of the features and analyses of the solid electrolyte interphase in li-ion batteries," *Electrochimica Acta*, vol. 55, no. 22, 6332–6341, 2010.

[17] E. Peled, "The electrochemical behavior of alkali and alkaline earth metals in nonaqueous battery systems—the solid electrolyte interphase model," *Journal of The Electrochemical Society*, vol. 126, no. 12, 1979.

[18] P. Peljo and H. Girault, "Electrochemical potential window of battery electrolytes: The homo–lumo misconception," *Energy & Environmental Science*, vol. 11, no. 9, 2306–2309, 2018.

[19] K. Xu, "Nonaqueous liquid electrolytes for lithium-based rechargeable batteries," *Chemical reviews*, vol. 104, no. 10, 4303–4418, 2004.

[20] A. Patil, V. Patil, D. Wook Shin, J.-W. Choi, D.-S. Paik, and S.-J. Yoon, "Issue and challenges facing rechargeable thin film lithium batteries," *Materials Research Bulletin*, vol. 43, 8–9 , 2008.

[21] R. Yazami, "Surface chemistry and lithium storage capability of the graphite–lithium electrode," *Electrochimica acta*, vol. 45, no. 1-2, 87–97, 1999.

[22] E. Peled and H. Yamin, "Solid electrolyte interphase (sei) electrodes. part 1. the kinetics of lithium in lialcl4-socl2," *Israel Journal of Chemistry*, vol. 18, no. 1-2, 131–135, 1979.

[23] R. Fong, U. Sacken, and J. Dahn, "Studies of lithium intercalation into carbons using nonaqueous electrochemical cells," *Journal of The Electrochemical Society*, pp. 137 7 , 1990.

[24] J. Jones, M. Anouti, M. Caillon-Caravanier, P. Willmann, P.-Y. Sizaret, and D. Lemordant, "Solubilization of sei lithium salts in alkylcarbonate solvents," *Fluid phase equilibria*, vol. 305, no. 2, 121–126, 2011.

[25] K. Tasaki, A. Goldberg, J.-J. Lian, M. Walker, A. Timmons, and S. Harris, "Solubility of lithium salts formed on the lithium-ion battery negative electrode surface in organic solvents," *Journal of The Electrochemical Society*, vol. 156, no. 12, p. 1019, 2009.

[26] D. Aurbach, Y. Ein-Eli, B. Markovsky, *et al.*, "The study of electrolyte solutions based on ethylene and diethyl carbonates for rechargeable li batteries: Ii," *Graphite electrodes. Journal of The Electrochemical Society*, vol. 142, no. 9, p. 2882, 1995.

[27] J. Vetter and P. Novák, "Novel alkyl methyl carbonate solvents for lithium-ion batteries," *Journal of power sources*, vol. 119, 338–342, 2003.

[28] E. Plichta, M. Hendrickson, R. Thompson, *et al.*, "Development of low temperature li-ion electrolytes for nasa and dod applications," *Journal of power sources*, vol. 94, no. 2, 160–162, 2001.

[29] D. Abraham, M. Furczon, S.-H. Kang, D. Dees, and A. Jansen, "Effect of electrolyte composition on initial cycling and impedance characteristics of lithium-ion cells," *Journal of Power Sources*, vol. 180, no. 1, 612–620, 2008.

[30] Y. Wang, S. Nakamura, M. Ue, and P. Balbuena, "Theoretical studies to understand surface chemistry on carbon anodes for lithium-ion batteries: Reduction mechanisms of ethylene carbonate," *Journal of the American Chemical Society*, vol. 123, no. 47, 11708–11718, 2001.

[31] Y. Wang and P. Balbuena, "Theoretical insights into the reductive decompositions of propylene carbonate and vinylene carbonate: Density functional theory studies," *The Journal of Physical Chemistry B*, vol. 106, no. 17, 4486–4495, 2002.

[32] R. Marom, O. Haik, D. Aurbach, and I. Halalay, "Revisiting liclo4 as an electrolyte for rechargeable lithium-ion batteries," *Journal of the Electrochemical Society*, vol. 157, no. 8, p. 972, 2010.

[33] S. Tsubouchi, Y. Domi, T. Doi, *et al.*, "Spectroscopic characterization of surface films formed on edge plane graphite in ethylene carbonate-based electrolytes containing film-forming additives," *Journal of The Electrochemical Society*, vol. 159, no. 11, 2012.

[34] D. Aurbach, J. Gnanaraj, W. Geissler, and M. Schmidt, "Vinylene carbonate and li salicylatoborate as additives in lipf3 (cf 2 cf 3) 3 solutions for rechargeable li-ion batteries," *Journal of The Electrochemical Society*, vol. 151, no. 1, 2003.

[35] Y. Wang, S. Nakamura, K. Tasaki, and P. Balbuena, "Theoretical studies to understand surface chemistry on carbon anodes for lithium-ion batteries: How does vinylene carbonate play its role as an electrolyte additive?" *Journal of the American Chemical Society*, vol. 124, no. 16, 4408–4421, 2002.

[36] D. Aurbach, E. Zinigrad, Y. Cohen, and H. Teller, "A short review of failure mechanisms of lithium metal and lithiated graphite anodes in liquid electrolyte solutions," *Solid state ionics*, 148 3–4 , 405–416, 2002.

[37] M. Broussely, P. Biensan, F. Bonhomme, *et al.*, "Main aging mechanisms in li ion batteries," *Journal of power sources*, vol. 146, no. 1-2, 90–96, 2005.

[38] D. Aurbach, B. Markovsky, M. Levi, *et al.*, "New insights into the interactions between electrode materials and electrolyte solutions for advanced nonaqueous batteries," *Journal of power sources*, vol. 81, 95–111, 1999.

[39] K. Son, S. Hwang, S.-G. Woo, M. Paik, E. Song, and Y.-J. Kim, "Thermal and chemical characterization of the solid-electrolyte interphase in li-ion batteries using a novel separator sampling method," *Journal of Power Sources*, vol. 440, p. 227 083, 2019.

[40] K. Edström, M. Herstedt, and D. Abraham, "A new look at the solid electrolyte interphase on graphite anodes in li-ion batteries," *Journal of Power Sources*, vol. 153, no. 2, 380–384, 2006.

[41] S.-P. Kim, A. Duin, and V. Shenoy, "Effect of electrolytes on the structure and evolution of the solid electrolyte interphase (sei) in li-ion batteries: A molecular dynamics study," *Journal of Power Sources*, vol. 196, no. 20, 8590–8597, 2011.

[42] M. Nie and B. Lucht, "Role of lithium salt on solid electrolyte interface (sei) formation and structure in lithium ion batteries," *Journal of the Electrochemical Society*, vol. 161, no. 6, p. 1001, 2014.

[43] S. Patil, S. Kolekar, and A. Deshpande, "Revisiting hopg superlattices: Structure and conductance properties," *Surface Science*, vol. 658, 55–60, 2017.

[44] M. Velický, P. Toth, C. Woods, K. Novoselov, and R. Dryfe, "Electrochemistry of the basal plane versus edge plane of graphite revisited," *The Journal of Physical Chemistry C*, vol. 123, no. 18, 11677–11685, 2019.

[45] E. Peled, D. Golodnitsky, C. Menachem, and D. Bar-Tow, "An advanced tool for the selection of electrolyte components for rechargeable lithium batteries," *Journal of the electrochemical Society*, vol. 145, no. 10, p. 3482, 1998.

[46] V. Eshkenazi, E. Peled, L. Burstein, and D. Golodnitsky, "Xps analysis of the sei formed on carbonaceous materials," *Solid State Ionics*, 170 1–2 , 83–91, 2004.

[47] E. Peleda, D. Towa, A. Merson, and L. Bursteinb, "Microphase structure of sei on hopg," *Journal of New Materials for Electrochemical Systems*, vol. 3, 321–328, 2000.

[48] E. Peled, D. Golodnitsky, A. Ulus, and V. Yufit, "Effect of carbon substrate on sei composition and morphology," *Electrochimica acta*, vol. 50, no. 2-3, 391–395, 2004.

[49] R. Unocic, X.-G. Sun, R. Sacci, *et al.*, "Direct visualization of solid electrolyte interphase formation in lithium-ion batteries with in situ electrochemical transmission electron microscopy," *Microscopy and Microanalysis*, vol. 20, no. 4, 1029–1037, 2014.

[50] H. Buqa, A. Würsig, J. Vetter, M. Spahr, F. Krumeich, and P. Novák, "Sei film formation on highly crystalline graphitic materials in lithium-ion batteries," *Journal of power sources*, vol. 153, no. 2, 385–390, 2006.

[51] F. Orsini, A. Pasquier, B. Beaudoin, *et al.*, "In situ scanning electron microscopy (sem) observation of interfaces within plastic lithium batteries," *Journal of power sources*, vol. 76, no. 1, 19–29, 1998.

[52] K.-i Morigaki and A. Ohta, "Analysis of the surface of lithium in organic electrolyte by atomic force microscopy, fourier transform infrared spectroscopy and scanning auger electron microscopy," *Journal of power sources*, vol. 76, no. 2, 159–166, 1998.

[53] D. Demirocak and B. Bhushan, "In situ atomic force microscopy analysis of morphology and particle size changes in lithium iron phosphate cathode during discharge," *Journal of colloid and interface science*, vol. 423, 151–157, 2014.

[54] A. Lipson, R. Ginder, and M. Hersam, "Nanoscale in situ characterization of li-ion battery electrochemistry via scanning ion conductance microscopy," *Advanced Materials*, vol. 23, no. 47, 5613–5617, 2011.

[55] H. Zhang, D. Wang, and C. Shen, "In-situ ec-afm and ex-situ xps characterization to investigate the mechanism of sei formation in highly concentrated aqueous electrolyte for li-ion batteries," *Applied Surface Science*, vol. 507, p. 145 059, 2020.

[56] L. Seidl, S. Martens, J. Ma, U. Stimming, and O. Schneider, "In situ scanning tunneling microscopy studies of the sei formation on graphite electrodes for li+-ion batteries," *Nanoscale*, vol. 8, no. 29, 14004–14014, 2016.

[57] M. Ebner, F. Marone, M. Stampanoni, and V. Wood, "Visualization and quantification of electrochemical and mechanical degradation in li ion batteries," *Science*, vol. 342, no. 6159, 716–720, 2013.

[58] V. Vanpeene, J. Villanova, J.-P. Suuronen, *et al.*, "Monitoring the morphological changes of si-based electrodes by x-ray computed tomography: A 4d-multiscale approach," *Nano Energy*, vol. 74, p. 104 848, 2020.

[59] F. Sun, X. He, X. Jiang, *et al.*, "Advancing knowledge of electrochemically generated lithium microstructure and performance decay of lithium ion battery by synchrotron x-ray tomography," *Materials today*, vol. 27, 21–32, 2019.

[60] Z. Shadike, H. Lee, O. Borodin, *et al.*, "Identification of lih and nanocrystalline lif in the solid–electrolyte interphase of lithium metal anodes," *Nature Nanotechnology*, vol. 16, no. 5, 549–554, 2021.

[61] G. Vaughan, R. Baker, R. Barret, *et al.*, "Id15a at the esrf–a beamline for high speed operando x-ray diffraction, diffraction tomography and total scattering," *Journal of synchrotron radiation*, vol. 27, no. 2, 515–528, 2020.

[62] S. Chattopadhyay, A. Lipson, H. Karmel, *et al.*, "In situ x-ray study of the solid electrolyte interphase (sei) formation on graphene as a model li-ion battery anode," *Chemistry of Materials*, vol. 24, no. 15, 3038–3043, 2012.

[63] R. Holze, W. Spectroelectrochemistry, and A. Klein, *The Royal Society of Chemistry*. Cambridge: Springer, 2008, pp. 236 , 106 47 , ISBN: 978-0-85404-550-1.

[64] H. Martin and P. Morrison, "Application of a diamond thin film as a transparent electrode for in situ infrared spectroelectrochemistry," *Electrochemical and Solid-State Letters*, vol. 4, no. 4, p. 17, 2001.

[65] E. Flores, P. Novák, and E. Berg, "In situ and operando raman spectroscopy of layered transition metal oxides for li-ion battery cathodes," *Frontiers in Energy Research*, vol. 6, p. 82, 2018.

[66] V. Stancovski and S. Badilescu, "In situ raman spectroscopic–electrochemical studies of lithium-ion battery materials: A historical overview," *Journal of Applied Electrochemistry*, vol. 44, 23–43, 2014.

[67] B. Philippe, M. Hahlin, K. Edström, T. Gustafsson, H. Siegbahn, and H. Rensmo, "Photoelectron spectroscopy for lithium battery interface studies," *Journal of The Electrochemical Society*, vol. 163, no. 2, p. 178, 2015.

[68] D. Ketenoglu, G. Spiekermann, M. Harder, *et al.*, "X-ray raman spectroscopy of lithium-ion battery electrolyte solutions in a flow cell," *Journal of synchrotron radiation*, vol. 25, no. 2, 537–542, 2018.

[69] K. Högström, S. Malmgren, M. Hahlin, *et al.*, "The buried carbon/solid electrolyte interphase in li-ion batteries studied by hard x-ray photoelectron spectroscopy," *Electrochimica Acta*, vol. 138, 430–436, 2014.

[70] I. Källquist, R. Le Ruyet, H. Liu, *et al.*, "Advances in studying interfacial reactions in rechargeable batteries by photoelectron spectroscopy," *Journal of Materials Chemistry A*, vol. 10, no. 37, 19466–19505, 2022.

[71] J. Amici, P. Asinari, E. Ayerbe, *et al.*, "A roadmap for transforming research to invent the batteries of the future designed within the european large scale research initiative battery 2030+," *Advanced energy materials*, vol. 12, no. 17, p. 2 102 785, 2022.

[72] BIG-MAP presentation. [Online]. Available: https://www.big-map.eu/big-map.

[73] H. Zhang, Y. Yang, D. Ren, L. Wang, and X. He, "Graphite as anode materials: Fundamental mechanism, recent progress and advances," *Energy Storage Materials*, vol. 36, 147–170, 2021.

[74] M. Bianchini, M. Roca-Ayats, P. Hartmann, T. Brezesinski, and J. Janek, "There and back again—the journey of linio2 as a cathode active material," *Angewandte Chemie International Edition*, vol. 58, no. 31, 10434–10458, 2019.

[75] K. Novoselov, A. Geim, S. Morozov, *et al.*, "Electric field effect in atomically thin carbon films," *science*, vol. 306, no. 5696, 666–669, 2004.

[76] H. Zhao, S.-J. Park, F. Shi, *et al.*, "Propylene carbonate (pc)-based electrolytes with high coulombic efficiency for lithium-ion batteries," *Journal of The Electrochemical Society*, vol. 161, no. 1, p. 194, 2013.

[77] M. Xu, W. Li, X. Zuo, J. Liu, and X. Xu, "Performance improvement of lithium ion battery using pc as a solvent component and bs as an sei forming additive," *Journal of Power Sources*, vol. 174, no. 2, 705–710, 2007.

[78] T. Melin, R. Lundström, and E. Berg, "Revisiting the ethylene carbonate–propylene carbonate mystery with operando characterization," *Advanced Materials Interfaces*, vol. 9, no. 8, p. 2 101 258, 2022.

[79] L. Xing, X. Zheng, M. Schroeder, *et al.*, "Deciphering the ethylene carbonate–propylene carbonate mystery in li-ion batteries," *Accounts of chemical research*, vol. 51, no. 2, 282–289, 2018.

[80] C. Jehoulet, P. Biensan, J. Bodet, M. Broussely, C. Moteau, and C. Tessier-Lescourret, "In influence of the solvent composition on the passivation mechanism of the carbon electrode in lithium-ion prismatic cells," in *Proceedings, Symposium on Batteries for Portable Applications and Electric Vehicles*, 1997.

[81] H. Ota, Y. Sakata, A. Inoue, and S. Yamaguchi, "Analysis of vinylene carbonate derived sei layers on graphite anode," *Journal of the Electrochemical Society*, vol. 151, no. 10, p. 1659, 2004.

[82] M. Nie, J. Demeaux, B. Young, *et al.*, "Effect of vinylene carbonate and fluoroethylene carbonate on sei formation on graphitic anodes in li-ion batteries," *Journal of The Electrochemical Society*, vol. 162, no. 13, 2015.

[83] A. Einstein, "Über einen die erzeugung und verwandlung des lichtes betreffenden heuristischen gesichtspunkt [adp 17, 132 (1905," *Annalen der Physik*, vol. 517, 164–181, 2005.

[84] K. Siegbahn, *In Atomic, molecular and solid state structure studied by means of electron spectroscopy*. ESCA, 1967.

[85] J. Kumar, "Photoelectron spectroscopy: Fundamental principles and applications," *Handbook of Materials Characterization*, 435–495, 2018.

[86] C. Berglund and W. Spicer, "Photoemission studies of copper and silver: Theory," *Physical Review*, p. 136, 1964.

[87] A. Damascelli, "Probing the electronic structure of complex systems by arpes," *Physica Scripta*, vol. T109, p. 61, 2004.

[88] S. Tanuma, C. Powell, and D. Penn, "Calculations of electron inelastic mean free paths for 31 materials," *Surface and Interface Analysis*, vol. 11, no. 11, 577–589, 1988.

[89] C. Fadley, "X-ray photoelectron spectroscopy: Progress and perspectives," *Journal of Electron Spectroscopy and Related Phenomena*, vol. 178, 2–32, 2010.

[90] C. Powell, A. Jablonski, I. Tilinin, S. Tanuma, and D. Penn, "Surface sensitivity of auger-electron spectroscopy and x-ray photoelectron spectroscopy," *Journal of Electron Spectroscopy and Related Phenomena*, vol. 98, 1–15, 1999.

[91] W. Egelhoff Jr, "Core-level binding-energy shifts at surfaces and in solids," *Surface Science Reports*, vol. 6, no. 6-8, 253–415, 1987.

[92] F. Adams, "X-ray absorption and diffraction-overview," *Encyclopedia of analytical science*, Paul J.[edit, vol. 9, no. Worsfold, 365–378, 2005.

[93] *Esrf what is synchrotron light.* [Online]. Available: https://www.esrf.fr/home/education/what-is-the-esrf/what-is-synchrotron-light.html..

[94] J. Cazes, *Analytical instrumentation handbook*. CRC Press, 2004.

[95] J. Helmer and N. Weichert, "Enhancement of sensitivity in esca spectrometers," *Applied Physics Letters*, vol. 13, no. 8, 266–268, 1968.

[96] J. Matthew, "Surface analysis by auger and x-ray photoelectron spectroscopy," *Surface and Interface Analysis*, vol. 36, no. 13, D. Briggs, J. IMPublications, U. Chichester, and SurfaceSpectra, Eds., pp. 900 , 2003.

[97] C. Weiland, A. Rumaiz, P. Pianetta, and J. Woicik, "Recent applications of hard x-ray photoelectron spectroscopy," *Journal of Vacuum Science & Technology A*, p. 34 3, 2016.

[98] J.-P. Rueff, J. Rault, J. Ablett, Y. Utsumi, and D. Céolin, "Haxpes for materials science at the galaxies beamline," *Synchrotron Radiation News*, vol. 31, no. 4, 4–9, 2018.

[99] S. Zhu, M. Scardamaglia, J. Kundsen, *et al.*, "Hippie: A new platform for ambient-pressure x-ray photoelectron spectroscopy at the max iv laboratory," *Journal of synchrotron radiation*, vol. 28, no. 2, 624–636, 2021.

[100] S. Omicron, *Hipp-3: Imaging ambient pressure electron analyser*. [Online]. Available: https://scientaomicron.com/en/Instruments/Electron-Analysers/HiPP-3..

[101] F. G. Capone, J. Sottmann, V. Meunier, *et al.*, "Operando observation of the dynamic sei formation on a carbonaceous electrode by near-ambient pressure xps," *Energy & Environmental Science*, 2024.

[102] R. Fowler, *Statistical thermodynamics*. CUP Archive, 1939.

[103] C. Herring and M. Nichols, "Thermionic emission," *Reviews of modern physics*, vol. 21, no. 2, p. 185, 1949.

[104] H. Reiss, "The fermi level and the redox potential," *The Journal of Physical Chemistry*, vol. 89, no. 18, 3783–3791, 1985.

[105] J. Broughton and D. Perry, "Electron binding energies in the study of adsorption by photoelectron spectroscopy: The reference level problem," *Surface Science*, vol. 74, no. 1, 307–317, 1978.

[106] M. Favaro, B. Jeong, P. Ross, *et al.*, "Unravelling the electrochemical double layer by direct probing of the solid/liquid interface," *Nature communications*, vol. 7, no. 1, p. 12 695, 2016.

[107] J. Maibach, I. Källquist, M. Andersson, *et al.*, "Probing a battery electrolyte drop with ambient pressure photoelectron spectroscopy," *Nature Communications*, vol. 10, no. 1, p. 3080, 2019.

[108] J. Maibach, J. Rizell, A. Matic, and N. Mozhzhukhina, "Toward operando characterization of interphases in batteries," *ACS Materials Letters*, vol. 5, no. 9, 2431–2444, 2023.

[109] I. Kallquist, F. Lindgren, M.-T. Lee, *et al.*, "Probing electrochemical potential differences over the solid/liquid interface in li-ion battery model systems," *ACS applied materials & interfaces*, vol. 13, no. 28, 32989–32996, 2021.

[110] I. Kallquist, T. Ericson, F. Lindgren, *et al.*, "Potentials in li-ion batteries probed by operando ambient pressure photoelectron spectroscopy," *ACS applied materials & interfaces*, vol. 14, no. 5, 6465–6475, 2022.

[111] D. Bonn, J. Eggers, J. Indekeu, J. Meunier, and E. Rolley, "Wetting and spreading," *Reviews of modern physics*, vol. 81, no. 2, p. 739, 2009.

[112] F. Lindgren, D. Rehnlund, I. Källquist, *et al.*, "Breaking down a complex system: Interpreting pes peak positions for cycled li-ion battery electrodes," *The Journal of Physical Chemistry C*, vol. 121, no. 49, 27303–27312, 2017.

[113] J. Wu, "Understanding the electric double-layer structure, capacitance, and charging dynamics," *Chemical Reviews*, vol. 122, no. 12, 10821–10859, 2022.

[114] J. Nakayama, H. Zhou, J. Izumi, *et al.*, "Electrical double layer formation at intercalation cathode–organic electrolyte interfaces during initial lithium-ion battery reactions," *Advanced Materials Interfaces*, p. 2 300 780, 2023.

[115] H. Li, W. Zhang, X. Yang, *et al.*, "State of charge estimation for lithium-ion battery using an electrochemical model based on electrical double layer effect," *Electrochimica Acta*, vol. 326, p. 134 966, 2019.

[116] K. Xu, "Whether ec and pc differ in interphasial chemistry on graphitic anode and how," *Journal of The Electrochemical Society*, vol. 156, no. 9, p. 751, 2009.

[117] M. Herstedt, A. M. Andersson, H. Rensmo, H. Siegbahn, and K. Edström, "Characterisation of the sei formed on natural graphite in pc-based electrolytes," *Electrochimica Acta*, vol. 49, no. 27, pp. 4939–4947, 2004.

[118] X. Zhang, C. Fan, and S. Han, "Effect of vinylene carbonate on electrochemical performance and surface chemistry of hard carbon electrodes in lithium ion cells operated at different temperatures," *Electrochimica Acta*, vol. 222, 221–231, 2016.

[119] Y. Yang, J. Xiong, S. Lai, *et al.*, "Vinyl ethylene carbonate as an effective sei-forming additive in carbonate-based electrolyte for lithium-metal anodes," *ACS applied materials & interfaces*, vol. 11, no. 6, 6118–6125, 2019.

[120] D. Aurbach, K. Gamolsky, B. Markovsky, Y. Gofer, M. Schmidt, and U. Heider, "On the use of vinylene carbonate (vc) as an additive to electrolyte solutions for li-ion batteries," *Electrochimica acta*, vol. 47, no. 9, 1423–1439, 2002.

[121] L El Ouatani, R. Dedryvère, C Siret, *et al.*, "The effect of vinylene carbonate additive on surface film formation on both electrodes in li-ion batteries," *Journal of the Electrochemical Society*, vol. 156, no. 2, A103, 2008.

[122] S. M. Kurtz, "Chemical and radiation stability of peek," in *PEEK biomaterials handbook*, Elsevier, 2012, pp. 75–79.

[123] W. Smekal, W. Werner, and C. Powell, "Simulation of electron spectra for surface analysis (sessa): A novel software tool for quantitative auger-electron spectroscopy and x-ray photoelectron spectroscopy," *Surface and Interface Analysis: An International Journal devoted*, to the development and application of techniques for the analysis of surfaces, interfaces and thin films, vol. 37, no. 11, 1059–1067, 2005.

[124] J. Velasco-Velez, V. Pfeifer, M. Havecker, *et al.*, "Photoelectron spectroscopy at the graphene-liquid interface reveals the electronic structure of an electrodeposited cobalt/graphene electrocatalyst," *Angew Chem Int Ed Engl*, vol. 54, no. 48, 14554–8, 2015.

[125] C. Shearer, A. Slattery, A. Stapleton, J. Shapter, and C. Gibson, "Accurate thickness measurement of graphene," *Nanotechnology*, vol. 12, p. 27, 2016.

# Acknowledgements

This thesis would not have been possible, first and foremost, without the funding from SOLEIL and BIG-MAP, which I thank.
Secondly, I cannot fail to express my gratitude to my advisors, Alexis and Jonas, and then to Jean-Pascal and Antonella, without whom this thesis would not have started nor been completed. There are many other individuals who contributed to this work. The entire staff of the GALAXIES beamline assisted me in developing the cell, along with the mechanical workshop, chemistry, vacuum, and materials laboratories, while all the Dip&Pull results are thanks to the entire HIPPIE staff in Lund. I was fortunate to collaborate with other students from the Collége de France, and with professors such as Rémi, without whom XPS would have many more mysteries for me than it does now. The group of young researchers at SOLEIL reminded me that even within the sometimes dark and lonley synchrotron, there is always another student willing to share a beer at the end of the day. Finally, my "group" colleagues, Gilles, Lucia, and eventually Francesco, with whom in the perhaps short but significant time spent together as a group, I learned many things that helped me get through these three years. Thanks to them, beamtimes and office hours were always a bit brighter.

All the friends made in Paris, and those remaining in Italy or scattered across Europe, and my family, formed an indispensable network for me during this PhD, that helped me go through thick and thin. A network with Francesca at its center, that in the midst of a pandemic, decided to accompany me on this Parisian adventure and helped me ever since.

I never think I possess great qualities, but one thing I am certain of is the luck I have in encountering the people around me, and these years have only confirmed it. These few lines of acknowledgements does not express that a tiny fraction of the gratitude I have for all the help I had these years.

Thanks to everyone.